OPTICAL VECTOR-VORTEX BEAMS: GENERATION, CHARACTERIZATION AND APPLICATIONS

A thesis submitted in partial fulfillment

of the award of the degree of

Doctor of Philosophy

By

V.V.G. KRISHNA INAVALLI

School of Physics

University of Hyderabad

Hyderabad – 500046, India

June-2012

DECLARATION

I hereby declare that the content embodied in this thesis entitled "Optical Vector-vortex beams: Generation, Characterization and Applications" submitted to University of Hyderabad for the award of Doctor of Philosophy in Physics is a record of original research work carried out by me under the supervision of Dr Nirmal K Viswanathan, School of Physics, University of Hyderabad, Hyderabad. This work has not been submitted partially or fully for any degree in any other university.

Place: Hyderabad V.V.G. Krishna Inavalli

Date:

CERTIFICATE

This is to certify that the research work presented in this thesis entitle "Optical Vector-vortex beams: Generation, Characterization and Applications" for the award of Doctor of Philosophy is an original work carried out by Mr. V.V.G. Krishna Inavalli under my direct supervision and the same has not been submitted for the award of any degree or diploma.

Place: Hyderabad
Date:

Dr. Nirmal K Viswanathan
(Thesis supervisor)

Dean
School of Physics

Dedicated To My Parents.....

Acknowledgements

I express my deep sense of gratitude and profound thanks to my supervisor ***Dr. Nirmal K Viswanathan*** *for his valuable guidance, patience, encouragement, and for the freedom he gave me in carrying out research. Throughout my PhD tenure, he was always approachable, helpful, friendly and extremely tolerant. I consider my association with him as a cherished memory in my life and it is an honor to be his first PhD student.*

I take this opportunity to thank my doctoral committee members, Prof. D. Narayana Rao, Dr. Suneel Singh and Dr. V. Ashoka, who offered helpful suggestions and comments, every six months during my Ph. D tenure.

I would like to thank Prof. H.S. Mani, Prof. A.K. Kapoor, Prof. S. Chaturvedi, Prof. S.P. Tewari, Prof. Bamba and Prof. R. Nityananda, for their timely help to understand the mathematical concepts.

It is a great pleasure to thank P. Vijay, Y.V. Jayasurya and Sarat, for their help in Matlab programs and my lab mates Geo, Shankar and Vijay, for useful discussions and timely help.

I would like to thank my batch mates (07PHPH) with whom I enjoyed a lot during birthday celebrations and month end parties. I like to thank NRS hostel-mates Sekhar, Bharat, Chalapathi, Kishore, Kalyan, Naveen, Ramesh and Seshu for making hostel life more memorable.

I would like to thank Mr. Abraham for his assistance throughout my PhD.

I feel fortunate to have friends Santosh, Inthiyaz and Sowjanya who have been good friends over the years, for keeping me sane and giving me a perspective. A special note of thank to Sandhya for helping me at various occasions though out my PhD tenure.

Most of all, I would like to thank my parents and my younger brother (Hanu), who supported me for so many things with their love and absolute confidence in me.

Last but not least, I thank UOH and CAS-RFSMS for the financial support and DST for the travel grant to attend workshop in Italy.

Contents

Abbreviations

OV	Optical vortex
VV	Vector vortex
SAM	Spin angular Momentum
OAM	Orbital angular momentum
SOI	Spin orbit interaction
CVB	Cylindrical vector beam
TMF	Two-mode fiber
QWP	Quarter wave plate
HWP	Half wave plate
HG	Hermite-Gaussian
LG	Laguerre-Gaussian
CW	Clockwise
CCW	Counter clockwise
NA	Numerical aperture
SOP	State of polarization
ZIP	Zero intensity point
RDE	Rotational Doppler-effect
DP	Dove prism

Introduction

Singular optics is an already well recognized and rapidly developing branch of modern optics dealing with singularities such as (i) caustics in geometrical optics, (ii) edge, screw and mixed dislocations in scalar wave optics and (iii) L–line, C-point and disclinations in vector wave optics [1-4]. In scalar wave optics, the singularities that deal with optical beams with helical wavefront are known as optical vortices (OVs). At the vortex core the amplitude vanishes and hence the phase becomes indeterminate (singular). Laguerre-Gaussian (LG_{nl}) and higher-order Bessel-Gaussian (BG)-$J_n(kr)$; $n \geq 1$ beams are some of the well known examples of beams carrying OVs. The seminal paper by Nye and Berry titled "*Dislocations in wave trains*" introduced the phase singularities in analogy with defects in crystals as a new class of objects in electromagnetic wave theory [5]. Further, Berry concluded that the phase singularities are the most remarkable features of the wavefronts [1].This concept was expanded subsequently by Nye and Hajnal to include vectorial (polarization) singularities such as C-point, L-line and disclinations in paraxial electromagnetic waves [2, 6-11]. The C-point is where the field is circularly polarized making the azimuth of the polarization ellipse indeterminate. The L-line is where the field is linearly polarized and consequently the handedness of the polarization ellipse is undefined and it also separates the regions of opposite handedness of polarization and disclinations are points where one of the components of the transverse field is an instantaneous zero [2, 6].

Allen et.al., [12] demonstrated that optical beams with helical wavefront also carry Orbital Angular Momentum (OAM) which kick-started the widespread research activity in the area of beams and photons with optical angular momentum which includes both spin (circular polarization) and orbital

momentum (helical phase) beyond its generation and characterization to include a wide variety of applications [13, 14]. More recently, Bekshaev and Soskin associated OAM with polarization singularities as well (C-point) [14, 15].

There are different methods available to generate OV beams in the laboratory [16-18]. The most commonly used are the computer-generated hologram (CGH) and spatial light modulator (SLM). In the CGH method, OVs with arbitrary topological charge are first simulated in computer and subsequently printed on a transparent substrate, whereas in the case of SLM by applying voltage to the pixels, beams with different topological charges are generated. A Gaussian beam transmitted or reflected by these optical elements will generate a beam with embedded OV. The beams generated using these methods are scalar beams, meaning that the polarization across the beam cross section is uniform.

Beams with spatially inhomogeneous polarization such as radial (TM_{01}) and azimuthal (TE_{01}) field orientations are the well known examples of vector beams. These beams are also known as cylindrical vector (CV) beams due to their cylindrical symmetry in polarization and have enabled several applications due to their unusual polarization characteristics [19, 20]. There are different methods to generate these vector beams, the most commonly used method is the interferometric technique, based on interfering two linear orthogonally polarized Hermite-Gaussian HG_{10} and HG_{01} modes either inside or outside a cavity.

An optically isotropic and inhomogeneous medium such as an optical fiber is a simple and inexpensive method to generate beams with both spatially inhomogeneous polarization (vector) and vortex beams. This is possible as both the vector and vortex modes are the eigen modes of the fiber in linear and

circular polarization basis [21-26]. Zel'dovich et.al., [27], reported first the presence of vortices in the fiber radiation field which they studied theoretically and experimentally using fork interference pattern in the scattered laser field and subsequently suggested filtration method to isolate a single pure screw dislocation [28]. Volyar and Fadeyeva revealed that the optical vortices are the guiding modes of the fiber and described their properties [29, 30]. In the recent years pure vector modes of the fiber are generated using two-mode optical fiber by coupling the Gaussian beam or the externally generated Laguerre-Gaussian (LG) beam [31-33].

In this thesis, we present a controllable generation of different combinations of optical vector-vortex (VV) beams from a two-mode step-index fiber. The VV beams are generated by coupling the input Gaussian beam from a He-Ne laser as skew-offset beam. The output beams are characterized for both the vector and vortex behavior using different techniques such as analyzer rotation, interferometric method, complex Stokes parameter method and the state of polarization (SOP) map at each point in the output beam cross section. The skew-offset launch with respect to the fiber axis enables us to flip between the positive and negative helical phase structures and controllable generation of output beam with two C-points with same topological charge and isolated C-point with different topological charges.

Organization of the Thesis

The thesis is organized as follows: in the first chapter we introduce the necessary mathematical background for the fiber modes in different basis such as vector, LP and circular vortex modes. The appearance of vector singularities in the fiber modes is also introduced in this chapter. In the second chapter we

present our experimental results on the generation of vector-vortex beams and the switching between the different VV modes. Also presented are our results on the effect of the fiber length and the NA of the input lens on the excitation of these modes. In the third chapter we introduce polarization singularities in paraxial waves, their characterization methods and our experimental results on the wavelength dependence of polarization singularities. In the fourth chapter we present our results on the generation of isolated polarization singularities and the switching between the different topological charges of the C-point. In the fifth chapter we present two applications of optical vortex beams with embedded polarization singularities including the demonstration of rotational Doppler-effect and the characterization of Dove prism using the well defined polarization singularities. Finally, in the sixth chapter we summarize the results obtained and suggest some future scope of the present work.

Chapter 1

Vector and Vortex Modes of Optical Fiber

We introduce first the necessary mathematical background for the fiber modes in different basis such as vector, LP and circular vortex modes. The vector modes of the step-index fiber are obtained by solving the vector wave equation in which the guided modes of the fiber have different propagation constants. Applying the weakly guiding approximation, the vector wave equation reduces to the scalar wave equation. In this approximation, the guided modes of the fiber have the same propagation constants resulting in the LP mode formalism. Alternately, the propagation constant degeneracy in the weakly guiding approximation is lifted by including polarization or birefringence correction term to the scalar propagation constant using perturbation method. The formation of circularly polarized vortex modes is introduced by solving the vector wave equation in quantum operator form in the weakly guiding approximation. Further, the propagation and formation of the vector modes and the formation of circular vortex modes are presented in terms of the vector singularities and circularly polarized (CP) modes to better understand the results presented in this thesis.

1.1 Introduction

Optical waveguides or optical fibers are dielectric structures and they are ideally uniform along the axis of propagation. Due to which the optical properties of the fiber are described by their transverse characteristics, which are defined by the refractive index profile of the fiber. The arbitrary refractive index profile of an optical fiber is defined as [23]

$$n(r) = n_{co}\left[1 - 2\Delta f(r)\right]^{1/2} \tag{1.1}$$

where 'r' is the radial coordinate defined as $n(r) = n(x, y)$, f(r) describe the shape of the refractive index profile and 'Δ' is the profile height or the relative refractive index defined as

$$\Delta = \left(n_{co}^2 - n_{cl}^2\right) / 2n_{co}^2 \tag{1.2}$$

where 'n_{co}' is the refractive index of the core and 'n_{cl}' is the refractive index of the cladding.

The step-index fiber is the simplest index profile, which has a circular core of uniform refractive index (n_{co}) surrounded by the cladding of lower uniform refractive index (n_{cl}), which is assumed to be unbounded. Thus the only variation in the profile is a step or jump discontinuity at the core and cladding interface as shown in Fig.1.1. Hence, for a step-index fiber the shape of the profile f(r) becomes a heaviside function, in the core $f(r) = 0$ and in the cladding $f(r) = 1$ and the eqn. (1.1) for a step-index fiber is [23]

$$\begin{aligned} n(r) &= n_{co} && 0 \le r < \rho \\ n(r) &= n_{cl} && \rho < r < \infty \end{aligned} \tag{1.3}$$

where 'ρ' is radius of the core.

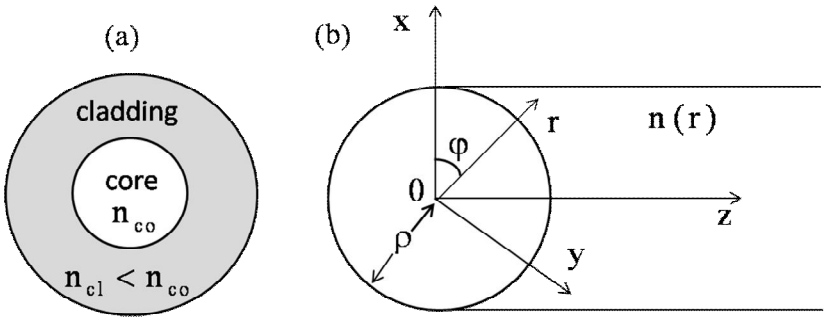

Figure 1.1: (a) Cross section of the step-index fiber (b) Symbols used for describing circular fiber, x,y,z are Cartesian coordinates and r,φ ,z are cylindrical polar coordinates. The core radius is ρ and $n(r)$ is the refractive index profile. The z-axis coincides with the fiber axis of symmetry.

In general, three large mode groups are excited in a fiber, classified as guided modes (bound modes), leaky modes and radiation modes [23]. However, if the transmission mode is far from the cut-off frequency, the contributions from the leaky and radiation modes are very small and can be ignored [23]. In this thesis, the fiber used to generate vector-vortex beams is operated far from the cut-off frequency for the first six waveguide modes (for the He-Ne laser at λ=632.8nm). In the step-index fiber, the bound modes have exact analytical solutions for circularly symmetric fiber and elliptical fibers, derived from the source free Maxwell's wave equations [23].

1.2 Vector modes of step-index fiber

The source free Maxwell's wave equations with current density $J=0$ and charge density $\sigma=0$, the dielectric constant ε(x,y,z) is related to the refractive index n(x,y,z) by $\varepsilon=n^2\varepsilon_0$ and the vector fields with implicit time dependence exp(-iωt) are written as [34]

$$\begin{aligned}
&\nabla\times\mathbf{E} = i(\mu_0/\varepsilon_0)^{1/2}k\mathbf{H}\\
&\nabla\times\mathbf{H} = -i(\mu_0/\varepsilon_0)^{1/2}kn^2\mathbf{E}\\
&\nabla\cdot(n^2\mathbf{E}) = 0\\
&\nabla\cdot\mathbf{H} = 0
\end{aligned} \tag{1.4}$$

where the symbols in bold represents the vector quantities, μ_0 and ε_0 are the magnetic permeability and dielectric constants in free space, k is wave number related with free space wavelength 'λ' as $k = 2\pi/\lambda$ and $\nabla\times$ and $\nabla\cdot$ are the curl and the divergence operators defined in Appendix 1 . The electric and magnetic fields for a translationally invariant waveguide are expressible as superposition of fields with separable form [35]

$$\begin{aligned}
&\mathbf{E}(x,y,z) = \mathbf{e}(x,y)\exp(i\beta z)\\
&\mathbf{H}(x,y,z) = \mathbf{h}(x,y)\exp(i\beta z)
\end{aligned} \tag{1.5}$$

where 'β' is the propagation constant. The corresponding forms in the cylindrical polar coordinates are

$$\begin{aligned}
&\mathbf{E}(r,\varphi,z) = \mathbf{e}(r,\varphi)\exp(i\beta z)\\
&\mathbf{H}(r,\varphi,z) = \mathbf{h}(r,\varphi)\exp(i\beta z)
\end{aligned} \tag{1.6}$$

We decompose these fields into longitudinal and transverse components, parallel and perpendicular to the waveguide axis respectively denoted by subscripts 'z' and 't' as

$$\begin{aligned}
&\mathbf{E}(x,y,z) = (\mathbf{e}_t + e_z\hat{\mathbf{z}})\exp(i\beta z)\\
&\mathbf{H}(x,y,z) = (\mathbf{h}_t + h_z\hat{\mathbf{z}})\exp(i\beta z)
\end{aligned} \tag{1.7}$$

where $\hat{\mathbf{z}}$ is the unit vector parallel to the waveguide axis. The fields **E**, **H** with separable form (eqn. (1.7)) are substituted in source free Maxwell's wave equation (eqn. (1.4)) and by comparing, the longitudinal and transverse field components are written as

$$\mathbf{e}_t = -\left(\frac{\mu_0}{\varepsilon_0}\right)^{1/2}\frac{1}{kn^2}\hat{\mathbf{z}}\times\{\beta\mathbf{h}_t + i\nabla_t h_z\} \tag{1.8(a))}$$

$$\mathbf{h}_t = \left(\frac{\varepsilon_0}{\mu_0}\right)^{1/2} \frac{1}{k} \hat{\mathbf{z}} \times \{\beta \mathbf{e}_t + i \nabla_t e_z\} \tag{1.8(b)}$$

$$e_z = i\left(\frac{\mu_0}{\varepsilon_0}\right)^{1/2} \frac{1}{kn^2} \hat{\mathbf{z}} \cdot \nabla_t \times h_t \tag{1.8(c)}$$

$$h_z = -i\left(\frac{\varepsilon_0}{\mu_0}\right)^{1/2} \frac{1}{k} \hat{\mathbf{z}} \cdot \nabla_t \times \mathbf{e}_t \tag{1.8(d)}$$

By eliminating the $\mathbf{h}_t$ and $\mathbf{e}_t$ from the eqns. (1.8(a) and (b)), we can express the transverse field components interms of the longitudinal field components as [35]

$$\begin{aligned} \mathbf{e}_t &= \frac{i}{k^2 n^2 - \beta^2} \{\beta \nabla_t e_z - \left(\frac{\mu_0}{\varepsilon_0}\right) k \hat{\mathbf{z}} \times \nabla_t h_z\} \\ \mathbf{h}_t &= \frac{i}{k^2 n^2 - \beta^2} \{\beta \nabla_t h_z + \left(\frac{\mu_0}{\varepsilon_0}\right) k \hat{\mathbf{z}} \times \nabla_t e_z\} \end{aligned} \tag{1.9}$$

From eqn. (1.9) it is clear that by knowing the longitudinal field components we can determine the transverse field components which simplifies the mathematical complications to solve the vector wave equation. Eliminating either the electric or the magnetic fields from eqn. (1.4), results in the homogenous vector wave equation

$$\begin{aligned} \{\nabla^2 + n^2 k^2\}\mathbf{E} &= -\nabla(\mathbf{E} \cdot \nabla \ln n^2) \\ \{\nabla^2 + n^2 k^2\}\mathbf{H} &= (\nabla \times \mathbf{H}) \times \nabla \ln n^2 \end{aligned} \tag{1.10}$$

Using eqn. (1.7), the fields with separable form, the eqn. (1.10) becomes

$$\begin{aligned} \{\nabla_t^2 + n^2 k^2 - \beta^2\}(\mathbf{e}_t + e_z \hat{\mathbf{z}}) &= -(\nabla_t + i\beta \hat{\mathbf{z}}) \mathbf{e}_t \cdot \nabla_t \ln n^2 \\ \{\nabla_t^2 + n^2 k^2 - \beta^2\}(\mathbf{h}_t + h_z \hat{\mathbf{z}}) &= \{(\nabla_t + i\beta \hat{\mathbf{z}}) \times \mathbf{h}_t\} \times \nabla_t \ln n^2 \end{aligned} \tag{1.11}$$

The above equation (eqn. (1.11)) contains all the information necessary to determine the spatial dependence of the fields everywhere in the waveguide and the term $\nabla_t \ln n^2$ couples various components of the field, which describes the polarization phenomena or the spin-orbit interaction (SOI) in optical fibers [36-

38]. The SOI influences the input state of polarization and phase velocities of the different handedness of circular polarization [39-41]. From eqn. (1.11), we need to solve only for the longitudinal field components of the vector field from which the transverse field components are derived using eqn. (1.9). Hence, the longitudinal field component of the vector wave equation is

$$\begin{aligned} \{\nabla_t^2 + n^2k^2 - \beta^2\}e_z &= -i\beta \mathbf{e}_t \cdot \nabla_t \ln n^2 \\ \{\nabla_t^2 + n^2k^2 - \beta^2\}h_z &= (\nabla_t h_z - i\beta \mathbf{h}_t\} \cdot \nabla_t \ln n^2 \end{aligned} \tag{1.12}$$

For a step-profile waveguide, a general approach to solve the above equation for mode fields is to solve the vector wave equation in regions where the profile is continuous, in the core and in the cladding where $\nabla_t \ln n^2 = 0$. Then using boundary conditions of Maxwell's equations in the core-clad boundary where $\nabla_t \ln n^2 \neq 0$, the field amplitudes are determined.

To facilitate description of the mode fields, dimensionless modal parameters U_j and W_j for the core and cladding are introduced and they are related by normalized frequency V as follows [23]

$$\begin{aligned} U_j &= \rho(kn_{co}^2 - \beta_j^2)^{1/2} \\ W_j &= \rho(\beta_j^2 - kn_{cld}^2)^{1/2} \\ V &= U_j^2 + W_j^2 \end{aligned} \tag{1.13}$$

In the core and the clad regions the eqn. (1.12) reduce to a scalar wave equation

$$\begin{aligned} \{\nabla_t^2 + n^2k^2 - \beta^2\}e_z &= 0 \\ \{\nabla_t^2 + n^2k^2 - \beta^2\}h_z &= 0 \end{aligned} \tag{1.14}$$

The solution for e_z and h_z must satisfy these equations in both the core and the cladding regions, and by imposing e_z or $h_z = \psi(r,\varphi)$, the eqn. (1.14) in core and cladding regions for a cylindrical symmetric step index fiber are [23]

$$\left\{\frac{\partial^2}{\partial R^2}+\frac{1}{R}\frac{\partial}{\partial R}+\frac{1}{R^2}\frac{\partial^2}{\partial \varphi^2}+U^2\right\}\psi=0 \qquad 0\le R<1 \qquad (1.15(a))$$

$$\left\{\frac{\partial^2}{\partial R^2}+\frac{1}{R}\frac{\partial}{\partial R}+\frac{1}{R^2}\frac{\partial^2}{\partial \varphi^2}-W^2\right\}\psi=0 \qquad 0\le R<\infty \qquad (1.15(b))$$

where the normalized radius R = r/ρ, and U and W are as defined in eqn. (1.13). Due to circular symmetry, ψ must have the same value after the rotation of '2π' in the cross section plane, and the azimuthal (φ) dependence must be invariant along the 'z'. Thus, the solutions are written in the separable form $\psi(r,\varphi)=\psi(r)\begin{Bmatrix}\cos(\nu\varphi)\\ \sin(\nu\varphi)\end{Bmatrix}$. The 'r' dependent part gives the solutions interms of the Bessel functions of first and second kind in core and cladding regions respectively. Then the separable solutions, everywhere bounded varies as $J_\nu(UR)\cos(\nu\varphi)$ or $J_\nu(UR)\sin(\nu\varphi)$ in the core, and as $K_\nu(WR)\cos(\nu\varphi)$ or $K_\nu(WR)\sin(\nu\varphi)$ in the cladding.

To construct the fields of waveguide we choose longitudinal components, which are continuous across the interface $r=\rho$ or $R=1$

$$e_z=A\frac{J_\nu(UR)}{J_\nu(U)}f_\nu(\varphi)\ , \qquad h_z=B\frac{J_\nu(UR)}{J_\nu(U)}g_\nu(\varphi) \quad 0\le R<1 \qquad (1.16(a))$$

$$e_z=A\frac{K_\nu(WR)}{K_\nu(W)}f_\nu(\varphi), \qquad h_z=B\frac{K_\nu(WR)}{K_\nu(W)}g_\nu(\varphi) \quad 0\le R<\infty \qquad (1.16(b))$$

where A and B are constants, and f_ν and g_ν are either $\sin\nu\varphi$ or $\cos\nu\varphi$. The dependence can be derived from the transverse components because each transverse component can depend on either f_ν or g_ν, but not both. These conditions are important in order to write the continuity of the four transverse

components at $r=\rho$ independent of 'φ' to derive the eigenvalue equation. Now let us write the transverse components of cylindrically symmetric step-index waveguide, from eqn. (1.9)

$$\begin{aligned}
e_r &= \frac{i}{k^2n^2-\beta^2}\left\{\beta\frac{\partial e_z}{\partial r}+\left(\frac{\mu_0}{\varepsilon_0}\right)^{1/2}\frac{k}{r}\frac{\partial h_z}{\partial\varphi}\right\}\\
e_\varphi &= \frac{i}{k^2n^2-\beta^2}\left\{\frac{\beta}{r}\frac{\partial e_z}{\partial\varphi}-\left(\frac{\mu_0}{\varepsilon_0}\right)^{1/2}k\frac{\partial h_z}{\partial r}\right\}\\
h_r &= \frac{i}{k^2n^2-\beta^2}\left\{\beta\frac{\partial h_z}{\partial r}-\left(\frac{\varepsilon_0}{\mu_0}\right)^{1/2}\frac{kn^2}{r}\frac{\partial e_z}{\partial\varphi}\right\}\\
h_\varphi &= \frac{i}{k^2n^2-\beta^2}\left\{\frac{\beta}{r}\frac{\partial h_z}{\partial\varphi}+\left(\frac{\varepsilon_0}{\mu_0}\right)^{1/2}kn^2\frac{\partial e_z}{\partial r}\right\}
\end{aligned} \qquad (1.17)$$

From the transverse components (eqn. (1.17)) the derivative of f_ν and g_ν appear in the terms $\frac{\partial}{\partial\varphi}$. If we define $f_\nu=\sin\nu\varphi$, we need $g_\nu=\cos\nu\varphi$, so that the 'e_r' be a function of $\sin\nu\varphi$ and not the linear combination of $\sin\nu\varphi$ and $\cos\nu\varphi$. Let us consider the first combination $f_\nu(\varphi)=\sin\nu\varphi$ and $g_\nu(\varphi)=\cos\nu\varphi$ gives

$\frac{\partial f_\nu}{\partial\varphi}=\nu g_\nu$, and $\frac{\partial g_\nu}{\partial\varphi}=-\nu f_\nu$

The second combination must be $f_\nu(\varphi)=\cos\nu\varphi$ and $g_\nu(\varphi)=-\sin\nu\varphi$ in order to obtain same derivatives as above. Hence, there are only two possible combinations

$$f_\nu(\varphi)=\begin{Bmatrix}\cos\nu\varphi\\ \sin\nu\varphi\end{Bmatrix} \quad \text{and} \quad g_\nu(\varphi)=\begin{Bmatrix}-\sin\nu\varphi\\ \cos\nu\varphi\end{Bmatrix} \qquad (1.18)$$

In above form the first line $f_\nu(\varphi)=\cos\nu\varphi$ and $g_\nu(\varphi)=-\sin\nu\varphi$ corresponds to the even or symmetric modes with respect to x-axis and the second line

$f_\nu(\varphi)=\sin\nu\varphi$ and $g_\nu(\varphi)=\cos\nu\varphi$ corresponds to the odd modes or symmetric with respect to y-axis.

The eigenvalue equation is obtained by imposing the continuity of four components that are tangent to the interface. From eqn. (1.16 (a) and (b)) the e_z and h_z components are continuous at $r=\rho$. So we need only two other components to derive the eigenvalue equation. The result will be the same for eigenvalue equation, while choosing the azimuthal components e_φ and h_φ or the radial components $n^2 e_r$ and h_r [42]. The eigenvalue equation for the step-index fiber is [23, 42]

$$\left\{\frac{J_\nu'(U)}{UJ_\nu(U)}+\frac{K_\nu'(W)}{WK_\nu(W)}\right\}\left\{\frac{J_\nu'(U)}{UJ_\nu(U)}+\frac{n_{cl}^2}{n_{co}^2}\frac{K_\nu'(W)}{WK_\nu(W)}\right\}=\left(\frac{\nu\beta}{kn_{co}}\right)^2\left(\frac{V}{UW}\right)^4 \qquad (1.19)$$

This equation has discrete solutions giving the values of 'U' or equivalently the discrete values of 'β' since they are related. These solutions depend on the parameter ν and the core-clad refractive indices, as well as the waveguide parameter V. As an example the properties of the eigenvalue equation in two cases $\nu=0$ and $\nu\neq 0$ are discussed below.

In the case of $\nu=0$, the eqn. (1.18) has two different values for f_ν and g_ν, for even modes $f_0(\varphi)=1$ and $g_0(\varphi)=0$ and for odd modes $f_0(\varphi)=0$ and $g_0(\varphi)=1$. Substituting the even values of eqn. (1.18) into the eqns. (1.17) and (1.16 (a, b)), the field components $e_\varphi=h_r=h_z=0$, which represents the TM_{0m} mode because the longitudinal component of magnetic field 'h_z' is zero. Whereas for odd values of eqn. (1.18), the field components $e_r=h_\varphi=e_z=0$, which represents the TE_{0m} modes because the longitudinal component of electric field 'e_z' is

zero. In both cases, the other components of TM ($e_r = h_\varphi = e_z \neq 0$) and TE ($e_\varphi = h_r = h_z \neq 0$) modes are independent of 'φ' and therefore these modes possess circular symmetry. The eigenvalue equation for the TE_{0m} and TM_{0m} modes are obtained from the eqn. (1.19) by making the term $\nu = 0$. The eigenvalue equation for TE_{0m} and TM_{0m} modes are [23]

$$\frac{J_1(U)}{UJ_0(U)} + \frac{K_1(W)}{WK_0(U)} = 0 \tag{1.20}$$

$$\frac{n_{co}^2 J_1(U)}{UJ_0(U)} + \frac{n_{cl}^2 K_1(W)}{WK_0(U)} = 0 \tag{1.21}$$

From eqn. (1.20), the eigenvalue equation of TE_{0m} mode is independent of the core and cladding of the waveguide, so that the propagation constant 'β' is independent of the $\nabla_t \ln n^2$ term, which is equivalent to the scalar propagation constant '$\tilde{\beta}$' in the weakly guiding approximation (Sec 1.2.1).

For $\nu \neq 0$, none of the field components are zero and the eigenvalue equation is the same as the eqn. (1.19), and further simplification will give two real roots with '+' and '-' sign. By convention'+' sign represents the even and odd $EH_{\nu m}$ modes and '-' sign represents the even and odd $HE_{\nu m}$ modes, where the first subscript 'ν' represents the order and the second subscript 'm' denotes the m^{th} root of the eigenvalue equation. These modes have non zero component of e_z and h_z, due to which they are called hybrid modes [23]. The numerical solutions of eigenvalue eqns. (1.19), (1.20) and (1.21) will give the discrete 'β' values for $HE_{\nu m}$, $HE_{\nu m}$, TE_{0m} and TM_{0m} modes. The 'β' values for even and odd $HE_{\nu m}$ and $EH_{\nu m}$ modes are the same.

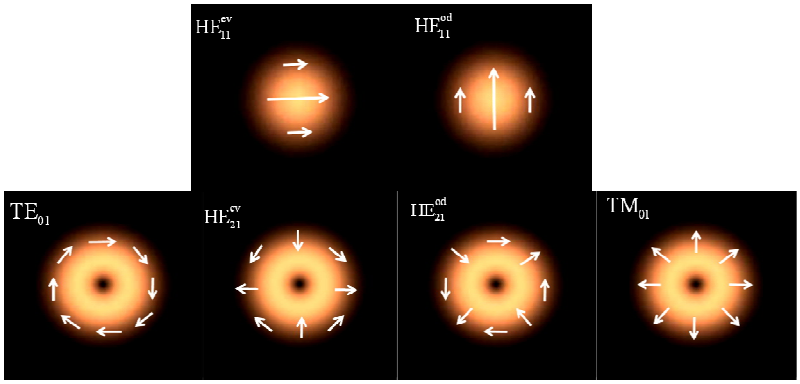

Figure 1.2: The guided vector modes of the step-index fiber with V=3.803.

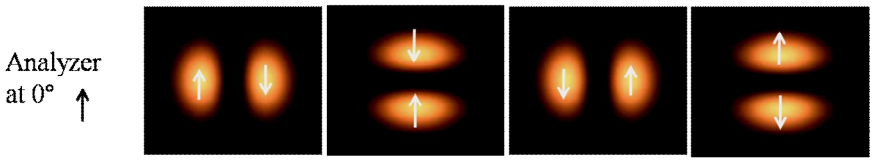

Figure 1.3: The two-lobe pattern of the vector modes after passing through the analyzer oriented at 0° for TE_{01} HE_{21}^{ev} HE_{21}^{od} and TM_{01} (from left to right) modes.

In this thesis, the fiber used to generate optical vector-vortex beams has the V value 2.484 <V< 3.832, and the corresponding guided vector modes are HE_{11}^{ev}, HE_{11}^{od}, TE_{01}, HE_{21}^{ev}, HE_{21}^{od} and TM_{01}. The corresponding propagation constant (β) values are represented as 'β' for an even and odd HE_{11} modes, $\beta_1 = \beta_3$ for the even and odd HE_{21} modes, β_2 for TM_{01} mode and β_4 for the TE_{01} mode [23]. The TE_{01}, HE_{21}^{ev}, HE_{21}^{od} and TM_{01} modes are called as annular modes due to their intensity distribution and are also known as 0^{th} order vector modes [43]. The electric field vector orientation across the beam cross section for all the modes are as shown in Fig.1.2 [23, 44]. Introducing an analyzer at the

fiber output end distinguishes the 0^{th} order or the annular modes experimentally. The vector modes after passing through the analyzer oriented at 0° is as shown in Fig.1.3, from this it is clear that two lobe pattern of TE_{01}, TM_{01} are orthogonal to each other and similar orientation for the HE_{21}^{ev}, HE_{21}^{od} modes. These modes are further distinguished by the analyzer rotation. For TE_{01} and TM_{01} modes, the two-lobe pattern rotates along with the analyzer rotation whereas for HE_{21}^{ev} and HE_{21}^{od} modes the lobes rotate opposite to the analyzer rotation.

1.2.1 Weakly guiding approximation

In the waveguide, polarization effects are governed by the $\nabla_t \ln n^2$ term in the vector wave equations (eqn. (1.11)). But when the core and cladding refractive indices are approximately equal (i.e. $n_{co} \approx n_{cl}$) or equivalently variation in the refractive index profile height parameter is small ($\Delta << 1$), the term $\nabla_t \ln n^2$ becomes negligible and the vector wave equation reduces to scalar wave equation. The approximation which involves $\Delta << 1$ is called the weakly guiding approximation. The term 'weak guiding fiber' is coined by Gloge [45], but the modes of weakly guiding step-index fiber were first reported by Snyder [46].

This approximation can be easily understood by the effect of polarization on the Fresnel reflection coefficients in a simple planar waveguide with refractive index n_1 and n_2. For TE and TM polarizations, the Fresnel reflection coefficients are [47].

$$r_{\perp} = \frac{\cos\theta_i - (n_2/n_1)\cos\theta_t}{\cos\theta_i + (n_2/n_1)\cos\theta_t}$$
$$r_{\parallel} = \frac{\cos\theta_i - (n_1/n_2)\cos\theta_t}{\cos\theta_i + (n_1/n_2)\cos\theta_t} \qquad (1.22)$$

where $r_{\parallel}$ and $r_{\perp}$ are the parallel and perpendicular components of the field and θ_i and θ_t are angle of incidence and transmission respectively. From eqn. (1.22) if $n_1 \neq n_2$ the two polarizations are reflected in different manner or equivalently the phase of the incident and reflected waves are different and increases as the difference between n_1 and n_2 increases. For $n_1 \approx n_2$ the two polarizations behave approximately the same way and the polarization effects can be ignored. In weakly guiding approximation, $n_1 \approx n_2$ and for the same reason the polarization effects are neglected.

In weakly guiding approximation the longitudinal components (e_z and h_z) of the field are small and negligible that the fields are practically transverse ($\mathbf{e}_t$ and $\mathbf{h}_t$), and the transverse electric and magnetic fields are related by

$$\mathbf{h}_t = \left(\frac{\varepsilon_0}{\mu_0}\right)^{1/2} n_{co}\hat{\mathbf{z}} \times \mathbf{e}_t \qquad (1.23)$$

By applying the conditions of weakly guiding approximation to eqn. (1.8) and by writing $\mathbf{e}_t$ and $\mathbf{h}_t$ as $e_x\hat{\mathbf{x}} + e_y\hat{\mathbf{y}}$ and $h_x\hat{\mathbf{x}} + h_y\hat{\mathbf{y}}$, it reduces to scalar wave equation:

$$(\nabla_t^2 + n^2k^2 - \tilde{\beta}^2)\left(\begin{Bmatrix} e_x \\ h_y \end{Bmatrix} \text{or} \begin{Bmatrix} e_y \\ h_x \end{Bmatrix}\right) = 0 \qquad (1.24)$$

where the '$\tilde{\beta}$' is the scalar propagation constant. The solution of the above

equation for both the pair of components are same and they are related to each other by eqn. (1.23), so that we need to solve either for e_x or e_y. Due to which the transverse fields of the fiber are assumed to be polarized in one direction. This is the reason the resultant modes are known as LP (linearly polarized) modes. Now we rewrite the solution of eqn. (1.24) in cylindrical polar coordinates and denoting $e_t(r,\varphi)=\psi(r,\varphi)=F(r)\Theta(\varphi)$.From the above discussion (Sec1.2) we know that 'φ' dependence will give solutions in $\cos l\varphi$ and $\sin l\varphi$, and the 'r' dependent part will give solutions in Bessel functions of the first and second kind in the core and cladding regions respectively. The final solution of eqn. (1.24) in cylindrical coordinates is

$$\psi(r,\varphi)=\begin{Bmatrix} \dfrac{AJ_l(\tilde{U}R)}{J_l(\tilde{U})}\begin{bmatrix}\cos l\varphi\\ \sin l\varphi\end{bmatrix}; & 0\le R<1 \\ \dfrac{BK_l(\tilde{W}R)}{K_l(\tilde{W})}\begin{bmatrix}\cos l\varphi\\ \sin l\varphi\end{bmatrix}; & 0\le R<\infty \end{Bmatrix} \qquad (1.25)$$

where $\tilde{U}$ and $\tilde{W}$ are the scalar dimensionless parameters defined as $\tilde{U}=\rho(kn_{co}^2-\tilde{\beta}^2)^{1/2}$ and $\tilde{W}=\rho(\tilde{\beta}^2-kn_{co}^2)^{1/2}$ and they are related to the normalized frequency as $V^2=\tilde{U}^2+\tilde{W}^2$. For the eigenvalue equation, in this case we need to check only the continuity of ψ and its first derivative $\dfrac{\partial\psi}{\partial r}$ at the core-cladding interface. After imposing these conditions on eqn. (1.25), the eigenvalue equation in the weakly guiding approximation is

$$\frac{\tilde{U}J_{l+1}(\tilde{U})}{J_l(\tilde{U})}=\frac{\tilde{W}K_{l+1}(\tilde{W})}{K_l(\tilde{W})} \qquad (1.26)$$

The eigenvalue equation is valid for both EH and HE modes. From eqn. (1.26), for *l*=1 the eigenvalue equation is the same as the eigenvalue equation of vector

TE mode (eqn. (1.20)), which implies that the TE mode has the same propagation constant in scalar as well as in vector treatment. The solution of eqn. (1.26) gives the scalar propagation constant ' $\tilde{\beta}$ '

$$\tilde{\beta} = \frac{V}{\rho(2\Delta)^{1/2}} \left\{ 1 - 2\Delta \frac{\tilde{U}^2}{V^2} \right\}^{1/2} \tag{1.27}$$

From eqn. (1.27), in weakly guiding approximation all the modes have the same propagation constant. The degeneracy in scalar propagation constants in the weakly guiding approximation is lifted by the polarization correction term through the perturbation method. This is based on the assumption that the circular cross section of the waveguide is slightly deformed which is equivalent to the small birefringence in the fiber [23]. The birefringent or the polarization correction to the scalar propagation constant is determined by taking the $\nabla_t \ln n^2$ term through perturbation method [23]. Hence, the exact propagation constant of the vector modes are the sum of scalar propagation constant and the polarization or the birefringent correction term $\delta\beta$ i.e. $\beta_i = \tilde{\beta} + \delta\beta_i$, where β_i is the vector propagation constant, $\tilde{\beta}$ is the scalar propagation constant and $\delta\beta_i$ is the corresponding polarization correction term to the i^{th} mode. The polarization correction ($\delta\beta$) term to the scalar propagation constant for fundamental, even and odd HE_{21}, TM_{01} and TE_{01}modes of step-index fiber are written as [23]:

$$\delta\beta = -\frac{(2\Delta)^{3/2}}{2\rho}\frac{\tilde{U}^2\tilde{W}}{V^3}\frac{K_0(\tilde{W})}{K_0(\tilde{W})}$$

$$\delta\beta_1 = \delta\beta_3 = -\frac{(2\Delta)^{3/2}}{2\rho}\frac{\tilde{U}^2\tilde{W}}{V^3}\frac{K_1(\tilde{W})}{K_0(\tilde{W})} \qquad (1.28)$$

$$\delta\beta_2 = -\frac{(2\Delta)^{3/2}}{2\rho}\frac{\tilde{U}^2\tilde{W}}{V^3}\frac{K_1(\tilde{W})}{K_2(\tilde{W})}$$

$$\delta\beta_4 = 0$$

From the above eqn. (1.28), the polarization correction to the TE_{01} mode is zero ($\delta\beta_4 = 0$), so it has the same propagation constant in vector as well as in scalar treatment as mentioned earlier.

1.2.2 Vector modes interms of linearly-polarized (LP) modes

In the weakly guiding approximation, the fiber modes are represented as linearly polarized LP_{lm} modes, where '*l*' is the azimuthal number and '*m*' is the radial mode order. Now we represent the first six guided modes of the step-index fiber interms of the combination of LP modes. From eqn. (1.25), for *l*=0, there are only two possible solutions which are $\psi_1 = \begin{pmatrix}1\\0\end{pmatrix} F_0(R)\exp(i\tilde{\beta}z)$ and $\psi_2 = \begin{pmatrix}0\\1\end{pmatrix} F_0(R)\exp(i\tilde{\beta}z)$, which are equivalent to the x and y polarized fundamental (Gaussian) mode of the fiber [23]. For *l*=1, the possible solutions are

$$\psi_1 = e_{ex} = \begin{pmatrix} \cos\varphi \\ 0 \end{pmatrix} F_1(R)\exp(i\tilde{\beta}z) \qquad \psi_2 = e_{ox} = \begin{pmatrix} \sin\varphi \\ 0 \end{pmatrix} F_1(R)\exp(i\tilde{\beta}z)$$

$$\psi_3 = e_{ey} = \begin{pmatrix} 0 \\ \cos\varphi \end{pmatrix} F_1(R)\exp(i\tilde{\beta}z) \qquad \psi_4 = e_{oy} = \begin{pmatrix} 0 \\ \sin\varphi \end{pmatrix} F_1(R)\exp(i\tilde{\beta}z) \tag{1.29}$$

Interms of the LP_{11} representation, the four solutions are denoted as LP_{11}^{ex}, LP_{11}^{ox}, LP_{11}^{ey} and LP_{11}^{oy} and are as shown in Fig.1.4

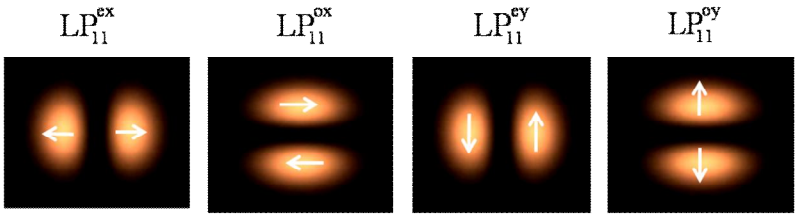

Figure 1.4: Linearly-polarized (LP) even and odd modes with x and y polarizations.

From Fig.1.4, the LP_{11} modes are four-fold degenerate, two fold in parity and two fold in polarization. The linear combinations of these modes through the symmetric and antisymetric combinations represent the first four annular modes of the fiber. The representation of the four guided vector modes of the fiber HE_{21}^{ev}, TM_{01}, HE_{21}^{od} and TE_{01} interms of the LP_{11} modes are as shown in Fig.1.5 and their corresponding electric field vectors are represented as [23]

$$\begin{aligned} e_{HE^{ev}} &= F_1(R)\{\cos\varphi\hat{x} - \sin\varphi\hat{y}\} \\ e_{TM_{01}} &= F_1(R)\{\cos\varphi\hat{x} + \sin\varphi\hat{y}\} \\ e_{HE^{od}} &= F_1(R)\{\sin\varphi\hat{x} + \cos\varphi\hat{y}\} \\ e_{TE_{01}} &= F_1(R)\{\sin\varphi\hat{x} - \cos\varphi\hat{y}\} \end{aligned} \tag{1.30}$$

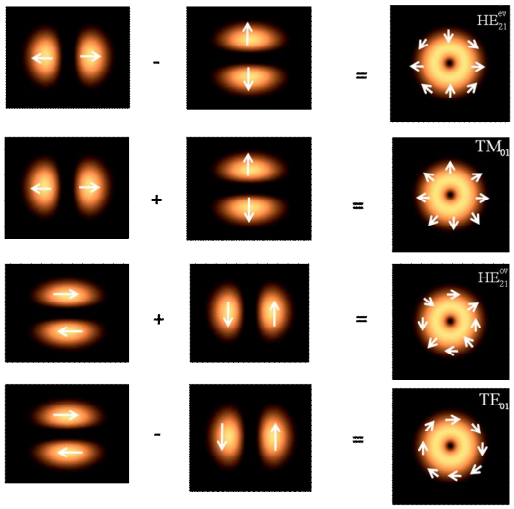

Figure 1.5: Representation of the guided vector modes interms of the LP mode combinations.

In principle, the vector modes have different propagation constants due to the polarization correction term $\delta\beta$ as discussed above, so none of the fields in eqn. (1.29) represent a guided mode of the fiber. However, the combination of guided modes results in the LP_{11} modes due to the beating between the different vector modes. For example, the LP_{11}^{ex} mode is formed due to the combination of HE_{21}^{ev} and TM_{01} vector modes at a particular length of the fiber, at which the beat length between the two vector modes is equal to the $2\pi/\delta\beta$, where $\delta\beta$ is the difference between the two propagation constants ($\delta\beta_1$ and $\delta\beta_2$) of the vector modes.

1.3 Vortex modes of step-index fiber

The formation of vortex modes in the fiber is understood by solving the vector wave equation in circular polarization basis or in the operator form in the

weakly guiding approximation [25, 26, 48]. In this section, we solve the vector wave equation in the operator form to obtain the vortex modes of the step-index fiber. After rearranging the vector wave equation (eqn. (1.16)), the eigen form of the transverse field is

$$\left(\nabla_t^2 + n^2k^2\right)\mathbf{e}_t + \nabla_t\left(\mathbf{e}_t \cdot \nabla_t \ln n^2\right) = \beta^2 e_t \tag{1.31}$$

where 'β^2' plays the role of eigenvalue and writing the above equation in a matrix form in the linear polarization basis,

$$\left(\hat{H}_0 + \hat{U}\right)\left|\begin{matrix} e_x \\ e_y \end{matrix}\right\rangle = \beta^2 \left|\begin{matrix} e_x \\ e_y \end{matrix}\right\rangle \tag{1.32}$$

where $\hat{H}_0 = \left(\nabla_t^2 + n^2k^2\right)\hat{\sigma}_0$ is the Hamiltonian, $\sigma_0 = \begin{pmatrix} 1 & 0 \\ 0 & 1 \end{pmatrix}$ is the identity matrix and $\hat{U} = \begin{pmatrix} \nabla_x g_x + g_x \nabla_x & \nabla_x g_y + g_y \nabla_x \\ \nabla_y g_x + g_x \nabla_y & \nabla_y g_y + g_y \nabla_y \end{pmatrix}$ is the perturbation part, from the gradient term and $g_\alpha = \dfrac{\partial \ln n^2}{\partial \alpha}$ with $\alpha = x, y$. The eqn. (1.32) in the circular basis is written as [26]

$$\left(\hat{H}_0 + \hat{V}\right)|\psi\rangle = \beta^2 |\psi\rangle \tag{1.33}$$

where $\hat{V} = \hat{\mathbf{D}} + \hat{\mathbf{T}}\hat{\mathbf{D}}$, $\hat{\mathbf{D}} = \dfrac{\nabla}{2}\dfrac{\partial f}{\partial r}\left(\hat{\sigma}_0 \dfrac{\partial}{\partial r} + \dfrac{i}{r}\hat{\sigma}_3 \dfrac{\partial}{\partial \varphi}\right)$ $\hat{\mathbf{T}} = \hat{\sigma}_1 \cos 2\varphi + \hat{\sigma}_2 \sin 2\varphi$, where $\sigma_1, \sigma_2, \sigma_3$ are the Pauli matrices, $|\psi\rangle = \left|\begin{matrix} e_+ \\ e_- \end{matrix}\right\rangle$ and $e_\pm = (e_x \mp i e_y)/\sqrt{2}$ is the circular basis. In the weakly guiding approximation, the operator $\hat{V}$ is relatively small because it originates from the gradient term and is equal to the polarization correction. In the scalar equation or the zero approximation to the

vector wave equation (eqn. (1.31)), it reduces to the form $H_o|\tilde{\psi}\rangle = \tilde{\beta}^2_{n,l}|\tilde{\psi}\rangle$, which is fourfold degenerate [49]. The perturbation term $\hat{V}$ removes the degeneracy and at the same time changes the structure of the ground state. In order to determine the correct structure of the ground state, the operator $\hat{V}$ should be in the basis of any four linearly independent solutions of the scalar equation that belongs to the same '$\tilde{\beta}^2_{n,l}$'. For which it is convenient to choose the four partial optical vortices $|\sigma, l\rangle$ as basis where σ is the sign of circular polarization (± 1) and the l is the orbital number (± 1) [25, 26]:

$$|\psi_1\rangle = |1, l\rangle, |\psi_2\rangle = |1, -l\rangle, |\psi_3\rangle = |-1, -l\rangle, |\psi_4\rangle = |-1, l\rangle \quad (1.34)$$

Using this basis the matrix elements of the perturbation matrix $\hat{V}$ are obtained using $\hat{V} = \frac{\langle i|\hat{V}|i\rangle}{\langle i / i\rangle}$ for a step-index fiber and using this relation we can find the four eigen vectors and their corresponding eigenvalues [26]. The eigenvalue gives the polarization correction to the modes. For a step-index fiber the corresponding vortex modes are written as [26]

$$|\psi_1\rangle = |1,1\rangle, |\psi_2\rangle = |-1,-1\rangle, |\psi_3\rangle = |1,-1\rangle + |-1,1\rangle, |\psi_4\rangle = |1,-1\rangle - |-1,1\rangle \quad (1.35)$$

The first two modes are circularly polarized OVs, formed due to the combination of HE_{21} even and odd vector modes due to the same propagation constant whereas, the other two modes are due to the combination of the two partial OVs, and the polarization structures of the $|\psi_3\rangle$ and $|\psi_4\rangle$ represents the TM_{01} and TE_{01} vector modes. From the above discussion the perturbation operator $\hat{V}$ acts both upon spatial and spin variables of the state vector $|\psi\rangle$, and hence the SOI is included in this operator [50, 51]. The energy flux of the

vortex modes (eqn. (1.35)) changes along the fiber for $|\psi_3\rangle$ and $|\psi_4\rangle$ states due to the different propagation constants of the TE and TM modes.

1.3.1 Vector modes interms of the vortex modes

From the above discussion, in an ideal fiber for *l*=1, the four circular polarized vortex modes with spin (σ) and orbital (*l*) momentum are represented as (1 1), (-1 -1), (1 -1) and (-1 1) (eqn. (1.34)). The first two vortices (1 1) and (-1 -1) correspond to the clockwise and counter clockwise fluxes respectively or in other words the spin and orbital circulations are in the same direction whereas for (1 -1) and (-1 1) vortices, the circulation of spin and orbital momentum are opposite to each other. The combination of (1 -1) and (-1 1) vortex modes forms TM_{01} and TE_{01} vector modes and the combination of (1 1) and (-1 -1) vortex modes form HE_{21}^{e} and HE_{21}^{o} vector modes. All the four combinations of the vortex modes, which form the vector modes are as shown in Fig.1.6. In a step-index fiber, the spin and orbital angular momentum are coupled together due to which the above discussed vortex mode combinations to form pure vector modes happen only at a particular length of the fiber. At all other lengths of the fiber two partial vortices with unequal intensities due to domination of one vortex over the other along the fiber length are present for the combination of TE and TM modes. In Chapter 3, we discuss more on our experimental results on the presence of two partial vortices in the combination of TE and TM modes and their behavior with respect to input wavelength.

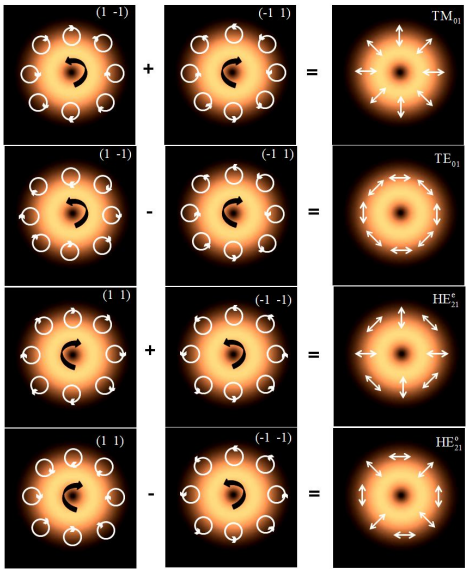

Figure 1.6: Formation of vector modes interms of the vortex modes, white circles correspond to spin rotation and black arrow corresponds to orbital rotation respectively.

1.4 Vector singularities in fiber modes

The formation and propagation of scalar and vector singularities of transverse field in free space were introduced and extensively studied by Berry, Nye and Hajnal [1-11]. Volyar and his group extensively studied the formation and the propagation of vector and vortex modes in the fiber through the vector (polarization) singularities [52-56, 24]. In this section, based on Volyar work, we introduce the singularities in vector modes based on the formation of scalar dislocations interms of the vector disclinations to better understand the results presented in this thesis.

The four LP_{11} modes (Fig.1.4) obtained in the weakly guiding approximation are classified into two pure scalar edge dislocations. The LP modes with x-polarization are denoted by D_x dislocation and the y-polarization

are denoted by D_y dislocation. However, in fibers the LP modes are formed due to the beating between the vector modes, and the scalar dislocation are not enough to understand the formation and propagation of LP modes completely, for which we need vector singularities. In order to understand vector singularities in LP modes, let us consider a vector LP_{11}^{ex} mode which is formed due to the beating between the HE_{21}^{ev} and TM_{01} vector modes. The electric field of the LP_{11}^{ex} mode is (Appendix 2)

$$LP_{11}^{ex} = \left\{\hat{\mathbf{x}}\cos(\varphi)\cos(\delta\beta_{21}z) + i\hat{\mathbf{y}}\sin(\varphi)\sin(\delta\beta_{21}z)\right\} F_1(R)\exp(i\beta' z) \qquad (1.36)$$

where $\hat{\mathbf{x}}$, $\hat{\mathbf{y}}$ are the unit vectors, $\delta\beta_{21}$ is half the difference between the polarization correction $[(\delta\beta_2 - \delta\beta_1)/2]$ of the TM_{01} and HE_{21}^{ev} modes, $F_1(R)$ is the radial distribution of the field and $\beta' = \tilde{\beta} + (\delta\beta_2 + \delta\beta_1)/2$ is the vector propagation constant of the LP_{11}^{ex} mode. The eqn. (1.36) contains two pure edge dislocations and one screw dislocation at different beating lengths of the fiber. The first dislocation is formed at the fiber beat length of $z = 2\pi/\delta\beta_{21}$, where the field becomes x-polarized as scalar LP_{11}^{ex} mode (D_x dislocation) and the other at $z = \pi/2\delta\beta_{21}$, where the field becomes y-polarized as scalar LP_{11}^{oy} mode (D_y dislocation). The beating length of $z = \pi/4\delta\beta_{21}$ forms a pure screw dislocation but the field in the transverse cross section is nonuniformly polarized due to the vector superposition of the two pure edge dislocations. The transformation of the scalar edge D_x dislocation to the D_y dislocation is understood interms of the vector disclination or the polarization singularities of

two circularly polarized components. For this eqn. (1.36) is written in the circular polarization basis as

$$LP_{11}^{ex} = \left\{\hat{e}^{+}\cos(\delta\beta_{21}z - \varphi) + \hat{e}^{-}\cos(\delta\beta_{21}z + \varphi)\right\} F_1(R)\exp(i\beta' z) \qquad (1.37)$$

The singularity condition, for the right circular polarization ($\hat{e}^{+}$) or in other words C^{-} disclination is that the amplitude of left circular component vanishes i.e. $\mathrm{Re}(e^{-}) = \mathrm{Im}(e^{-}) = 0$ and for the left circular polarization ($\hat{e}^{-}$) or the C^{+} disclination the right circular component vanishes i.e. $\mathrm{Re}(e^{+}) = \mathrm{Im}(e^{+}) = 0$. Similarly, the linearly polarized L_x and L_y disclinations are defined as for L_x disclination the $\mathrm{Re}(e_x) = \mathrm{Im}(e_x) = 0$ and for an L_y disclination the $\mathrm{Re}(e_y) = \mathrm{Im}(e_y) = 0$. By applying these conditions to the eqns. (1.36) and (1.37), the equations for C^{-}, C^{+}, L_x and L_y disclinations are

$$\varphi = \pm\pi/2 + \delta\beta_{21}z, \qquad \varphi = \pm\pi/2 - \delta\beta_{21}z$$

$$L_x;\varphi = 2n\pi, \qquad L_y;\varphi = (2n+1)\pi/2 \qquad (1.38)$$

From eqn. (1.38), the C^{-}, C^{+} disclinations have the longitudinal 'z' dependence whereas the L_x and L_y disclinations are independent of 'z'. This means that they are immobile or remain at the same position for the propagation of a mode through the fiber. The dynamics of propagation and the interaction between the C^{-} and C^{+} disclinations will decide the polarization and the orientation of the LP_{11} mode. In the case of LP_{11}^{ex} mode or the x-polarized D_x dislocation, it forms a two pure edge C^{-} and C^{+} disclinations and simultaneously immobile L_x disclination. The fiber of beat length $z = \pi/2\delta\beta_{21}$ and $\varphi = \pi/2$ and $3\pi/2$, the C^{-} and C^{+} disclinations move opposite to each other and annihilate to create

$-L_x$ disclination. The generated $-L_x$ disclination is anti-phase with the earlier located immobile L_x disclination and they both annihilate and give birth to the D_y dislocation or the LP_{11}^{oy} mode. At all other lengths of the fiber the output field is a superposition of C^-, C^+, L_x and L_y disclinations.

1.5 Vortex modes interms of the circularly polarized (CP) modes

The circularly polarized (CP) modes with pure edge dislocation are formed due to the combination of two orthogonal linearly polarized (LP_{11}) modes with relative phase shift $\pi/2$ and same parity. From the four LP_{11} modes, we can construct four possible degenerate CP_{11} modes of different parity and direction of circulation, which are shown in Fig.1.7. The electric field of these modes is written as

$$\begin{aligned} e_t(CP_{11}^{e+}) &= e_t(LP_{11}^{ex}) + ie_t(LP_{11}^{ey}) \\ e_t(CP_{11}^{o+}) &= e_t(LP_{11}^{ox}) - ie_t(LP_{11}^{oy}) \\ e_t(CP_{11}^{e-}) &= e_t(LP_{11}^{ox}) - ie_t(LP_{11}^{oy}) \\ e_t(CP_{11}^{o-}) &= e_t(LP_{11}^{ox}) + ie_t(LP_{11}^{oy}) \end{aligned} \tag{1.39}$$

From the above discussion (Sec 1.4) each LP_{11} mode is formed due to the interaction between the C^- and C^+ disclinations which form either L_x or L_y disclination. Since the CP mode is a combination of two orthogonal LP modes, which forms two C^+ and two C^- disclinations, the interaction between these disclinations form L_x and L_y disclination. If the L_x and L_y disclinations are collinear they form the pure edge circularly polarized (CP) dislocation and if, they are orthogonal to each other they form a pure screw dislocation.

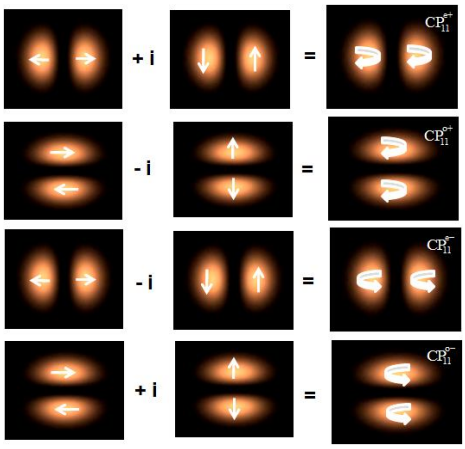

Figure 1.7: Representation of CP_{11} modes interms of the LP_{11} modes

In a step-index fiber the beat length which is equal to $z = 2\pi / (\delta\beta_{21} - \delta\beta_{43})$ forms a pure circularly polarized edge dislocation (CP_{11}) whereas for the other lengths of the fiber the output mode is a combination of two elliptically polarized regions separated by the L_x and L_y disclinations. In chapter 3 we measured these vector singularities during the transformation of right elliptically polarized even mode (EP_{11}^{e+}) to the left elliptically polarized even mode (EP_{11}^{e-}) by changing the input wavelength.

Now let us write the combination of degenerate even and odd CP_{11} modes with same circulation and $\pm\pi$ phase shift to form a circularly polarized vortex modes with helicity ($\sigma = \pm 1$) and topological ($l = \pm 1$) charges. These CP mode combinations are helpful to understand the formation of circularly polarized vortex modes in the fiber. In the pair of numbers (σ, l) the four possible combination are (1, 1), (-1, -1), (1, -1) and (-1, 1). In a step-index fiber the first two combinations are formed due to the combination of even and odd HE_{21}

vector modes and the other two combinations are formed due to the combination of TE_{01} and TM_{01} modes. In Chapter 4, the combination of vector modes to form vortex mode (eqn. (1.40)) are used to explain our experimental results on the generation of isolated polarization singularities. The four combinations of vortex modes are shown in Fig.1.8 and are represented as

$$\begin{aligned} HE_{21}^{e} - iHE_{21}^{o} &= CP_{11}^{e+} + iCP_{11}^{o+} \\ HE_{21}^{e} + iHE_{21}^{o} &= CP_{11}^{e-} - iCP_{11}^{o-} \\ TE_{01} - iTM_{01} &= CP_{11}^{e+} - iCP_{11}^{o+} \\ TE_{01} + iTM_{01} &= CP_{11}^{e-} + iCP_{11}^{o-} \end{aligned} \tag{1.40}$$

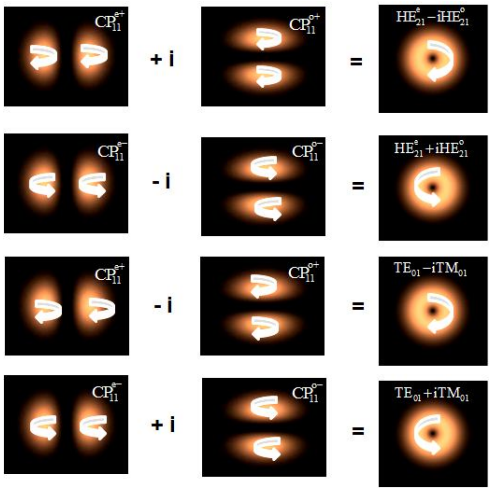

Figure 1.8: Representation of circularly polarized vortex modes interms of the CP_{11} modes.

Chapter 2

Generation and Characterization of Vector-vortex Beams

In this chapter, we first present the literature on different methods to generate cylindrical vector beams using active and passive optical components. In this context we present our experimental results on the generation of cylindrical vector-vortex beams using a two-mode optical fiber and switching between the different VV mode combinations. The VV beams are generated using a two-mode step-index optical fiber by coupling the Gaussian beam into the fiber as skew-offset beam. The vector nature of the output modes are analyzed by the rotating analyzer at the output end of the fiber and the vortex nature of the modes are identified by constructing a two-beam interferometer. The switching between the different VV beams are achieved (i) by changing the input launch angle to a diametrically opposite position in the fiber cross-section and (ii) by changing the input quarter wave plate to launch right and left circularly polarized light for both input launch angles. In this case the lateral and angular shifts of the four output beams are analyzed using the weighted average method. Further, the spatial polarization across the beam cross section of VV beams are manipulated by a combination of two HWPs at the fiber output end to get the pure cylindrical VV beams. We also qualitatively address the role of different experimental parameters such as the fiber length and numerical aperture (NA) on the generation of vector-vortex beams.

2.1 Introduction

In recent years the generation of azimuthally polarized TE_{01} and radially polarized TM_{01} or their combination received a lot of interest due to their spatial polarization properties. These beams are called cylindrical vector (CV) beams due to their cylindrical symmetry in the electric or the magnetic fields in the beam cross section. The linear combination of TE and TM modes are known as generalized vector beams. There are many active and passive methods to generate these CV beams detailed in Refs [19, 20]. In the active methods, the CV beams are generated inside a laser cavity using intracavity devices such as axial birefringent / dichroic components to provide the necessary mode discrimination. For example, by using a calcite crystal as intracavity axial birefringent material CV modes were generated by Pohl [57], and this method was extended further in [58, 59], and to improve the efficiency of generation [60, 61]. The other methods used to generate CV beams including using a conical axicon [62] Brewster angle reflector [63, 64], polarization sensitive cavity mirrors [65], and intra cavity interferometric method [66].

In the passive method, the CV beams are generated outside the cavity. In general, these methods convert the commonly known spatially homogeneous polarization into the spatially inhomogenous CV polarization. The CV modes are generated using birefringent or dichroic radial polarizers [67, 68], liquid crystal SLM [69], combining HG_{01} and HG_{10} modes through an interferometric method [70], space varying sub-wavelength gratings [20], several segmented $\lambda/2$ or $\lambda/4$ plate for a linear or circular polarized beams [71, 72]. Interestingly, optical fibers are used both as active and passive element to generate CV beams [31, 33, 73].

In all the methods discussed above, apart from the sub-wavelength grating, the generated CV beams don't carry helical phase structure and have only the polarization singularities. The polarization singularities of these beams were also studied under the high focusing lens [74-76].

2.2 Generation of cylindrical vector beams using optical fiber

As discussed in Sec 1.2.2, the two-mode optical fiber supports six waveguide modes [23] of which the four 0^{th} order guided modes (HE_{21}^{e}, TM_{01}, HE_{21}^{o} and TE_{01}) are singular or annular modes. These modes are reminiscent of the CV beams due to their spatial polarization structure. The radial (TM_{01}) and azimuthal (TE_{01}) modes are cylindrically symmetric in polarization and the HE_{21}^{e}, HE_{21}^{o} modes are hybrid in polarization. The power distributions of the fundamental and annular modes across the cross section of the fiber are different. For the fundamental mode optical power concentrated on the axis whereas for the annular modes the optical power is distributed in a doughnut shape around the axis. By illuminating the fiber with a Gaussian beam with an off-axis and tilt (Fig.2.1(c, d)) or the on-axis coupling of externally generated LG_{01} beam into the fiber, the four annular modes are excited in the fiber with negligible fundamental mode.

By tuning the input Gaussian beam polarization and the input launch angle or by selecting the appropriate phase and polarization of the input LG_{01} beam we can selectively excite the desired annular mode or the combination of annular modes out of four possible guided modes [31-33]. This is a simple and inexpensive method to generate CV beams and also the beams generated using this method are highly stable making it suitable for several applications.

Grosjean et al. [31, 32] generated these fiber modes using an all fiber device in which light from a single mode fiber is coupled into the two mode fiber through index matching liquid. By misaligning the two fibers, annular modes are excited. In this experiment it was observed that when the two fibers are shifted in the direction of the incident beam the TM_{01}beam is generated whereas for a perpendicular shift TE_{01} beam is generated and for other shifts HE_{21} beam is obtained. Later on Volpe et al., [33] increased the purity and efficiency of the mode generation by coupling the externally generated Laguerre-Gaussian (LG) beam into the two-mode fiber through on axis coupling. When the input LG mode has opposite signs of circular polarization ($\sigma = \pm 1$) and helical phase structure ($l = \mp 1$),TE_{01} and TM_{01} modes with same efficiency are excited with a constant phase of $\pi/2$ in the fiber whereas for the same sign of circular polarization ($\sigma = \pm 1$) and helical phase structure ($l = \pm 1$), HE_{21}^{e} and HE_{21}^{o} modes are excited in the fiber with same efficiency and with constant phase of $\pi/2$. At appropriate lengths of the fiber the input LG beam is converted into generalized CV beams.

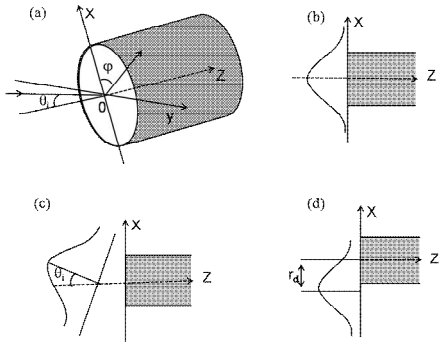

Figure 2.1: (a) Fiber cross section with coordinates and incident angle, θ_i, (b) on-axis launching of the Gaussian beam (c) tilted (θ_i) illumination of Gaussian beam (d) offset (r_d) illumination

In our method, we excite the different combinations of the guided modes in a two-mode step-index circular core optical fiber using a Gaussian beam from the He-Ne laser as skew-offset beam. By keeping the input end of the fiber at the focal plane of the microscopic objective lens and giving tilt and /or offset to the fiber or to the input beam (Fig.2.1(c, d)) we selectively excite 0^{th} order vector mode combinations in the fiber. Further, an optimum condition for the desire mode excitation is achieved by varying the input beam polarization and the fiber length. In this method, the coupling of the input Gaussian beam as off/set skew beam always excites vortex modes along with the vector modes. Hence, the output modes of the fiber have both vector and vortex nature. This method has significant advantage as far as generation of polarization singularities such as two C-points and a single C-point and switching between the different topological charges of the C-points in the output beam are concerned. The presence of two partial vortices in the output beam forms two C-points and the coherent superposition of the fundamental mode with the vortex modes form isolated C-point which are discussed in Chapters 3 and 4.

2.3 Experimental details

A schematic of the experimental setup used for controlled generation of cylindrical VV beams and switching between the different VV beams using linearly and circularly polarized Gaussian beam is shown in Fig. 2.2 (a). Partially polarized Gaussian (TEM_{00}) beam from the He-Ne laser (λ= 632.8 nm) pass through a Glan-Thompson polarizer (P) to obtain linearly polarized light. The linearly polarized light then passes through a half-wave plate (HWP) or a quarter wave plate (QWP) mounted on a rotation stage to enable adjustment of the polarization of the beam launched into the fiber. The beam

after passing through the polarization components is focused using a 0.25 NA 10x microscope objective lens (L_1) onto the cleaved end of the fiber, positioned using a three-axis ultra positioner stage. The *V* number of the circular core step-index optical fiber, calculated using the available fiber parameters is 3.805, implying that the fiber will support two LP modes, the fundamental LP_{01} mode and the first higher-order LP_{11} mode [23]. The TMF is kept horizontal with reduced twist, and bend along its length. By adjusting the position of the focused input beam with respect to the fiber axis we launch skew beam into the fiber. The angular tilt of the input beam to excite the vector-vortex modes are measured as follows: for linearly polarized input beam, starting from the maximum output intensity measured for on-axis Gaussian beam illumination the fiber input end is carefully adjusted for off axis illumination using the *x*- and *y*-axis controls to get the desired LG_{01} output beam. By measuring the half-width at half-maximum (HWHM) of the output Gaussian and LG beams directly using a CCD camera, connected through an IEEE 1394 card to the computer, positioned at 80 mm from the fiber tip we determine an angular tilt in the input beam of 30 μrad from the on-axis position to achieve the desired LG_{01} output beam. The TMF output intensity is then collimated using a lens (L_2) and imaged using the CCD for data acquisition and analysis. A rotating analyzer (A) at the fiber output end is used to characterize the polarization content of the output beam for a fixed input beam polarization. A two-beam interferometer is constructed in parallel using two beam splitters and two mirrors (BS_1, BS_2 and M_1, M_2) to verify the presence of transverse and longitudinal OV in the output beam [29, 30].

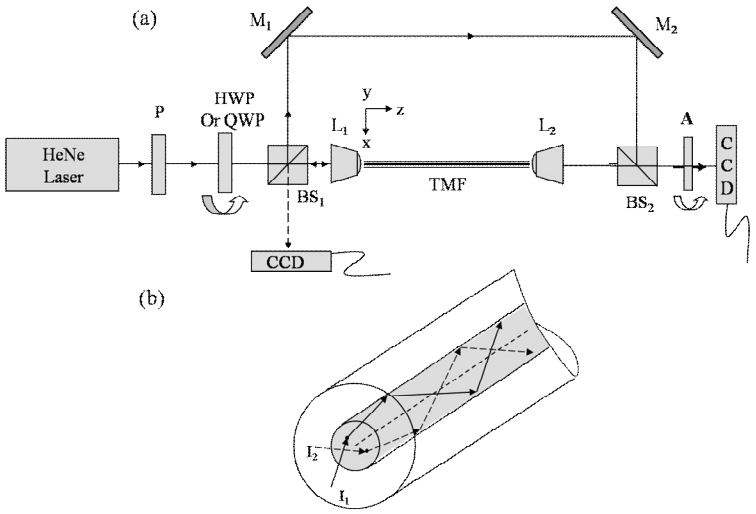

Figure 2.2: (a) Schematic of the experimental setup used for the generation and characterization of OVVBs. P-polarizer; HWP-half-wave plate; L_1, L_2 -lenses; BS_1, BS_2 - 50-50 beam splitters; M_1, M_2 - mirrors; TMF -two-mode fiber; A -analyzer; CCD -digital camera. (b) Two different launch angles with respect to the fiber axis

2.4 Results and discussion

2.4.1 Generation of vector-vortex beams

For the input HWP oriented at 0°, the vertical linearly polarized Gaussian beam is coupled into the fiber, by placing its cleaved end at the focal point of the objective lens (L_1) and adjusting the fiber 'x' and 'y' positions to a particular angle such that skew beam is coupled into the fiber. The fiber output is a HG_{10} beam as shown in Fig.2.3 (a). Now by fixing the fiber input launch angle, the input HWP is rotated in steps of 5° from θ =0° to 90° and the resulting intensity patterns for every 10° are shown in Fig.2.3(a)–(j). Counterclockwise (CCW) rotation of the input beam polarization results in CCW rotating and a dramatically changing output beam pattern. As a function of the plane of

polarization of the input beam the output HG_{10} beam (at θ =0°) transforms into an LG_{01} beam for θ =35° and a tilted HG beam for θ=60° before returning back to the HG_{10} beam for θ =90°. The behavior of the output intensity pattern repeats itself for larger rotation angles of the HWP. The behavior of the output beams for different input polarization with same input launch angle is due to the polarization selectivity of the guided vector modes [22, 23].

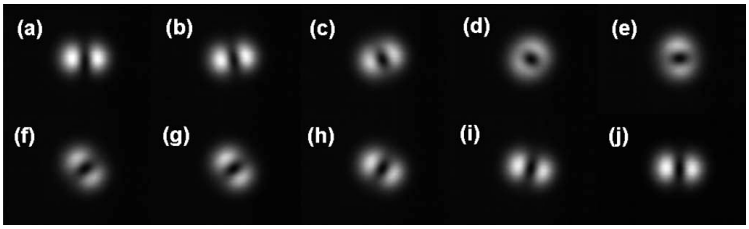

Figure 2.3: Intensity pattern at the fiber output as a function of input HWP angle 'θ'. (a) – (j) θ = 0° –90° in steps of 10°.

The polarization content of the HG and LG output beams are then analyzed by rotating the analyzer kept at the output end of the fiber. The HG_{10} and LG_{01} modes for every 45° of analyzer rotation are as shown in Fig.2.4. From the output beam behavior, it is clear that the output HG_{10} mode is LP_{11}^{ex} mode and it is formed due to the beating between the HE_{21}^{e} and TM_{01} guided vector modes. For the LG_{01} mode, the two-lobe pattern after the analyzer rotates in the same sense (CCW) as the analyzer. Further, for the analyzer at 0° the null line between the two lobes makes 45° in the clockwise direction (Fig.2.4). This behavior indicates that the fiber output is due to the linear combination of radially and azimuthally polarized TM_{01} and TE_{01} modes excited within the fiber with same phase.

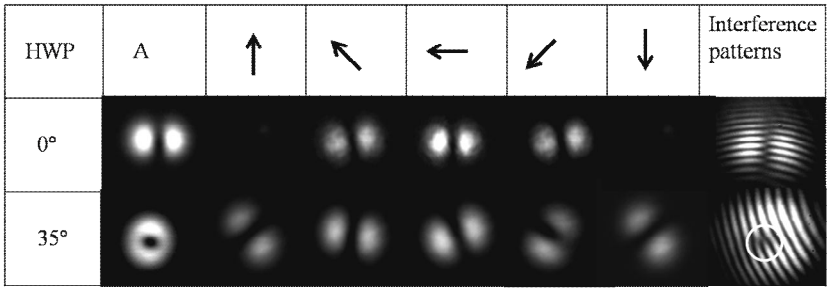

Figure 2.4: Fiber output as function of analyzer rotation for HG_{10} and LG_{01} output beams and their corresponding edge and fork interference patterns.

The corresponding interference patterns for the two output beams shows the pure edge and screw dislocations as shown in Fig.2.4. The interference forklet pattern is due to the combination of TE and TM modes (partial vortices) to form the helical phase structure and hence the forklet pattern. The complete polarization information and the presence of partial vortices in the beam cannot be obtained from the analyzer rotation alone and we need special techniques such as Stokes parameter method and state of polarization map at each and every point of the beam, which we discuss in the Chapter 3. At the other input polarizations the output beams are due to the simultaneous excitation of different vector-vortex modes and they possess polarization singularities across the beam cross section because of the different propagation constants of the excited modes.

Further, we plot the measured intensity variation as a function of analyzer rotation (from 0° to 360°), for three output beams from the fiber as shown in Fig.2.5.The intensity variation of the HG_{10} mode shows sinusoidal oscillation with maximum contrast for analyzer rotation as shown in Fig.2.5 (triangles) which confirms further that the output mode is linearly (x) polarized even (LP_{11}^{ex}) mode. For an in phase TE_{01} and TM_{01} mode combination the small

intensity variation of the two lobes as a function of the analyzer angle (Fig.2.5) is possibly due to the variation in the state of elliptical polarization across the beam cross section. The resulting (linearized) polarization vectors for this mode are shown in Fig.2.5 inset.

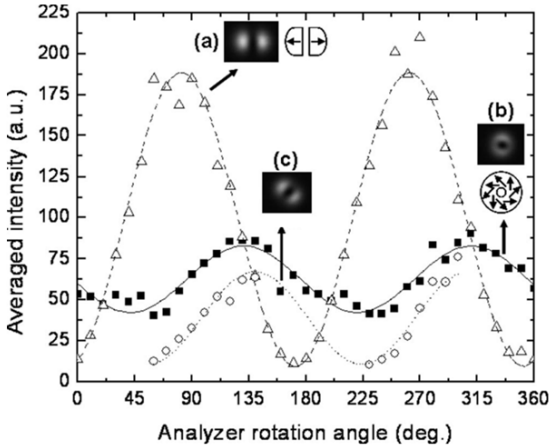

Figure 2.5: Average beam intensity as a function of analyzer rotation angle for the different output beams. HG_{10} =0° (open triangles), LG_{01} =35° (filled squares), and tilted HG_{01} =65° (open circles). The symbols are fitted to a sinusoidal curve. The beam patterns and the corresponding field vectors are given in the insets.

When the HWP is oriented at 65°, the resulting tilted HG beam after passing through the rotating analyzer shows little rotation from its position along with the intensity variation. This behavior is due to the presence of the vector singularities (or disclinations) across the beam cross section. In this case we plotted only the intensity variations in the intervals 45°–135° and 225°–315°, of the analyzer orientation (Fig.2.5, open circles) where the beam shift from its position is very less.

Now, changing the input launch condition by adjusting the fiber 'x' and 'y' positions for input HWP at 0° the output is a HG_{01} beam. The different output modes (HG_{10} and HG_{01}) for the same input polarization are possible due

to the change in the input cone angle of the skew-offset beam with respect to fiber axis [22, 23, 31]. Without changing the input launch angle, HWP is rotated upto 90° insteps of 10°. The output modes are as shown in Fig.2.6.

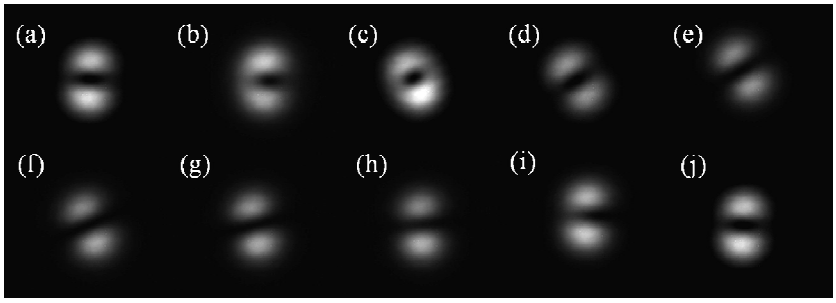

Figure 2.6: Intensity pattern at the fiber output as a function of HWP rotation. (a) – (j) $\theta = 0° – 90°$ in steps of 10°.

In this case, for the input HWP at 22.5°, the output beam passing through a counter clockwise rotating analyzer results in the two-lobe pattern rotating in opposite direction to the analyzer rotation as shown in Fig.2.7. This implies that the output beam is a combination of even and odd HE_{21} modes. The intensity variation in the two lobe pattern for different analyzer orientation is due to the simultaneous presence of the other fiber modes. In this case also the presence of the vortex character in the output beam shows up as up forklet.

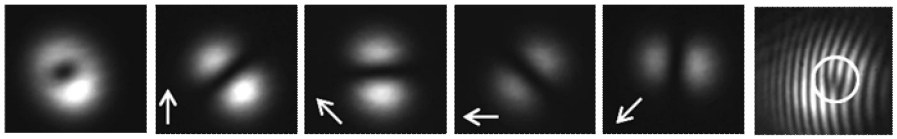

Figure 2.7: For a counter clockwise rotation of analyzer the two lobe pattern rotates in a clockwise direction and the corresponding interference fork pattern shows the helical phase structure.

From the above two cases, it is clear that by changing the input launch conditions for the same input polarization two different mode combinations can be excited in the fiber. The rotation of the HWP for the two different launch

angles results in TE and TM modes excited for the HWP orientation at 35° with HG_{10} mode as the starting mode whereas even and odd HE_{21} mode combination is excited for the HWP at 22.5° with HG_{01} as the starting mode. In both the cases the presence of partial vortices in the output beam shows up as down and up forklet patterns.

2.4.2 Switching between different vector-vortex beams

The experimental method used to switch between the different vector-vortex beams is shown in Fig.2.2 (a, b). Starting from adjusting the fiber input end to achieve maximum output intensity corresponding to on-axis illumination of circularly polarized input Gaussian beam the fiber position is carefully adjusted for an off-axis and tilted illumination using the x-and y-axes controls to selectively launch skew beam into the fiber and hence to get the desired 'doughnut' output beam for a fixed input beam polarization. In this case we measured the tilt angle using the back-reflected beam from the fiber input end, imaged using the CCD camera positioned at 137.3 cm. The measured angular tilt in the input beam are -27 μrad and 34.3 μrad respectively for doughnut output beams with respect to the Gaussian output beam, for the two input beam positions of I_1 and I_2 (Fig.2.2(b)).

Switching between the different VV beams is achieved using the input QWP: the QWP oriented at 45° with respect to the polarizer direction results in right-circular polarized (RCP) light which is first launched into the TMF at -27 μrad angle corresponding to I_1 shown in Fig.2.2 (b). The output doughnut beam (row 1 of Fig.2.8) upon passing through a vertically oriented analyzer results in a two-lobe pattern with its null line making 45° in the clockwise (CW) direction. Rotating the analyzer axis in the counter-clockwise (CCW) direction

results in the two-lobe pattern rotating in the same sense (row 1 of Fig.2.8) indicating that the output doughnut beam is due to the linear combination of radially and azimuthally polarized TM_{01} and TE_{01} modes ($TM_{01} - TE_{01}$) excited with same phase in the TMF [23, 33]. A small variation in the lobe intensity as a function of the analyzer rotation is possibly due to the contribution from the residual fundamental HE_{11} mode excited simultaneously in the fiber. Interference of this beam with the reference beam shows a downward forklet (Fig.2.9 (e)) indicating the presence of vortex in the beam. The corresponding electric field pattern is shown in Fig.2.9 (a).

Without disturbing the fiber input launch condition the QWP is rotated to 135° and the resulting left circularly polarized (LCP) light excites different waveguide modes in the fiber as evidenced by the behavior of the output doughnut beam with respect to the rotating analyzer (row 2 of Fig.2.8). For the doughnut beam excited by the LCP Gaussian input light, the vertical analyzer axis orientation results in two lobes with vertical null line and a CCW rotation of the analyzer axis results in the two-lobe HG_{10} pattern rotating in the opposite, CW sense. This behavior of the output LG_{01} beam from the TMF is an odd HE_{21} hybrid eigen mode of the waveguide excited in the fiber (Fig.2.8 (b)). Now, interference of this vector beam with the reference beam, confirms the presence of on-axis screw dislocation via the appearance of a single downward forklet as shown in Fig.2.9 (f). From the two outputs (for QWP at 45° and 135°), it is clear that just by rotating the QWP between 45° and 135° the resulting right and left circular polarized input skew ray launched into the TMF results in characteristics due to the different modes excited in the fiber. Both the beams have the same helical structure (down forklet) due to the same skew angle for

the inputs but the different vector nature is due to the polarization selectivity of the fiber modes.

In addition we also explored the effect of changing the skew ray launch angle as discussed above with respect to the fiber axis and its effect on the characteristics of the generated beams. By adjusting the x and y-axis controls of the fiber input end we move the launch angle to 34.3 μrad with respect to the fiber axis corresponding to the skew ray I_2 shown by dotted line in Fig.2.2 (b). This launch condition results in a completely different behavior of the vector-vortex beams generated for RCP and LCP input beam. For the RCP input Gaussian beam the output doughnut beam, after passing through vertically oriented analyzer results in two-lobe pattern with a horizontal null-line (row 3 of Fig.2.8). Subsequent CCW rotation of the analyzer axis results in a CW rotation of the two-lobe pattern, characteristic of the even hybrid mode (HE^{e}_{21}) excited in the TMF. It is obvious that there is a $\pi/2$ phase difference between the two-lobe HG_{10} and HG_{01} beams corresponding to the I_1 and I_2 skew rays launched into the TMF for vertical orientation of the analyzer axis. In addition, the two-lobe intensity pattern rotates in CW for a CCW rotation of the analyzer, implying that the beam generated corresponds to even HE_{21} waveguide mode, as shown in Fig.2.9 (c). The interference of this beam with the reference beam results in an upward forklet (Fig.2.9 (g)) due to the skew ray I_2 launched from the opposite side of the fiber axis. Similar to the change in the forklet direction – from upwards to downwards or vice-versa – reported for a change in the direction of the reference beam [77] we report here the change in the direction of the input Gaussian beam with respect to the fiber axis for generating the LG_{01} beam results in the flipping of the forklet direction (from downwards to upwards) due to the excitation of the vector-vortex beams with

opposite topological charges. The reversal of the vortex charge sign for the two input beams I_1 and I_2 is simply due to an image inversion in geometrical optics, similar to the results of Molina-Terriza et al., [78].

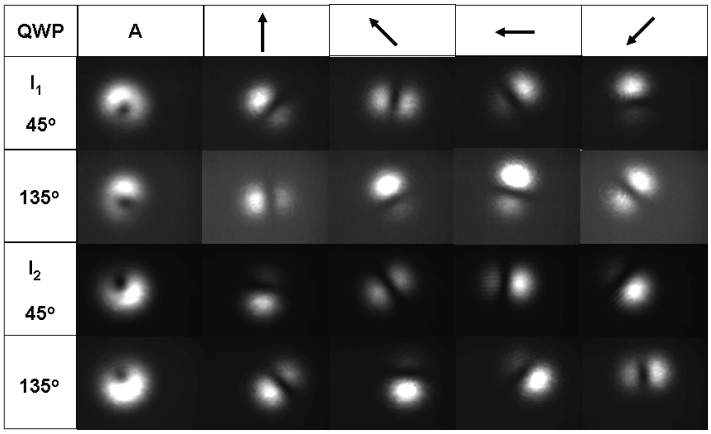

Figure2.8: VV beams generated for two different QWP orientations (45° and 135°), and two input beam positions (I_1 and I_2) and the corresponding behaviour as a function of the analyzer axis orientation.

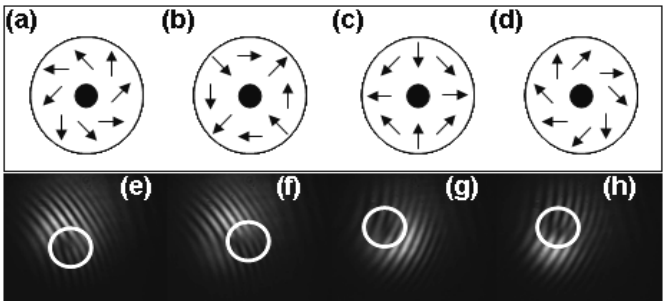

Figure 2.9: Row 1: Electric field distribution of the VV beams for the two different QWP orientations and two input beam positions. Row 2: the corresponding two-beam interference patterns.

Next, by keeping the input beam launch condition the same (I_2), rotating the QWP to 135° the behavior of the resulting LG_{01} beam after passing through the rotating analyzer shown in row 4 of Fig.2.8 corresponds to the linear

combination of TM_{01} and TE_{01} waveguide modes (TM_{01} + TE_{01}) but with $\pi/2$ phase difference compared to that shown in row 1 of Fig.2.8. The resulting generalized vector-vortex beam rotation sense for CCW rotation of the analyzer axis is opposite to that reported earlier. The electric field pattern corresponding to the generalized VV beam is shown in Fig.2.9 (d). As before, the two-beam interference of this LG_{01} VV beam with the reference beam results in a single upward directed forklet (Fig.2.9 (h)). Similar to what was mentioned earlier, changing the QWP orientation between 45° and 135° (corresponding to RCP and LCP input Gaussian light) it is possible to switch between the different VV beams respectively generated using a TMF. The sense of rotation of the vector-vortex beams for a fixed orientation of the QWP however is opposite for the two input launch conditions I_1 and I_2 with respect to the fiber axis indicating clearly that the reversal of the topological charge is simply due to the image inversion [77].

2.4.3 Weighted average analysis

We further analyze the changes observed in the output beam pattern for the four beams generated as a function of the change in the input beam polarization (from RCP to LCP) and as a function of the launch angle with reference to the fiber axis. Custom Matlab program was written to calculate the weighted average (centre of gravity) and the tilt angle of the beam. The weighted average of the doughnut beams were calculated by using

$$X_c = \sum x_i \frac{I(i,j)}{\sum I(i,j)} \quad ; \qquad Y_c = \sum y_i \frac{I(i,j)}{\sum I(i,j)}$$

where x_i and y_j are the pixel numbers and I(i, j) are the intensities of the corresponding pixel number. The X- and Y-axes are then drawn through the

centroid of the doughnut beam as shown in Fig.2.10. We then find the average high intensity and average low intensity (null of the doughnut beam) pixels within the doughnut beam and then draw a straight line connecting the high and low intensity pixels. This line passing through the centroid horizontal axes, with respect to which we calculate the slope. The slope is calculated using the formula $\phi = \arctan\left(\frac{y_2 - y_1}{x_2 - x_1}\right)$, where (x_1,y_1) and (x_2,y_2) are the pixel numbers of the low and high intensities of the doughnut beams respectively.

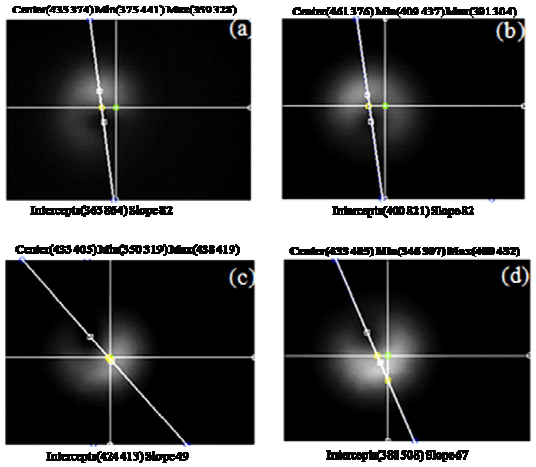

Figure 2.10: Weighted average analysis of the four output OVV beams

The analysis figures shown in Fig.2.10 (a – d) correspond to the beams shown in Fig.2.8. It is interesting to see that the doughnut beams (Fig.2.10 (a) and (b)) corresponding to the same input angle of -27 µrad have same slope of 82° but have different weighted average beam centers of (435, 374) and (461, 376) respectively for the LCP and RCP polarization of the input beam, corresponding to a change in the weighted centre of (26, 2). This implies that

there is a transverse shift in the output beam position with respect to the change in the input beam polarization but no angular rotation of the beam. However, when we changed the input beam angle to 34.3 μrad on the opposite side of the fiber axis, the output doughnut beams (Fig.2.10 (c) and (d)) have the same weighted average centers of (433, 405) but now they have different slopes with respect to the horizontal axis. The slope changes from 49° to 67° for a change in the input beam polarization (from LCP to RCP), a difference of 18°. This corresponds to the fact that in this case, there is no transverse shift in the beam but the output beam rotates angularly while changing the polarization of the input beam.

2.4.4 Conversion of generalized vector-vortex beams to cylindrical vector-vortex beams

The conversion of generalized vector-vortex beams into the cylindrical VV beam is achieved using a combination of two half wave plates [79]. In principle a single HWP rotates the initial polarization state by 2θ, which for an inhomogeneous polarized input beam will give different amount of rotation to different parts of the beam. But the combination of two HWP results in a pure polarization rotator. This feature of using two HWP can be understood by using the corresponding Jones matrices. The total effect of the two wave plates is

$$T = R(-\theta_2)\begin{pmatrix} 1 & 0 \\ 0 & -1 \end{pmatrix} R(\theta_2) R(-\theta_1) \begin{pmatrix} 1 & 0 \\ 0 & -1 \end{pmatrix} R(\theta_1)$$

where $R(\theta_1)$ and $R(\theta_2)$ are the rotation matrices for the two HWPs. After simplification, we get

$$T = \begin{pmatrix} \cos 2(\theta_2 - \theta_1) & -\sin 2(\theta_2 - \theta_1) \\ \sin 2(\theta_2 - \theta_1) & \cos 2(\theta_2 - \theta_1) \end{pmatrix}$$

(or)

$$T = R[-2(\theta_2 - \theta_1)]$$

From this it is clear that the combination of two HWPs works as a pure polarization rotator and irrespective of the initial polarization state of the input beam or its inhomogeneity in polarization, the polarization state of the output beam is rotated by the relative angle between the two HWP $2(\theta_2 - \theta_1)$ i.e., all the electric vectors are rotated by the same amount. The polarization state of the two generalized VV beams shown in the Figs.2.4 and 2.7, are converted into pure CVV beams using the two HWP combination. The output beams after passing through the two HWP combination is shown in Figs.2.11 and 2.12, for different relative angles. For the in phase combination of TE_{01} and TM_{01} beams, the relative angle between two HWP at +45° gives the pure azimuthally polarized TE_{01} beam and for a -45° it is converted into radially polarized TM_{01} beam. The corresponding two lobe patterns after the analyzer are as shown in Fig.2.11 (b). For the combination of even and odd HE_{21} modes the relative angle between the two HWP at +45° gives radially polarized TM_{01} beam and for -45° azimuthally polarized TE_{01} beam. The corresponding behaviors for the analyzer rotation are shown in Fig.2.11 (b).

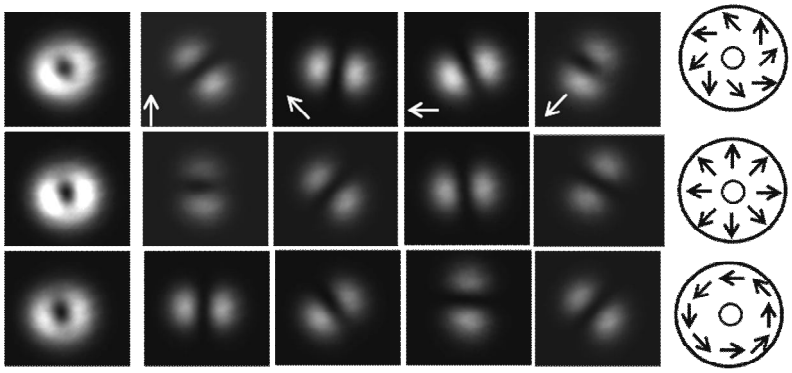

Figure 2.11: (a) First row, direct fiber output of in phase TE_{01} and TM_{01} mode second and third rows are the beams after passing through the HWP with respective angles at +45° and -45° (b) output beam for different analyzer rotations (c) Corresponding electric field vector orientation.

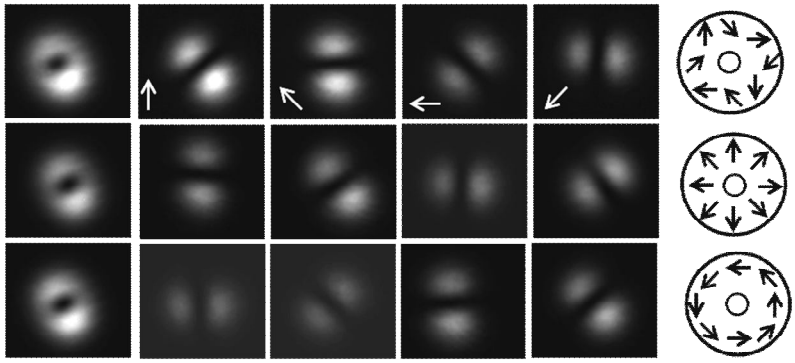

Figure 2.12: (a) First row, direct fiber output of in phase HE_{21} even and odd mode second and third rows are the beams after passing through the HWP with respective angles at -45° and +45° (b) output beam for different analyzer rotations (c) Corresponding electric field vector orientation.

2.5 Effect of other parameters on vector-vortex beam generation

In addition to the input beam polarization and the launching angle the generation of vector-vortex beams also depends on the fiber length and numerical aperture (NA) of the lens. Based on our experimental observations we qualitatively address these effects.

2.5.1 Length of the fiber

The vector fiber modes are length dependent due to the polarization correction term to the scalar propagation constants which plays a crucial role in the generation optical VV beams. The 'β'values of the vector modes calculated using eqn. (1.28), are used to select the appropriate length of the fiber for the desired mode generation. The on axis launch of externally generated HG or the LG beam into the fiber, in which the input and output beams with same orientation and polarization is possible only at a particular length of the fiber where the beat length interms of the fiber eigen modes is equal to the fiber length. In these experiments the desired modes are obtained by cutting the fiber to appropriate lengths. In coupling the Gaussian beam into the fiber as off-axis skew beam, to within the first few millimeters of the fiber length the input Gaussian beam is converted into the fiber modes. After this length, the modes propagate in the fiber the same way as the coupling of the externally generated HG or the LG beams. The length dependence of the fiber modes in this case can be studied by fixing one input condition and cutting the fiber output end to get back to the starting mode or by tuning the input wavelength of the Gaussian beam (which effects the 'β'values of the modes) for a fixed fiber length and input conditions. Using second method we studied the propagation of modes in the fiber interms of the evolution of polarization singularities in Chapter 3.

2.5.2 Numerical aperture of the lens

The NA of the input lens effects the cone of light coupled into the fiber. For an on axis launching (Fig.2.1 (b)) the NA of the lens which is close to the fiber NA will couple maximum light into the guided modes. In our experiments the effect of NA on the mode excitation is carried out for three different NAs. Since the

NA of the fiber used in this thesis is 0.20, the three different NAs used here are 0.10, 0.25, and 0.40 above and below the fiber NA. The diameter of the focused spot for the three different NAs are calculated using formula $w = \frac{4\lambda f}{\pi D}$, where λ is the wavelength (632.8 nm), 'f' focal length of the lens (25.4mm, 16.5mm and 9.0mm) and 'D' the beam diameter incident on the lens (2.5mm). The measured diameters of the focused spot for the three different NAs are: 8.1μm, 5.3μm and 2.8μm respectively with reference to the core diameter of the fiber 3.8 μm.

The effect of NA on the output beam is understood by adjusting input conditions for the same output beam for three different NAs by adjusting the x and y positions of the fiber for the same input polarization. For the input HWP at 0° the output beams for the three different NAs are as shown in Fig.2.13 (b). The intensity difference between the two lobes is more for the input NAs of 0.10 and 0.25 whereas for 0.45 the variation is small. This is probably due to the different spot sizes due to the lens: bigger spot sizes exciting more fundamental mode than the smaller spot sizes along with the vector modes and the beating between these modes results to the intensity variation between the two lobes [23]. By changing the input polarization for the same input launch conditions, to HWP at 67.5° the output beams for all the three NAs are shown in Fig.2.13 (c).

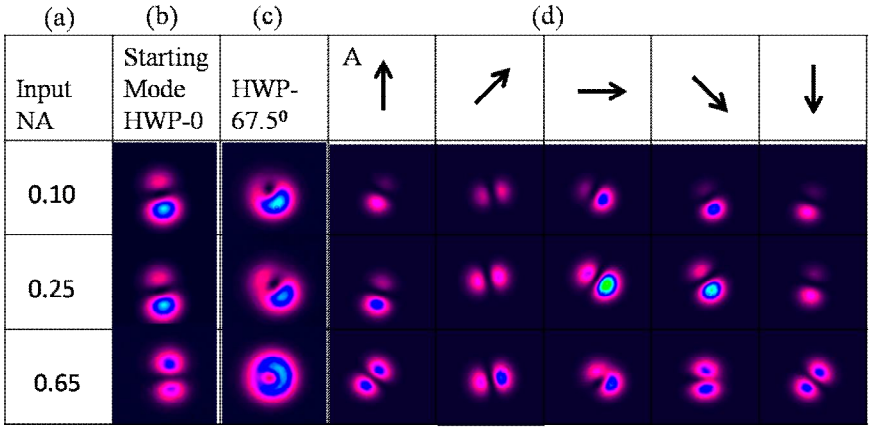

Figure 2.13: (a) Different NA of the objective lens used to couple light into the TMF (b) Starting modes for different NAs,. (c) Output mode for the input HWP at 67.5° (d) Output beams for different NAs analyzer orientation.

For the output beams passing through the clockwise rotating analyzer, the two lobe pattern rotates in the same way for all the three NAs shown in Fig.2.13 (d). From the analyzer rotation the behavior of the output beam is a combination of out of phase TE_{01} and TM_{01} modes. The intensity distribution across the beam cross section is different for the three different NAs and is also reflected in the analyzer data as the intensity variation in the two lobes. The intensity variation in the two lobes after the analyzer is more for the 0.10 and small for the 0.45 NA. This behavior is strongly connected with our starting mode which has different intensities in the two lobes. The lens with higher NA than the fiber has the advantage in order to suppressing the effect of fundamental mode in the output beam.

2.6 Summary

In this chapter, we presented our results on the vector-vortex beams generated using short length of two-mode step-index fiber by coupling Gaussian beam as off-set skew beam. The positive and negative cone angle of the input beam with respect to the fiber axis excite different mode combinations and opposite helical charges. For the output beam passing through the rotating analyzer the polarization content of the output beams are shown as linear vectors are as approximation to elliptically polarized output as will be shown using Stokes polarization measurements. Analyzer rotation alone can not give the complete information about the polarization of electric vectors across the beam cross section for which we need some other techniques to measure the state of polarization across the beam at every point. In the next chapter we present Stokes parameter techniques to measure the presence of partial vortices and the state of polarization at every point in the beam to better understand the beams generated from the TMF under different conditions.

Chapter 3

Polarization Singularities in Vector-vortex beams

In this chapter, we introduce polarization singularities (L-line and C-point) in paraxial waves and different techniques such as interferometric and complex Stokes parameter methods to identify the presence of partial vortices and polarization singularities in the output beam. In our experiment, the polarization singularities in the output beams for a fixed input condition are studied using a tunable wavelength (700-1000 nm) continuous-wave Ti: Sapphire laser. The input wavelength is tuned in the range of 740-760 nm, insteps of 1nm for two different output (HG_{10} and LG_{01}) beams for fixed input conditions. Within this wavelength range the output beam evolves from one elliptically polarized region to another through polarization singularities. The polarization behavior of the output beams are characterized by constructing state of polarization map using complex Stokes parameter method. The presence of L-line, C-point and the orientation of polarization ellipses around the C-point are also characterized using the complex Stokes parameter method. The formation of two C-points with same topological charge in the output beam is analyzed by the mutual influence of the two partial vortices and confirmed by the sign rule. The intensity plot and the polarization plot on the Poincare sphere for all the output beams confirms the cyclic behavior of the polarization singularities as a function of input wavelength.

3.1 Introduction

In the paraxial wave approximation, the transverse component of electric field vector, $\mathbf{E}_t$, describes a polarization ellipse. The polarization ellipse is defined by ellipse parameters such as size (a, b), shape (b/a) and orientation angle (φ) [35]. In a scalar beam the polarization ellipse parameters are same at all spatial points in the transverse plane but in vector field the polarization ellipse parameters vary spatially from point to point which results in complicated polarization patterns. The most obvious features of these complicated patterns are the generic (stationary stable) polarization singularities [2-7]. In the paraxial wave approximation the spatial distribution of polarization ellipse maintains two kinds of polarization singularities: L-surfaces (or S-surfaces) and C-lines, which in a 2-D observation plane become L-line (or S-line) and C-point [2-7, 80]. The L-line is where the field is linearly polarized and the handedness of electric vector rotation is indeterminate (singular) and the C-point is where the field is circularly polarized and as a consequence the polarization azimuth and the vibration phase (S_C) are indeterminate [2-7]. The C-points are characterized by the polarization index I_C that describes the orientation of the ellipsis axis in the surrounding vector field and the topological charge of the vibration phase S_C [2]. The sign of the vibration phase S_C of the C-point coincides with the sign of the topological charge of the vortex beam in which it is formed [81, 82]. The polarization index I_C is defined as $I_C = \frac{1}{2\pi}\oint d\alpha$, where α is the orientation angle of the polarization ellipse around the C-point. This index takes values of $\pm 1/2$ when the integration is carried out on a loop drawn around the C-point. The sign of the C-point (I_C), the sign of the handedness of the polarization (h)

in which the C-point is embedded and the sign of the vibration phase S_C are related by $I_C = hS_C$ [81, 82]. From this relation, by knowing the sign of any two quantities we can find the sign of the third quantity.

The C-point singularities are classified by three different properties: namely index, line and contour. The index is identified by the orientation of polarization ellipse major axis around the C-point: clockwise direction index is +1/2 and is -1/2 for an anti-clock wise rotation [2]. The line property is identified by the number of straight line trajectories that emerge (terminate) from (on) the C-point. The number of lines that terminate on a singularity is generically 3 or 1. For the -1/2 index the number of lines that terminate on the singularity is always 3 and such a singularity is called 'Star' whereas for the +1/2 index, the number of lines that terminate on the singularity is either 1 or 3, and the corresponding morphologies are Lemon and Monstar respectively. A pictorial representation of all the three patterns are shown in Fig.3.1 (a-c) [2, 6].

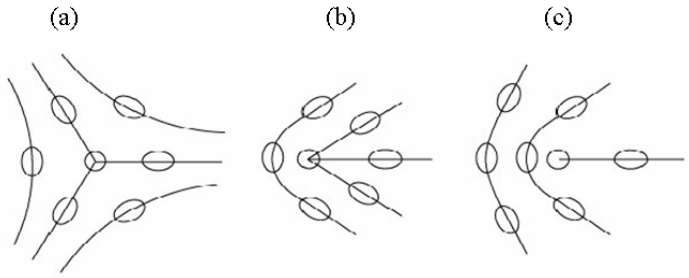

Figure 3.1: The polarization patterns around the C-point with three types of point singularity in a 2-D field (a) Star (b) Monstar and (c) Lemon (adapted from [2]).

The third property, contour is different from the other two in that it refers to the shape of the lines around the C-point, which is positive for ellipse and negative for hyperbola. Based on these classifications, six different C-point singularities

are possible and with each one a right or left handed polarization resulting in a total of twelve possibilities in all [4, 7].

3.2 Measurement and characterization of polarization singularities

In a scalar field, the condition for singularity, $\mathrm{Re}\,\mathrm{E} = \mathrm{Im}\,\mathrm{E} = 0$, represents two surfaces. The intersection of these two surfaces results in a generic dislocation (phase singularity) which forms a line in three dimensions or a point in a 2-D observation plane [1, 5]. These singularities are observed in the interference with a plane wave resulting in a forklet depending on the topological charge of the vortex beam and the angle of the interfering beam with respect to the singular beam [27, 77, 83-85]. In vector singularities, the component $\mathbf{E}_x$ has two surfaces, and the component $\mathbf{E}_y$ also has two surfaces,. The $\mathbf{E}_x$-component of the field has a generic dislocation line where the two surfaces ($\mathrm{Re}\,\mathbf{E}_x = \mathrm{Im}\,\mathbf{E}_x = 0$) meet to form a phase singularity and similarly for the $\mathbf{E}_y$-component. But the dislocation of the generic lines of the $\mathbf{E}_x$ component will not intersect with the $\mathbf{E}_y$ component lines as it requires an intersection of all the four surfaces at all the time. There will be no points in space where $\mathbf{E}_t$ is zero at all the time [2]. Hence, the polarization singularities are not the amplitude zero singularities as in scalar field singularities because all components of the transverse vector field $\mathbf{E}_t$ are not zero simultaneously at all the time. Measurement and characterization of the polarization singularities are typically carried out either using an interferometric method [82, 86-88] or complex Stokes parameter method [89-91].

3.2.1. Interferometric method

In this method, the vector singularities in the beam cross-section are measured by adapting the scalar forklet method [27, 77]. For finding a set of L-points, the inhomogeneously polarized vector-vortex beam and the unpolarized plane wave reference beam pass through the rotating analyzer to form an interference forklet pattern. The analyzer selects the field components from the vector-vortex and reference beams depending on the orientation of the analyzer axis and blocks the orthogonal component. Analyzer oriented at 0° allows only one component of the field, $\mathbf{E}_x = 0; \mathbf{E}_y \neq 0$, which forms a generic dislocation in the $\mathbf{E}_x$ component of the field. Similarly, for the analyzer oriented at $90°, \mathbf{E}_x \neq 0; \mathbf{E}_y = 0$, which forms a generic dislocation in the $\mathbf{E}_y$ component. Rotation of the analyzer from 0° to 180° and finding the positions of all forklet patterns gives the set of all L-points in a vector field and the joining of all such points gives the L-line [82, 86-88]. For finding the C-point in the beam cross-section an additional quarter wave plate (QWP) is inserted before the rotating analyzer [86]. The QWP transforms the elliptically polarized field into linearly polarized along some line, where the direction of the polarization ellipse axis coincides with the fast axis of the inserted QWP. As a consequence, other L-lines are formed after the QWP and these lines are identified as azimuth or a-lines. It is clear that the rotation of QWP will give infinite family of such a-lines and the majority of them cross both the L-line and C-point inside it. The intersection point of all such a-lines will give the C-point [86-88].The a-lines possess $\pi/2$ jump while crossing the C-point, which resembles the behavior of equiphase lines, which undergo a π jump while crossing the phase singular point [2, 86]. The topological charge of the C-point or its polarization index I_C

are measured from the azimuth lines by taking the rotation of polarization ellipse around the C-point, if they rotate same way as the path tracing direction, I_C is +1/2 and for opposite direction of rotation, I_C = -1/2.

3.2.2 Complex Stokes parameter method

The polarization state of an optical field is usually characterized by the four Stokes parameters (S_0, S_1, S_2, S_3). The Stokes parameters are defined as follows [92]:

$$\begin{aligned} S_0 &= E_x^2 + E_y^2 = I(0,0) + I(90,0) \\ S_1 &= E_x^2 - E_y^2 = I(0,0) - I(90,0) \\ S_2 &= E_x E_y^* - E_x^* E_y = I(45,0) - I(135,0) \\ S_3 &= -i(E_x^* E_y - E_x E_y^*) = I(45,90) - I(135,90) \end{aligned} \tag{3.1}$$

The Stokes parameters are calculated from six intensity measurements as given in eqn. (3.1) where, $I(\theta,\phi)$ is the intensity passed by a polarizer oriented at an angle θ to the positive *x*-axis and ϕ is the phase introduced by $\lambda/4$ plate to the *y* component before passing through the polarizer [92]. For the fields of interest, the Stokes parameters are not independent but obey the relation $S_0^2 = S_1^2 + S_2^2 + S_3^2$ for a completely polarized field. If the sum of the three Stokes parameters adds up to less than S_0^2 i.e., $S_0^2 > S_1^2 + S_2^2 + S_3^2$, the beam is considered as partially polarized. The Stokes parameters can be normalized to give the normalized Stokes parameters, which are defined as [92]:

$$s_i = \frac{S_i}{\sqrt{S_1^2 + S_2^2 + S_3^2}} = \frac{S_i}{pS_0}; i = 1, 2, 3 \tag{4.5}$$

where $p = \sqrt{S_1^2 + S_2^2 + S_3^2}/S_0$ is the degree of polarization. The Stokes parameters are related to the polarization ellipse parameters as: orientation angle $\tan 2\alpha = \frac{s_2}{s_1}$ and the ellipticity $\sin 2\chi = \frac{s_3}{s_0}$. From these relations the polarization singularities are measured from the complex Stokes parameters [89-91]. If $\chi > 0$, the polarization ellipse is right handed and is left handed for $\chi < 0$. The points where $\chi = 0$, the state of polarization is linear. For L-line where the polarization is linear, it is measured by making the complex Stokes parameter $s_3 = 0$. The C-point, being a point of circular polarization where the vibration phase and orientation angle are undefined are characterized by making the Stokes parameters $s_1 = s_2 = 0; s_3 = 1$, also known as Stokes vortex [91]. The orientation of the ellipse around the C-point or the sign of the topological charge of the C-point (I_C) is determined using the relation $2\alpha = \arg(s_1 + is_2)$. For the clockwise rotation of the ellipse around the C-point, the topological sign of the C-point is +1/2 and is -1/2 for counter clockwise direction.

3.3 Wavelength dependence of polarization singularities

The wavelength dependence of PSs generated using the two-mode optical fiber depends on its dispersion characteristics. In general, fibers have two different kinds of modal dispersions, intermodal and intramodal. The intermodal dispersion is due to the propagation of different transverse modes whereas intramodal dispersion is due to the waveguide dispersion and material dispersion [93-95]. The waveguide dispersion is due to the confinement of modes in a

waveguide with propagation constant 'β', which is wavelength dependent, resulting in different speeds for different wavelengths. The material dispersion is due to the wavelength dependence of refractive indices of the core and cladding. Birefringence in fibers is due to the deformation of circular core, transverse stress and elastic twist, which causes modal dispersion, and changes the input state of polarization [96]. The residual linear birefringence of a fiber due to the deformation of circular core and transverse stress is measured by the evolution of fixed linearly polarized input, either by cut-back technique or wavelength scanning method [97, 98].The measured wavelength dependence of the output polarization state can be traced along a trajectory on the Poincare sphere [99, 100].

In a step-index fiber the birefringence characteristics are observed as a difference in the polarization corrections δβ to the scalar propagation constant β of the azimuthally symmetric linearly polarized OV (LV) mode or circularly-polarized (CP) modes [101]. The intermodal dispersion due to the difference in the propagation constants of the fiber modes and their polarization correction leads to vector inhomogeneity in the output field from the fiber [26, 101]. We measured the wavelength dependence of the vector inhomogeneity and hence the polarization singularities by using a tunable laser, whose wavelength is in the two-mode region of the fiber.

3.4 Experimental details

Schematic of the experimental setup used for generating polarization singularities of vector fiber modes and for demonstrating its wavelength dependence is shown in Fig.3.2. A tunable continuous-wave (CW) Ti: Sapphire laser (MBR 110, Coherent, USA) is used as the light source. The overall

wavelength range of operation of the laser is 700 nm -1000 nm and the range of interest to us here is 740 – 760 nm, which is in the middle of the two-mode regime (2.4048<V<3.8317) of the fiber. The laser output is a linearly polarized (500:1) TEM_{00} beam. A 4 % reflection from the glass plate is taken and coupled to an optical spectrum analyzer (AQ 6370B, Yokogawa, Japan) to monitor the wavelength of the light. A Glan-Thomson polarizer (P) (> 10^5:1) and a half-wave plate (HWP) are used to control the polarization of the input beam launched into the fiber thereby controlling the output beam characteristics. A modified Mach-Zender interferometer is constructed in parallel to measure the phase characteristics of the generated beam. A beam splitter (R/T ≈ 50/50) is used to split the incoming light beam into two beams of almost equal intensity. The beam passing through the beam splitter (BS_1) is focused using a microscope objective lens L_1 (0.20 NA and 10X) to couple the laser light into the fiber, whose input end is fixed on a 3-axis precision launching mount. The output from the fiber is collimated using another objective lens L_2 (0.40 NA and 20X) as shown in the Fig.3.2.

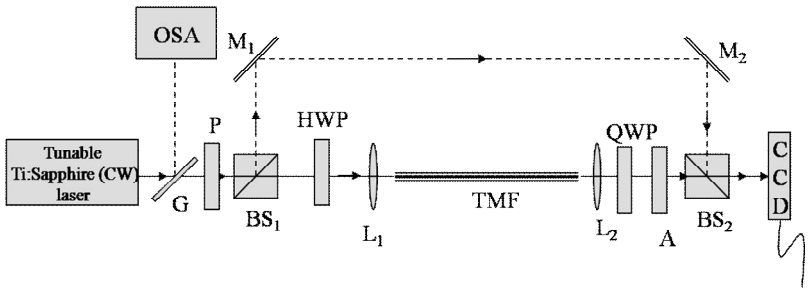

Figure 3.2: Schematic of the experimental setup used to demonstrate wavelength dependence of the polarization singular beams generated using a two-mode optical fiber (TMF). G: Glass Plate; P: Glan-Thomson polarizer; OSA: optical spectrum analyzer; HWP: half wave plate; BS: beam-splitter; M: mirrors L: microscopic objective lens; QWP: quarter-wave Plate; A: analyzer; CCD-charge coupled device.

The reference beam that is reflected from the BS_1 after reflection at mirror M_1 and M_2, is made to interfere collinearly with the output beam from the fiber using the beam splitter (BS_2). A CCD camera connected to computer via IEEE 1394 card is used to capture the images of the output beam directly from the fiber and the interferometer output. We first generate the desired HG or LG beam at a given wavelength by adjusting the launch conditions and carry out the required interference and Stokes parameter measurements on the beam. The measurements are repeated for different uniformly spaced wavelengths of the input beam. The desired output beam from the fiber is generated by adjusting the controls – HWP orientation angle, and the launching conditions at a given wavelength of the input beam and for a fixed fiber length, as discussed in Chapter 2.

3.5 Results and discussion

For the input wavelength of the Ti: Sapphire laser tuned to λ_1 = 740nm and the HWP oriented at 0°, the linear vertically polarized Gaussian beam is coupled into the cleaved input end of the TMF. By placing, the fiber at the focal point of the objective lens L_1 and adjusting the 'x' and 'y' positions of the fiber we launch the beam as offset skew beam into the fiber. The output two-lobe intensity pattern is similar to the HG_{10} beam, without changing the input launch conditions HWP is rotated to 45°, and the output is a LG_{01} beam. The two output modes and their corresponding edge and fork interference patterns are shown in Fig.3.3.

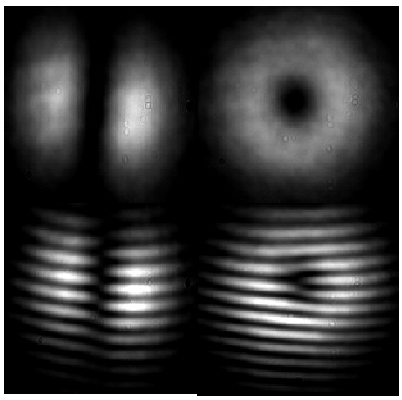

Figure 3.3: Output modes for two different orientations of the input HWP (0° and 45°) and the corresponding interference (edge and fork) patterns.

In this experiment, the polarization singularities are measured using the complex Stokes parameter method. The six intensity measurements of both the output beams are measured as I(0; 0), I(π/2; 0), I(π/4; 0) and I(3π/4; 0) which are measured by orienting the analyzer (A) at 0°,90°,45° and 135° angles without the QWP in the output beam and as I(π/4; π/2) and I(3π/4; π/2) measured by introducing the QWP before the analyzer (A), with its fast axis oriented at 90°, and recording the intensities for the analyzer angles 45° and 135° respectively. The six intensity measurements for the output HG_{10} and LG_{01} beams are shown in Fig.3.4.

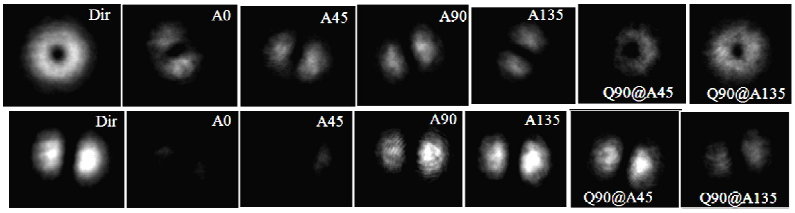

Figure 3.4: All the six Stokes intensity measurements of the fiber output HG_{10} and LG_{01} beams respectively. Dir: direct beam, A: analyzer, Q: quarter wave plate

From the above figure (Fig.3.4) it is seen that the HG_{10} beam has more RCP component than LCP component, so that the polarization state of the output beam is predominantly right elliptically polarized along the x-direction. For the LG_{01} beam, for the analyzer oriented at 0° we get two lobe inclined pattern after the analyzer which rotates the same way as the analyzer, implying that the beam is a combination of TE_{01} and TM_{01} modes. The same beam after passing through the QWP - analyzer combination shows the presence of two partial vortices. The LCP vortex intensity is more than the RCP vortex, implying that the output beam is predominantly left elliptically polarized the orientation of ellipse across the beam cross section changes. The topological charges of these partial vortices are measured by changing the reference beam polarization that will selectively interfere with the corresponding polarization vortex or by interfering the beam after the QWP and analyzer combination [24, 53, 102]. In this case, the change of reference beam polarization results in up and down forklet for the two partial vortices, indicating that they have opposite topological charges. The two vortices and their topological charges are: right circularly polarized vortex with -1 topological charge i.e. (1 -1), and left circularly polarized vortex with +1 topological charge i.e. (-1 1).

From the six intensity images measured using the CCD, the Stokes parameters are obtained for each pixel using the intensity value at the same coordinates from the images. This is done using a MATLAB code written for this purpose, which loads the grayscale bitmap images from the CCD as matrices and processes them.. Using this method the four Stokes parameters are obtained for each pixel in the image. The important point is that the images used in the Stokes parameter calculation are to be captured with the CCD in the same position, and care must be taken that the output QWP does not cause any

shift in the beam when introduced in its path. The four Stokes parameters of the two output beams are shown in Fig.3.5 (a, b) in a custom scale to highlight the contributions of the different polarizations to the overall beam.

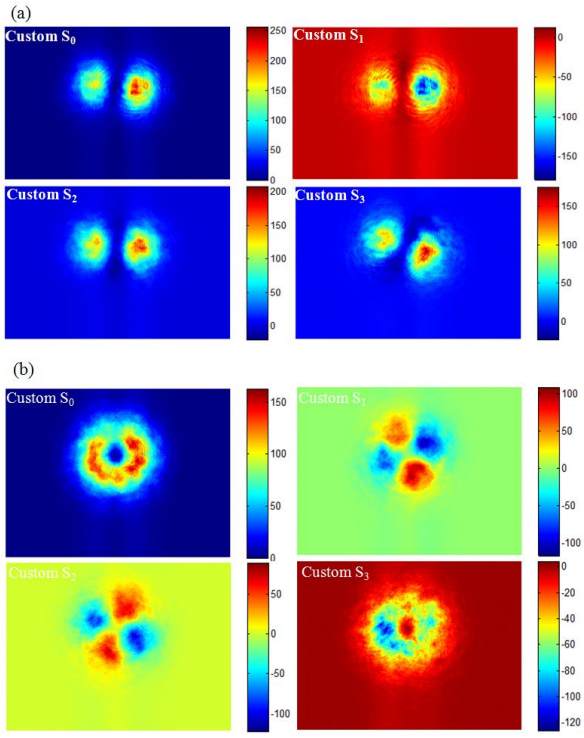

Figure 3.5: Point wise Stokes parameter of the output (a) HG_{10} and (b) LG_{01} beams from the TMF.

Further, from the Stokes parameter measurements we also calculated the state of polarization (SOP) of the output modes using the ellipse parameters calculated at every point within the beam and using the parametric form of polarization ellipse [92]. The polarization map of the light beam can be plotted which will give the SOP at every point in the beam cross section. As plotting the polarization ellipse at each pixel will make the polarization map crowded

and we cannot get any insightful information about the state of polarization, we take plain average of all the elements in a square block of suitable dimension so that this block tiles the entire image exactly and take the average as the representative value of that block. Essentially, we reduce the size of the matrix to a manageable size to represent the SOP in the beam cross section effectively.

The ellipse parameters are calculated at each point in this resized image, and the polarization ellipse is plotted in the expanded image of the same size as the original image and to fit the square block exactly. The SOP map of the two output beams are shown in Fig.3.6 (a, b). From Figs.3.5 (a, b) the HG_{10} beam is a right elliptically polarized with a small left elliptical region, whereas the overall $LG_{01,}$beam is left elliptically polarized even though it has right circular vortex. This RCP vortex is not visible in Fig.3.6 (b), due to the large intensity difference between the two vortices as discussed above and also due to the pixel average which we have taken to construct the polarization ellipses (256-pixel average).

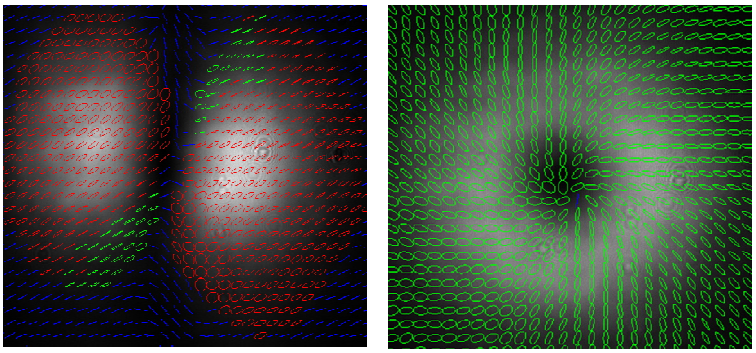

Figure 3.6: State of polarization (SOP) map superimposed on the original images of the (a) HG_{10} and (b) LG_{01} output beams. Red: right-handed ellipses and Green: left-handed ellipses.

The vector singularities in the output beam are measured as discussed in Sec 3.2.2. The L-line where the state of polarization is linear is measured by making the Stokes parameter $s_3 = 0$, is shown in Fig.3.7 (a, b) as a dark line. The C-point where the polarization is circular is measured by making the Stokes parameters $s_1 = s_2 = 0$ (not shown here) and the same information with the sign of topological charge of the C-point is measured from $\alpha = \frac{1}{2}\arg(s_1 + is_2)$. The orientation angle of the ellipses around the C-point is shown in Fig.3.7 (a, b) (hue plot) for the two output beams.

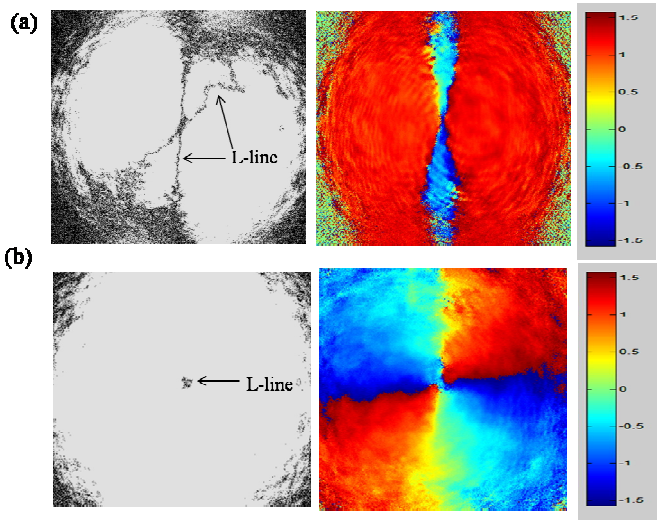

Figure 3.7: (a, b) The L-line and the hue plots of polarization ellipse orientation around the C-point for the two output (HG_{10} and LG_{01}) beams. In (b) the ellipses rotate in clockwise direction, index I_C is +1/2.

From Fig.3.7 (a) for the HG_{10}beam there are no C-points as such because the polarization structure does not complete a full circle whereas for an LG_{01} beam (Fig.3.7 (b)) shows two C-points with same index sign. The formation of C-points can be understood interms of the coherent superposition of two

orthogonal circularly polarized vortex (partial vortices) modes. In this case the presence of two partial vortices (1 -1) and (-1 1) are perturbed by each other to satisfy the condition to form a C-point with the condition that the two vortices should be orthogonally polarized [2] (more in Chapter 4). The formation and the topological sign of the two C-points are as follows, when the RCP ($\sigma=1$) vortex mode with topological charge -1 is perturbed by the LCP ($\sigma=-1$) vortex mode with topological charge +1. At the core of the RCP vortex the field is a perturbed left circular polarization (σ = -1), where the C-point is located. From the sign of the topological charge of the RCP vortex mode we can find the sign of the vibration phase (S_c) as discussed above. In this case the sign of the vibration phase is negative ($S_C=-1$), hence, from the sign rule the topological charge of the C-point is positive ($I_C=+1/2$) because the product of both handedness in which the C-point is located and the vibration phase are negative. Similarly, for the (-1 1) vortex perturbed by (1 -1) vortex, the sign of the handedness and the sign of vibration phase of C-point are interchanged so that the sign of the C-point is positive ($I_C=+1/2$). Therefore, in both the cases the sign of the C-point is positive as indicated clearly in the hue plot (Fig.3.6 (b)).

For the HG_{10} mode, across the beam cross-section different polarization regions are present and the left and right elliptical regions are separated by the L-line. This behavior is due to the presence of disclination in the beam cross-section due to the combination of different vector modes as discussed in Sec 1.4 and 1.5 [26]. In other words, the intramodal phase difference accumulated by the propagating modes due to the fiber birefringence and the weight factor of the modes are superposed to generate the output beam. These are governed by the overall residual linear birefringence of the fiber, which includes

inhomogeneities in the core shape, doping inhomogeneities which in turn give rise to non-uniform refractive index profile along the propagation direction. However, in a step-index fiber these disclinations evolve along the fiber length. Due to the birefringence or the polarization correction terms to the vector modes, the evolution can be understood by cutting the fiber length or by tuning the input wavelength.

To investigate further, without changing the input launch conditions we tune the laser wavelength in steps of 1 nm from λ_i = 740nm to λ_f = 760 nm and at each wavelength the input HWP is oriented at two different positions (0° and 45°) as mentioned above. As the wavelength of the input laser is increased, part of the beam that was left elliptically polarized gradually increases in size in the HG_{10} beam whereas in the LG_{01} beam the right elliptically polarized region gradually increases in size. From λ = 740 nm to 758 nm the above mentioned change from REP to LEP over the entire beam is completed for the HG_{10} beam whereas for the LG_{01} beam the LEP to REP is only half transformed. The change in the handedness of the two output beams is due to the wavelength dependent material dispersion of the fiber, which affects the polarization correction terms of the propagation constants for different input wavelengths.

For all the output beams, we measured the SOP, the L-lines and the polarization orientation angles: the L-lines (L_x and L_y) and the orientation angle using $s_3 = 0$ and $\alpha = \frac{1}{2}\arg(s_1 + is_2)$. The SOP map and the polarization singularities are shown in Figs.3.8 (a, b) and 3.9(a, b) for three different input wavelengths of 740, 748 and 758 nm respectively. From these figures, for HG_{10} beam by tuning the input wavelength the L-lines change their positions and at the λ = 758 nm the L_x and L_y disclinations are collinear to form a pure edge elli-

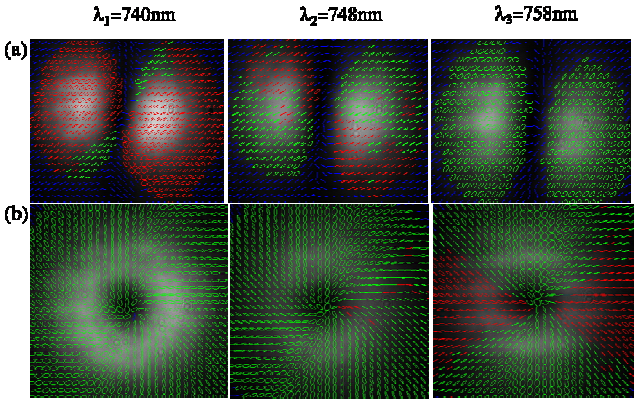

Figure 3.8: Evolution of the polarization ellipse in the output (a) HG_{10} beam (b) LG_{01} beam as a function of the input wavelength.

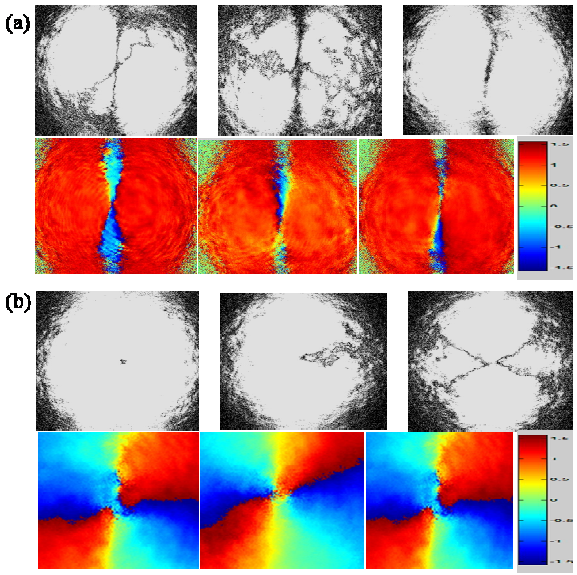

Figure 3.9: (a, b) The L-line and polarization ellipse orientation maps of the output of HG_{10} and LG_{01} beams at different wavelengths as mentioned in Fig.3.8

-ptical dislocation. Whereas for LG_{01} beam half LEP and half REP are formed due to the intensity variation in the two partial vortices with respect to input wavelength tuning and the boundary between them are separated by L-line. In

this case, the presence of two C-points are as shown in Fig.3.9 (b). Now moving beyond, at λ = 760 nm we see parts of the beam that are LEP begin to turn around to being REP for the HG_{01} beam. This confirms that the change in the polarization content (or change in the handedness) of the output beam is periodic for input wavelength tuning. Simultaneously, we also observed that the intensities of the output beams changes periodically for the input wavelength tuning.

Further analysis is carried out on the intensity patterns of the two output modes for all the wavelengths. In addition to plotting the polarization ellipse in the beam cross section, we also plot the change in the output beam intensity along a fixed line across the beam: x-direction for the HG_{10} beam and x and y-directions for the LG_{01} beam for all the wavelengths as shown in Figs.3.10 and 3.11 respectively. It is important to note here that the line profile for the output beams from the fiber at the starting wavelength (λ_i) has a slight asymmetry in its peak intensity, possibly due to the fiber V-clamp in the output and a slight bend in the fiber along its length, which causes slight asymmetry in the output intensity pattern. A plot of the line profile of the output beam as a function of wavelength emphasizes that the beam intensity variation is periodic with wavelength (inset in Fig.3.10), for both the outputs due to the dispersion of the polarization correction of the vector modes contributing to the output beam from the weakly birefringent elliptic distorted TMF. Also, as the fiber vector modes are excited by offset and skew linearly polarized Gaussian beam that travels along a twisted path inside the fiber, the role of transverse energy flow in the field results in the rotation of the instantaneous energy distribution with wavelength which cannot be ruled out [43]. In addition, the small modulation contrast (~ 100 and ~ 20counts) in the two-lobe intensity and in the LG_{01} beam

due to wavelength scanning further emphasizes that the dispersion in the polarization correction terms is of consequence here rather than the HE_{11} mode influence [103]. Thus, it is clear from our observations that both the handedness of the polarization ellipse and the intensity of the output beam changes periodically with the wavelength of the input beam [104].

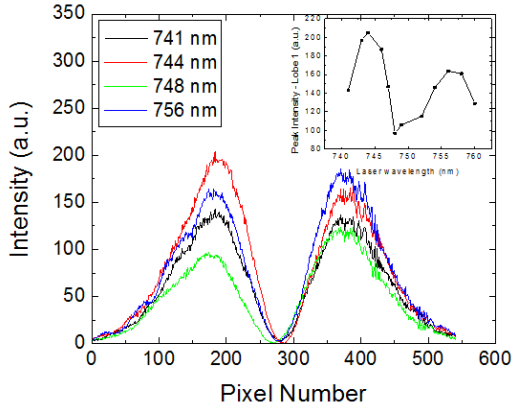

Figure 3.10: Line intensity plot of the output HG_{10} beam as a function of the input wavelength. Inset shows the periodic behavior of the peak intensity of the left lobe as a function of the laser wavelength.

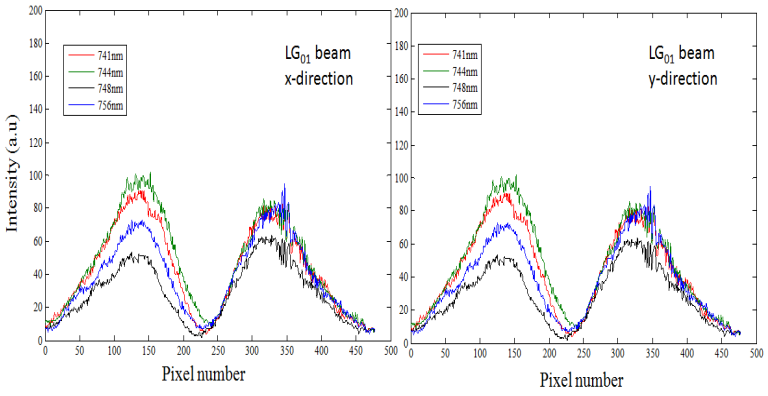

Figure 3.11: Line intensity plot of the output LG_{01} beam as a function of the input wavelength in the x and y directions.

It is known that graphic representation of the polarization data allows a clear insight into the complex situation where the SOP evolution is tracked as a function of the wavelength. Based on the Stokes parameters calculated for the different input wavelengths we extract the necessary information to plot the evolution on the Poincare sphere representation for both the HG and LG output beams. For the HG_{10} beam, we pick the two polarization points along the x-direction from the two lobes whereas for the LG_{01} beam the two points are picked from the x and y directions of the beam, and the corresponding polarization states on the Poincare sphere are shown in Figs 3.12 and 3.13 [35]. The two points in the right and left lobes of the HG_{10} beam shows the same behavior for the input wavelength scanning (Fig.3.12), whereas for the LG_{01} beam, the x and y polarization points in Fig.3.13 (red and black lines), shows different behavior, because as the wavelength scanned along the x-direction while the polarization changes from LEP to REP whereas in y-direction it still in the LEP state for the LG_{01} beam (Fig.3.8 (b)).

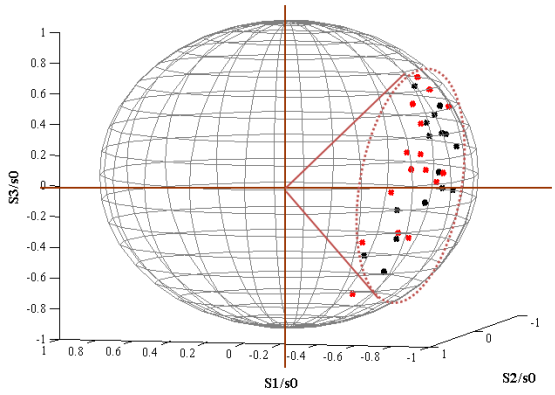

Figure 3.12: (a) Poincare representation of the Stokes parameters measured in the TMF output as a function of the input laser wavelength. The two sets of data are for the right and left lobes of the output beam.

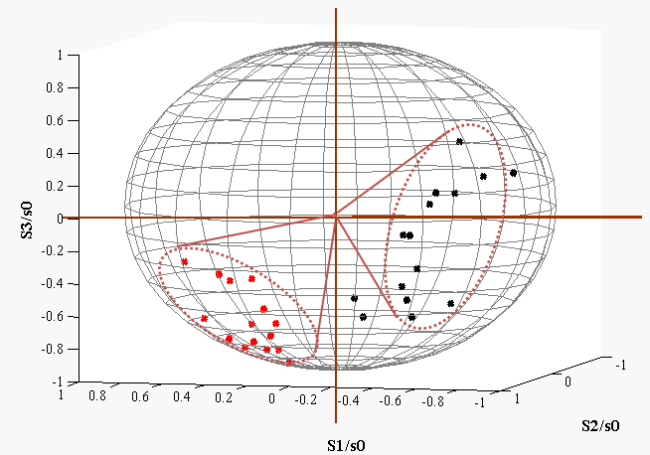

Figure 3.13: (a) Poincare representation of the Stokes parameters measured in the TMF output as a function of the input laser wavelength. The two sets of data are for the x and y-direction of the beam, black and red colors respectively

For the fixed input linear polarization, scanning the input wavelength from 740 nm to 760 nm at a fixed point on the output beam the SOP moves on the Poincare sphere from REP to LEP for HG_{10} beam whereas for the LG_{01} beam it changes from LEP to REP. As our wavelength scan range covers only a phase change of $\pi/2$ between the superposed vector modes, we have plotted only one half of the curve. However, proceeding with the increasing wavelength, we expect to cover the second half of the trajectory as well, which should correspond to the evolution of elliptically polarized light on the Poincare sphere.

3.6 Summary

The experimental demonstration of the generation of polarization singular optical beams due to superposition of vector fiber modes and their wavelength dependence emphasize the role of modal dispersion in the characteristics of the beams. The evolution of right elliptically polarized edge dislocation to pure left elliptically polarized edge dislocation through disclinations for the two lobe HG beam and the pure left elliptically polarized LG to half right and half left elliptically polarized LG beam are achieved by tuning the input laser wavelength from 740 nm to 760 nm in steps of 1nm. The changes in the polarization characteristics of these beams with the change in the laser wavelength occur due to the dispersion of the propagation constant (β_i) and the polarization correction $(\delta\beta_i)$ of the vector modes as they propagate in the fiber. Some evidence is also shown to emphasize that these changes, in addition to the intensity variations and the polarization ellipse parameters are cyclic with wavelength of the input beam. The presence of the two partial vortices in the output LG beam results in the formation of two C-points with same topological charges. We anticipate that the results will be useful in the advancement and the applicability of the polarization singular beams, especially in polarization tweezers.

Chapter 4

Generation and Characterization of Isolated Polarization Singularities

In this chapter, we introduce the mathematical background of formation of isolated polarization singularities (IPSs) due to the coherent superposition of orthogonal circularly polarized fundamental and vortex modes, and our experimental results on the generation of isolated polarization singularities. Comparison between the two different measurement techniques of identifying IPSs as introduced in Chapter-3 and the switching between the different topological charges of the C-point ($\pm 1/2$) are also presented. The switching between the different C-point topologies is achieved in two different ways: (i) by changing the input launch position with respect to the fiber axes to a diametrically opposite position in the fiber cross-section (I_1 and I_2) and (ii) by switching the handedness of input polarization from right circular to left circular or vice versa as mentioned in Chapter 2.

4.1 Introduction

Consider a right circularly polarized (RCP) vortex beam in free space, the electric field components of the vortex beam are written as

$$\begin{aligned}\mathbf{E}_x &= (kx + iky)\,\mathrm{expi}(kz - \omega t)\\ \mathbf{E}_y &= -i(kx + iky)\,\mathrm{expi}(kz - \omega t)\end{aligned} \tag{4.1}$$

Where, $k=2\pi/\lambda$ is the propagation constant. If the vortex field is perturbed with left circularly polarized (LCP) Gaussian beam with field components $\mathbf{E}_x = \varepsilon\,\mathrm{expi}(kz-\omega t)$, $\mathbf{E}_y = i\varepsilon\,\mathrm{expi}(kz-\omega t)$, where ε is real constant, The total field of the perturbed beam is a superposition of the vortex field and Gaussian field and is written as

$$\begin{aligned}\mathbf{E}_x &= (\varepsilon + kx + iky)\,\mathrm{expi}(kz - \omega t)\\ \mathbf{E}_y &= i(\varepsilon - kx - iky)\,\mathrm{expi}(kz - \omega t)\end{aligned} \tag{4.2}$$

At the vortex point on the z = 0 plane where x = y =0, the field is perturbed LCP point and around this point the polarization ellipse execute the fine structure due to the different phase and amplitude of the two beams. The S-surface where the polarization is linear is obtained by applying the following conditions on eqn. (4.2): any one component of the field goes to zero or the two field components are parallel or anti-parallel to each other. These conditions result in

$$\frac{\varepsilon + kx}{ky} = \frac{ky}{\varepsilon - kx}$$

or

$$(kx)^2 + (ky)^2 = \varepsilon^2 \tag{4.3}$$

The eqn. (4.3) represents a circle of radius ε / k .The places where the orthogonal circularly polarized components of the vortex beam and the Gaussian beam have the same amplitude results in a linear polarization and the

collection of all such points forms a closed circle. The closed circle separates the right and left circular polarization regions of the superposed beams. From eqn. (4.3) the left hand polarization is surrounded by the sea of right hand polarization and depending on the amplitude strength of ε the size of the S-line will vary. From the sign rule: the handedness of the wave in which the C-point is located, the singularity index of the C-point and the sign of the screw dislocation in phase are connected by the relation [6, 82]

$$\textit{sign of the handedness} \times \textit{sign of index} = \textit{sign of the screw}$$

In the above case the sign of the handedness of polarization is negative (-) and the sign of the screw dislocation is positive (+) hence the sign of the C-point is negative (-). From the above rule it is also clear that by changing the topological charge of the vortex beam or the handedness of the Gaussian beam one can switch between the different topological charges of the C-point. However, in order to achieve switching between the different orientations of the C-point we need inhomogeneous optical beam with controllable parameters to change the topological charge of the vortex beam without changing the handedness of the Gaussian beam or by changing the handedness of the Gaussian beam without changing the topological charge of the vortex beam. Inhomogeneous optical medium such as optical fibers are an effective means to manipulate the generation of isolated C-point to switch between different index of the C-point.

4.2 Generation of Isolated C-point

The formation of isolated polarization singularities in the output of optical fiber is due to the coherent superposition of the circularly polarized vortex mode with the orthogonal circularly polarized fundamental Gaussian mode within the

fiber. The four CP vortex modes of the step-index fiber are $TE_{01} \pm iTM_{01}$ and $HE_{21}^{e} \pm iHE_{21}^{o}$ as discussed in Sec 1.4. The coherent superposition of these modes with the circularly polarized fundamental mode is distinguished by the rotation of the zero intensity point (ZIP) within the beam cross section with respect to a rotating analyzer and stationary screen. If the ZIP rotates in the same way as the analyzer the output mode is due to the combination of orthogonal circularly polarized fundamental Gaussian mode with circularly polarized $TE_{01} \pm iTM_{01}$ vortex mode whereas for the combination of circularly polarized fundamental mode with orthogonal circularly polarized $HE_{21}^{e} \pm iHE_{21}^{o}$ vortex mode, the ZIP in the output beam rotates opposite to the analyzer rotation direction. Further, the topological charge of the mode is distinguished by the condition of the formation of isolated polarization singularities, which requires that the fundamental mode and the vortex mode should be orthogonally polarized. With this condition and the analyzer rotation we can clearly identify the output mode combinations and its topological charge. For example, right circularly polarized fundamental Gaussian mode $\sigma = +1$ coherently superposed with either the left circularly ($\sigma = -1$) polarized $HE_{21}^{e} + iHE_{21}^{o}$ vortex mode with topological charge -1 or left circularly polarized $TE_{01} + iTM_{01}$ vortex mode with topological charge -1 results in the formation of isolated C-point of index $I_C = +1/2$.

4.3 Experimental details

The schematic diagram of the experimental setup used to generate isolated polarization singularities using two mode fiber (TMF) and to characterize them

is shown in Fig.4.1. Partially polarized Gaussian (TEM_{00}) beam from a He-Ne laser (632.8 nm) pass through a Glan-Thompson polarizer (P) to obtain linearly polarized light. The linearly polarized light then passes through a quarter wave plate (QWP1) oriented at 45° or 315° to obtain right or left-circularly polarized (RCP or LCP) light respectively. The circularly polarized light beam is then focused using a 0.40 NA, 20x microscopic objective lens (L_1) onto the cleaved end of the circular core step-index TMF. The output from the fiber is collimated using another microscope objective lens (L_2).

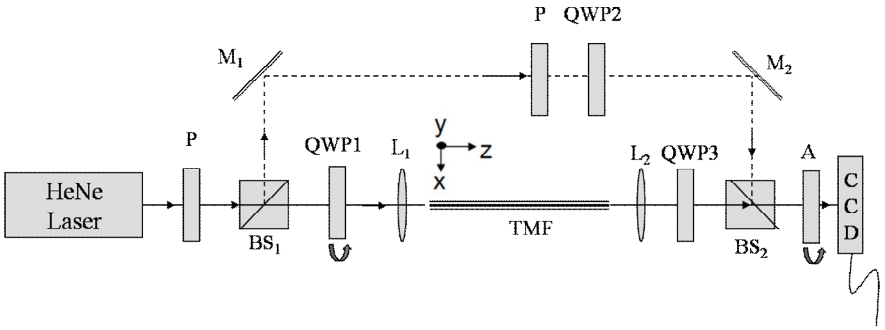

Figure 4.1: Schematic of the experimental setup used to generate isolated polarization singularities and the different diagnostic techniques to measure the S-line and C-point. BS- beam splitter, P- polarizer, QWP –quarter wave plate, L_1 and L_2 – microscopic objective lenses, TMF –two mode fiber, M_1 and M_2 – mirrors, A- analyzer, CCD – charge coupled detector.

In the second arm of the interferometer, used to measure the phase structure of the beams generated using TMF, a polarizer (P) and quarter wave plate (QWP2) are used to generate a circularly polarized reference beam for off-axis interference. The quarter wave plate (QWP3) after the objective lens L_2 is used in two different methods: in the interferometric method it generates different a-lines to measure the C-point and in the complex Stokes parameter method it is used to measure the S_3 component. The analyzer (A) after the

second beam splitter (BS_2) is also used in two methods: in the interferometric method it is used to select the same state of polarization from the fiber output beam and the reference beam and, in the Stokes method it is used to measure the three Stokes parameters as mentioned in 3.2.2.

4.4 Results and discussion

The input QWP1 oriented at 45° generates right circularly polarized (RCP) light ($\sigma = +1$) which is coupled into the fiber by placing its cleaved end at the focal plane of the objective lens (L_1). By adjusting the x and y positions of the fiber holder to a particular position we excite both the fundamental mode and the circularly polarized vortex mode simultaneously in the fiber output. The resultant fiber output mode passing through the analyzer (A) rotated in counter clockwise direction shows that the ZIP rotates in the same direction as the analyzer. This behavior implies that the left circularly polarized $TE_{01} + iTM_{01}$ vortex mode with topological charge +1 is predominant in the output beam which is coherently superposed with the fundamental RCP mode.

4.4.1 Interferometric method

In this method for measuring the S-contour, we removed the QWP3 from the setup and the QWP2 in the reference arm is oriented in such a way that it generates RCP reference beam for off-axis interference. The interfering reference beam and the output beam from the fiber pass through the analyzer (A) which selects the same field component from the two beams to form the interference forklet pattern. The analyzer (A) is rotated from 0° to 180° in steps of 10° to measure a series of S-points as mentioned in Sec 3.2.1. The rotation of the analyzer results in the rotation of the ZIP which in turn results in the rotation of the forklet pattern. The measured forklet patterns (insteps of 30°) are shown

in Fig.4.2 (A), where the position of the forklet is identified by white circle. From the interference measurement it is clear that the forklet rotates in the counter clock wise direction and makes one complete circle for 180^0 rotation of the analyzer. The S-contour is constructed from this set of measurements by finding the coordinates of base of the forklet pattern for each orientation of the analyzer and all these points are projected onto the original image of the output beam as shown in Fig.4.2 by white dotted line. For finding the C-point, the QWP3 is inserted in the experimental setup to generate different azimuth lines (a-lines) as mentioned in 3.2.1. For two different orientations of the QWP3 and by rotating the analyzer from 0° to 180° (in steps of 10°) for each orientation we measure the different a-lines by measuring the coordinates of forklet pattern. The projections of the two a-lines, a_1 and a_2 onto the output image are shown in Fig.4.2 as continuous white lines. The point of intersection of these two a- lines within the S-contour is the C-point. Along the a-lines the direction of the major axis of the polarization ellipse makes a $\pi/2$ jump while crossing the C-point as indicated by the yellow colour arrows in Fig.4.2 (B).

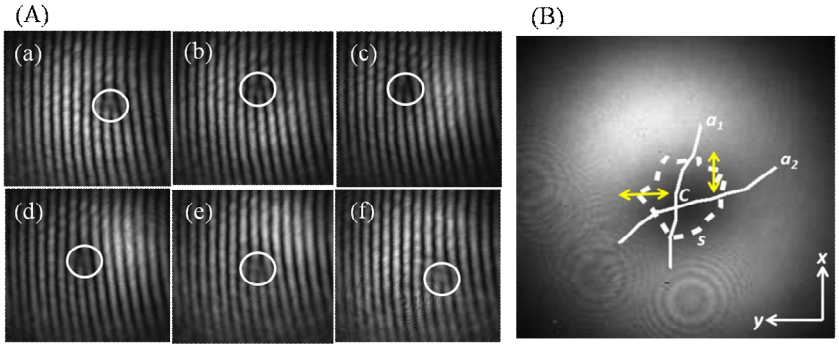

Figure 4.2: (A) Interference forklet patterns for different analyzer orientations, to track the S-line trajectory (a) 0° (b) 30° (c) 60° (d) 90° (e) 120° (f) 150°. (B) Superposition of S-points (white dot) and a-lines (continuous white lines) on the fiber output image. The intersection point of the two a-lines is the C-point.

4.4.2 Complex Stokes parameter method

The four Stokes parameters are measured experimentally from the six intensity measurements: I(0; 0), I(π/2; 0), I(π/4; 0) and I(3π/4; 0) are measured by orienting the analyzer (A) at 0°,90°,45° and 135° angles without the QWP3 in the output beam and I(π/4; π/2) and I(3π/4; π/2) measured by introducing the QWP3 before the analyzer (A), with its fast axis oriented at 90°, and recording the intensities for the analyzer angles 45° and 135° respectively. From the six intensity images measured using the CCD, the Stokes parameters are obtained for each pixel using the intensity value at the same coordinates from the images. The point wise calculation of the four Stoke parameters of the output beam is as shown in Fig.4.3. From the custom Stokes parameter 's_3' it is clear that the right circularly polarized light is surrounded by the sea of left circularly polarized light.

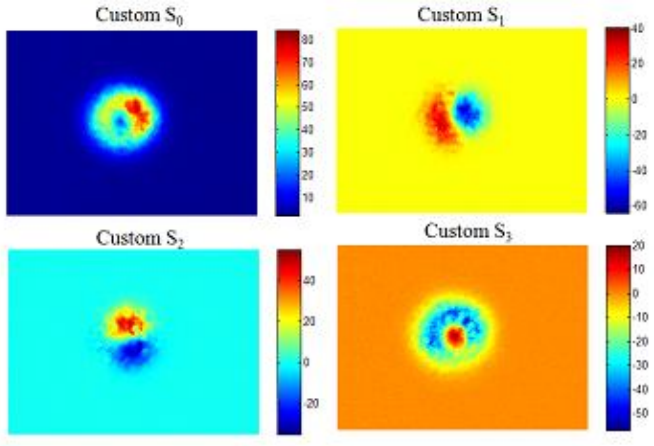

Figure 4.3: Point-wise Stokes parameters (S_0 – S_3) of the output beam from the fiber plotted in '*Custom*' scale to highlight the contributions of the different polarizations to the overall beam.

The polarization singularities are located and characterized by method described in 3.2.2. The normalized Stokes parameters are used in our analysis to measure S-line and C-point. The S-line is measured by making complex Stokes parameter s_3=0, is shown in Fig.4.4 (a) as a dark line on white background and the C-point is measured by making normalized Stokes parameters s_1=s_2=0, is as shown in Fig.4.4 (b) as a dark point. The location of the C-point is determined to an accuracy of approximately five pixels. The orientation angle of the ellipse around the C-point which gives the sign of the C-point is measured using $\alpha = \frac{1}{2}\arg(s_1 + is_2)$, is shown in Fig.4.4 (d). The polarization ellipse around the C-point rotates in the clockwise direction. Hence the topological charge of the C-point is +1/2.

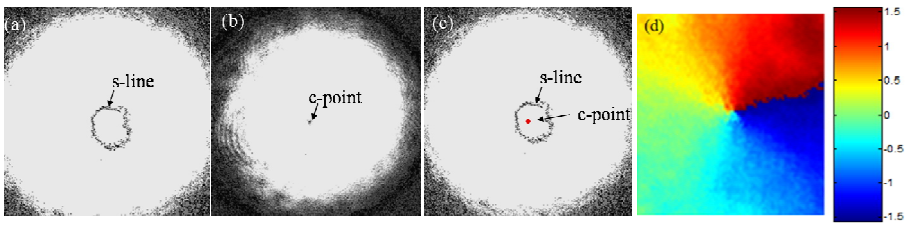

Figure 4.4: Measurement of the polarization singularities (a) S- contour as a dark line (b) C-point (dark point) (c) the coordinates of the C-point are overlapped on the S-line (d) polarization ellipse orientation around the C-point, index of $I_c = +1/2$.

4.4.3 Comparison between the two methods

Comparison of the results obtained using the interferometric and complex Stokes parameter methods, for the measurement of S-line in the output beam from the optical fiber is shown in Fig.4.5. It is clear from the figure that the two results are in good agreement with each other, with the Stokes parameter method found

to give a more precise location of the polarization singularities. This difference in accuracy is particularly pronounced in the location of C-points. The Stokes parameter method is only limited by the resolution of the CCD whereas in case of interferometry, possible errors include those while tracing the *a*-lines and also due to limitations in determining the point of intersection of *a*-lines due to the spacing between data points. Also, the Stokes parameter method involves a simpler arrangement of optical components and is more robust compared to the interferometric method. Also, manual identification of the position of the fork in the CCD images containing the interference pattern is prone to errors and the width of the fringes is also a limiting factor in accurately determining the location of the singularity.

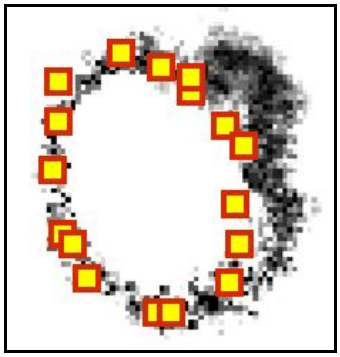

Figure 4.5 The measured L-points using the interferometric method (yellow squares) superimposed on the L-line measured from complex Stokes method (black dots).

4.4.4 Switching between different C-points

The experimental setup used to switch between the different C-points is the same as shown in Fig.4.1. Initially, the input QWP1 is oriented such that right circular polarized (RCP) light ($\sigma = +1$) is coupled into the fiber by placing its cleaved end at the focal point of the objective lens (L_1). By adjusting the fiber x- and y- positions to a particular launch angle configuration I_1 (Fig.2.2 (b)), we get our output beam as shown in Fig.4.6 (a), measured using the CCD camera. The ZIP of the output beam (Fig.4.6 (a)) passing through the analyzer (A) rotated in counter-clock wise direction rotates in the same way. This behavior implies that the LCP $TE_{01} + iTM_{01}$ vortex mode with topological charge +1 is predominant in the output beam which is coherently superposed with the RCP fundamental mode inside the fiber. When the QWP1 is rotated by 90^o without changing the input launch conditions, the LCP light ($\sigma = -1$) is coupled into the fiber and the corresponding output beam is shown in Fig.4.6 (b). As the handedness of the input beam polarization is reversed, the ZIP rotates in a direction opposite to the analyzer rotation direction implying that the RCP $HE_{21}^{e} - iHE_{21}^{o}$ vortex mode with topological charge +1 is predominant in the output beam which is coherently superposed with the LCP fundamental mode. The different combinations of the output modes for the RCP and LCP input beams guided in the fiber are due to the change in the direction of circulation of the polarization of the beam which results in a change in the angular orientation of the trajectory of the local transverse modes in the fiber due to optical Magnus effect [41] or spin-Hall effect of light [105].

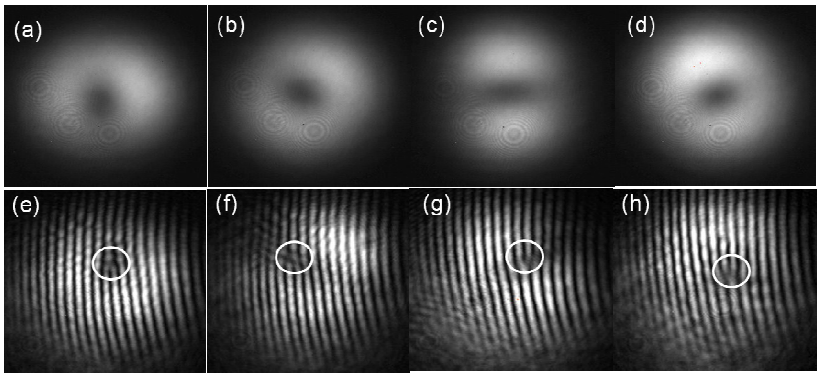

Figure 4.6: (a) – (d) output beam from the fiber for four different input launch conditions. (e) – (h) the corresponding interference forklet patterns marked in a white circles. The sign convention of the topological charge of the output beams is +1 for down fork and -1 for up fork.

Next, by changing the input launch angle from I_1 to a diametrically opposite position I_2 as shown in Fig.2.2 (b), by adjusting the fiber x- and y-positions, we find that for RCP input beam the ZIP rotates opposite to the analyzer rotation implying that LCP $HE_{21}^{e} + iHE_{21}^{o}$ vortex mode with topological charge -1 is predominant in the output beam which is coherently mixed with the RCP fundamental mode. For the LCP input beam, the ZIP rotates in the same direction as the analyzer implying that the RCP $TE_{01} - iTM_{01}$ vortex mode with topological charge -1 is predominant in the output beam which is coherently superposed with the LCP fundamental mode in the fiber. The formation of different output mode combinations for different input launch angles I_1 and I_2 is due to the Rytov effect in the fiber, which influences the rotation of the plane of polarization for the two different launch angles. The output beams from the fiber for all the four input conditions discussed are given in Fig.4.6 (a – d). The corresponding off-axis two-beam interference patterns, showing the characteristic forklet pattern to recognize the topological charges of the output

beams are shown in Fig.4.6 (e – h). Changing the launch angle from I_1 to I_2 clearly changes the forklet orientation from down to up, indicating change in the vortex charge from +1 to -1.

Next the polarization characteristics of the four output beams from the fiber are measured using the complex Stokes parameter method described earlier in Sec.3.2.2. The C-point and the S-contour for all the four output beams are shown in Fig.4.7 (a – d). It is important to note that the shape of the S-contour which can provide more information about the purity of the vortex modes along with the analyzer rotation for all the four cases. In the case of I_1 RCP input and I_2 LCP input the output mode S-contours are close to circles as shown in Fig.4.7 (a, d). This indicates that the output beam is a pure combination of the fundamental mode and $TE_{01} \pm iTM_{01}$ vortex modes. For I_1 LCP input and I_2 RCP input, the output mode S-contour are elliptical (Fig.4.7 (b, c)) which indicates a mixing of other fiber modes along with the fundamental and vortex $HE^{e}_{21} \pm iHE^{o}_{21}$ modes in the output mode.

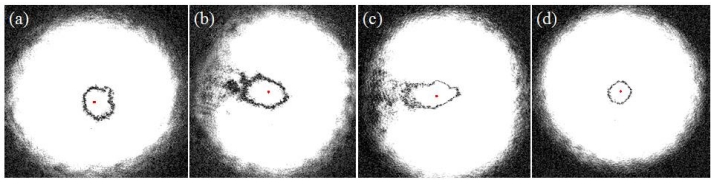

Figure 4.7: The C-point and s-line of four output modes, S-lines are represented as closed black contours and the C-points are marked as red dots inside the S-line (a) RCP input I_1, (b) LCP input I_1, (c) RCP input I_2, and (d) LCP input I_2.

The SOP map measured from the Stokes parameters for all the four output modes from the TMF are shown in Fig.4.8 (a- d). From this it is clear that the output beams are either RCP fundamental mode surrounded by the LCP vortex or the LCP fundamental mode surrounded by the RCP vortex mode

combination. The orientation of the major axis of the polarization ellipse around the C- point measured using $\alpha = \arg(s_1 + is_2)$ are shown as hue plots in Fig.4.9 (a – d) for all the four conditions of the input beam.

In the case of RCP and LCP input beams, at input launch angle $I_{1,}$ both the output vortex modes have the same topological charge of +1 indicated by the down forklet in Fig.4.6(a, b) but the corresponding orientation index of the C-point changes from +1/2 (lemon) to -1/2 (star) as shown in Fig.4.8(a, b). This behavior clearly indicates that changing the polarization handedness of the fundamental mode from RCP to LCP with the same topological charge +1, the orientation angle of the C-point is changes from +1/2 to -1/2 as shown in Fig.4.9 (a, b).

Similarly, for the input launch angle I_2 for RCP and LCP input beams, the C-point index changes from -1/2 (star) to +1/2 (lemon) for the vortices with same topological charge of -1. Similar behavior is observed for orientation index of the C-point when the topological charge of the vortex beam is changed from +1 to -1 and keeping the polarization of the fundamental mode the same. For the input RCP at I_1 and I_2, output beams have different topological charges of down and up forklet as shown in Fig.4.6 (a, c) but the corresponding orientation index of the C-point changes from +1/2 to -1/2 as show in Fig.4.9 (a, c). Similarly, for input LCP at I_1 and I_2 the topological charge of the C-point changes from -1/2 to +1/2 (Fig.4.9 (b, d)).

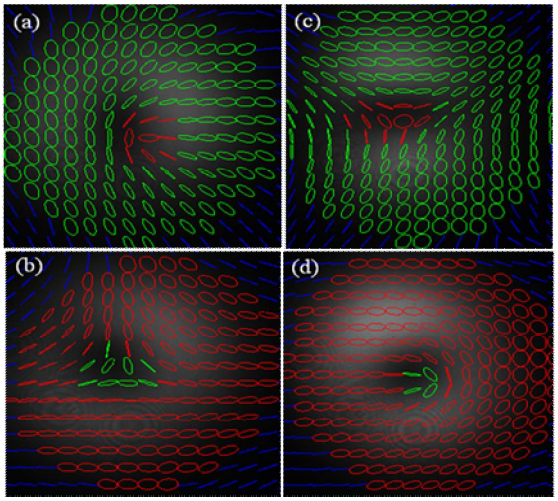

Figure 4.8: Polarization ellipse superposed on the original images of the four output beams, (a) RCP input I_1 (b) LCP input I_1, (c) RCP input I_2, and (d) LCP input I_2**.** Red: right handed polarization ellipse green: left handed polarization ellipse, blue: no light/linearly polarized.

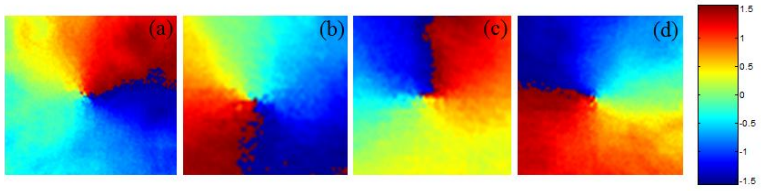

Figure 4.9: Hue plots of the polarization ellipse orientation around the C-point: (a) RCP input I_1 $I_c = +1/2$ (b) LCP input I_1, $I_c = -1/2$ (c) RCP input I_2, $I_c = -1/2$ and (d) LCP input I_2**,** $I_c = +1/2$

From the above analysis and discussion of the results obtained it is clear that the orientation index of the C-point changes by changing the handedness of the fundamental mode with same topological charge of the vortex mode or by changing the topological charge of vortex modes with same handedness of the fundamental mode.

4.4 Summary

To summarize the results presented in this section, we generated isolated polarization singularities (S-line and C-point) in the output of the two mode fiber, due to the coherent superposition of circularly polarized fundamental Gaussian mode with orthogonal circularly polarized vortex mode. Such an output beam is achieved by coupling circularly polarized Gaussian beam into the TMF as offset-skew beam. The polarization singularities S-line and C-point are characterized by interferometric and complex Stokes parameter methods. The results obtained using the two methods are in good agreement with each other with the complex Stokes parameter method providing a more reliable and easier method for such measurements than the interferometric method. We also demonstrated controllable switching between the different topological charges of the C-points ($\pm 1/2$) generated using the two-mode fiber. The structure of these singularities depends on the launching conditions at the input end of the optical fiber and the handedness of circularly polarized light coupled into the fiber. The S-contour surrounding the C-point shows significant distortion when the polarization of the input beam and the input launch condition are changed. The orientation index of the C-point changes by changing the handedness of fundamental mode with same topological charge of the vortex modes or by changing the topological charge of vortex modes with same handedness of the fundamental mode.

Chapter 5

Applications of Polarization Singular Beams

In this chapter, we present two applications of isolated polarization singularities: (i) the rotational Doppler-effect (RDE) and (ii) the characterization of the Dove prism (DP) (used to invert the topological charge of the OV and to demonstrate RDE). We demonstrate our experimental results on the RDE in a stationary two-mode optical fiber due to the simultaneous excitation of the vortex mode and the fundamental mode inside the fiber. The RDE is demonstrated by tracking the singularity or zero intensity point as a function of the output analyzer rotation with respect to a stationary screen. The ZIP moves on the S-contour and for one complete rotation of the analyzer (Ω), the singularity point rotates twice. We also measured the beam behavior as a function of rotation of the Dove prism and half-wave plate – Dove prism combination to understand the role of phase and polarization modifying components on the observed RDE. The DP with 45° base angle is characterized using the well defined S-contour and C-point. The S-contour and the C-point are sensitive to the polarization, phase and amplitude perturbations introduced by the DP. By tracking the shape of the S-contour and the C-point position after the Dove prism as it is rotated around its axis we characterize the perturbations introduced by the DP. The shape of the S-contour and the polarization ellipse around the C-point gives information about the polarization and the phase distortion of the DP.

5.1 Rotational Doppler-effect

The relative velocity between a source and an observer leads to frequency shift which is proportional to the product of the velocity and the unshifted frequency is a well known phenomenon of (non-relativistic) translational Doppler-effect (TDE) or linear Doppler-effect (LDE). The relation between the observed frequency 'f' and the source frequency 'f_0' is;

$$f = \left(\frac{v \pm v_o}{v \mp v_s} \right) f_0 \qquad (5.1)$$

Where 'v' is the velocity of waves in medium, 'v_o' and 'v_s' are the velocity of the observer and the source respectively. In this expression (eqn. (5.1)), the upper signs ($+v_o$ and $-v_s$) refer to motion of one toward the other, and the lower signs ($-v_o$ and $+v_s$) refer to motion of one away from the other.

The optical vortex beam with helical phase structure ($\exp il\varphi$) experiences change of its phase and frequency upon rotation of the beam with respect to a stationary screen known as rotational Doppler-effect (RDE). In other words, the number of wavefronts passing through a plane in a unit time is equal to the optical frequency change due to rotational effect. The rotation of the beam with '*l*' intertwined helical wavefronts changes the wave fronts passing through this plane by '*l*', hence, the frequency shift is equal to' $l\Omega$'. The RDE is different from the LDE for rotating bodies due to the rotation having linear velocity with respect to the observer. In RDE, the axis of rotation is parallel to the propagation vector and is maximum in the direction of the angular velocity 'Ω', where the LDE is zero.

The classical effect of observing the hands of a watch kept at the center of a rotating stage and rotating in the clockwise direction when viewed from the top appears to rotate fast is known for a long time. This simple observation is

known as due to the rotational Doppler-effect. The effect can be extended to the rotation of the electric field vector of a circularly polarized light beam, which also carries spin angular momentum to either speed up or slow down the beam rotation about its propagation axis resulting in the frequency broadening or frequency shift proportional to the rate of rotation of the field vector or the total angular momentum of the beam [106, 107]. First demonstrated by Garetz and Arnold, the frequency of circularly polarized light ($\sigma = \pm 1$) transmitted through a half-wave plate rotating at frequency $\Omega/2$ is measured to be shifted by $\sigma\Omega$ [108]. Associated with this angular Doppler-effect, the rotational frequency shift manifests itself whenever light is emitted, absorbed or scattered by rotating bodies [109, 110]. Analogously, an atom moving in a light beam with orbital angular momentum (OAM), a Laguerre-Gaussian (LG_n^l) beam for example, experiences an azimuthal shift in its resonant frequency [111].

In general, for circularly-polarized LG beams with both spin (σ) and orbital (l) components of the angular momentum, the Doppler frequency shift is proportional to the total angular momentum ($\sigma + l$) which has been quantified directly for the rotation of EM beams at millimeter wavelengths [112]. Subsequently, the angular Doppler-effect was made use of in an elegant demonstration of moving interference patterns in the optical domain for controlled rotation of trapped particles [113]. The RDE was also demonstrated for helical wavefront-vortex optical beams generated using a spiral zone plate [114] and in off-axis optical vortex beam generated using a holographic grating [115]. Further, an OAM spectrum analyzer was demonstrated utilizing the rotational Doppler frequency shifts imparted to LG modes with different '*l*' values [116].

Though different manifestations of the RDE have been demonstrated in free-space and in atomic and molecular systems using scalar optical beams with OAM, very few demonstration of the effect exist in the waveguide medium [117 – 119]. In addition to being a practically important system, optical fibers are an interesting class of inhomogeneous medium wherein the guided optical vortices (OVs) can co-exist with the vector eigen modes of the fiber wherein the OAM of the light is redistributed among the different fiber eigen modes [118, 119]. The resulting optical vector-vortex beams excited in fibers offers an unique opportunity to study the interplay between the OAM of the light beam redistributed among the spatially (temporally) varying electric field vector of the guided modes. Recently, the possibility of observing RDE in stationary and rotating optical fibers was proposed and subsequently observed in few-mode fibers by launching an externally-generated LG beam into the fiber [117 – 119]. In our method, the RDE is demonstrated in a stationary two-mode step-index fiber by simultaneously exciting the fundamental and the vector-vortex modes and passing the output beam through a rotating analyzer with respect to the stationary screen. The fundamental and vortex modes are excited in the TMF by circularly-polarized Gaussian beam.

5.1.1 Theoretical details

Considering the fiber output as a coherent superposition of the fundamental and vortex mode within the fiber that the transverse electric field distribution at the fiber output (in free space) can be written as

$$\mathbf{E}_t = (\hat{\mathbf{x}} + i\sigma_1\hat{\mathbf{y}})a\exp(-R^2) + (\hat{\mathbf{x}} + i\sigma_2\hat{\mathbf{y}})R\exp(-R^2 + i\sigma_2\varphi) \quad (5.1)$$

where, ‘a’ is the relative amplitude, ‘φ’ is the helical phase of the vortex beam, ‘R’ is the radial distance, x and y are the unit vectors, σ_1 and σ_2 are the

handedness (±1) of the Gaussian and vortex modes respectively. In the above expression the sign of the handedness and the topological charge of the vortex mode are the same. If they are different, the above equation can be rewritten as

$$\mathbf{E}_t = (\hat{\mathbf{x}} + i\sigma_1\hat{\mathbf{y}})a\exp(-R^2) + (\hat{\mathbf{x}} + i\sigma_2\hat{\mathbf{y}})R\exp(-R^2 - i\sigma_2\varphi) \tag{5.3}$$

Introducing an analyzer, we get the projection of the field of the output beam and rotating it by an angle $\theta = \Omega t$, where 't' (sec) is time and 'Ω' is the angular frequency (Hz) of the analyzer, results in the rotation of the position of vortex core or the singularity point, (ZIP). The position of the ZIP in the beam cross section is obtained by applying the condition $\mathrm{Re}\,\mathbf{E}_\theta = \mathrm{Im}\,\mathbf{E}_\theta = 0$ to eqn. (5.2) (see Appendix 2 for derivation details)

$$a + \mathrm{Re}\exp\{i(\sigma_2[\theta - \varphi]) - \sigma_1\theta\} = 0 \tag{5.4}$$

Equating the real and imaginary parts of eqn. (5.4) to zero, the ZIP coordinates are given as

$$R = a, \qquad \varphi = \pi/\sigma_2 + (1 - \frac{\sigma_1}{\sigma_2})\theta \tag{5.5}$$

The above eqn. (5.5) indicates that the ZIP rotates even in the non-rotating coordinate system associated with a fixed screen placed after a rotating analyzer. The ZIP rotation with respect to the stationary screen is

$$\Delta\Omega = \frac{\partial\varphi}{\partial t} = (\frac{\sigma_1}{\sigma_2} - 1)\Omega \tag{5.6}$$

From eqn. (5.3) if the vortex mode has opposite sign for handedness and topological charge, the ZIP rotation with respect to the stationary screen is

$$\Delta\Omega = \frac{\partial\varphi}{\partial t} = (1 - \frac{\sigma_1}{\sigma_2})\Omega \tag{5.7}$$

From eqn. (5.6) and eqn. (5.7), for the same circular polarization of the Gaussian mode and the vortex mode i.e., $\sigma_1 = \sigma_2$, the modes corresponding to ZIP do not rotate at the stationary screen whereas for the case of orthogonal circular polarizations of $\sigma_1 = -\sigma_2$, the angular frequency of the ZIP at the stationary screen is $\Delta\Omega = -2\Omega$ for the vortex mode with same sign of handedness and topological charge (eqn. (5.6)) where as $\Delta\Omega = +2\Omega$ for the vortex mode with an opposite sign of handedness and topological charge (eqn. (5.7)).

The two different rotations (2Ω and -2Ω) of the output beam from the two-mode step-index optical fiber is possible by selectively exciting the appropriate fundamental and vortex mode combinations within the fiber. For example, when the right circularly (+1) polarized fundamental mode is coherently superposed with the left circularly (-1) polarized vortex mode with topological charge +1, (the handedness and topological charge of the vortex mode are opposite), using eqn. (5.7), the output beam after passing through the rotating analyzer with respect to stationary screen rotates at +2Ω. Whereas for a vortex beam with topological charge -1, when the handedness and the topological charge of the vortex mode are the same, from eqn. (5.6), the output mode after the rotating analyzer with respect to a stationary screen rotates at -2Ω. In our experiment we achieved RDE beams by coupling circularly polarized Gaussian beam into the TMF and by adjusting the fiber input launch conditions at two different launch angles.

5.1.2 Results and discussion

Schematic of the experimental setup used to demonstrate the rotational Doppler-effect using appropriate modes excited in the two-mode optical fiber is the same as shown in Fig.4.1. In Chapter-4, in the isolated polarization singularities generated using the TMF, all the four output modes are coherent superposition of orthogonal circularly polarized fundamental Gaussian mode and vortex mode as discussed in detail in Sec-4.4.3. Let us re-write all the four combination in a convenient representation to identify the handedness of the fundamental and vortex mode and the topological charge of vortex mode as (σ_1, (σ_2, l)) where $\sigma_1(\pm 1)$ is the polarization handedness of the fundamental mode, σ_2 (± 1) handedness of the vortex beam and 'l' is topological charge (± 1) of vortex mode. For RCP ($\sigma = 1$) input beam, the output modes are (1, (-1, 1)) and (1, (-1, -1)) as shown in Fig.4.5 (a, c) whereas for LCP ($\sigma = -1$) input beam, the output modes are (-1, (1, 1)) and (-1, (1, -1)) as shown in Fig.4.5 (b, d). All the four mode combinations satisfy the conditions of RDE but depend upon the sign of the vortex mode handedness and the topological charge the RDE changes as discussed earlier.

For the vortex modes with same handedness and topological charge i.e., (1, (-1 -1)) and (-1, (1 1)), the ZIP rotates at the stationary screen as $\Delta\Omega = -2\Omega$ (eqn. (5.6)) whereas for the vortex mode with opposite handedness and topological charge (1, (-1 1)) and (-1, (1 -1)), the ZIP rotates at the stationary screen as $\Delta\Omega = +2\Omega$ (eqn. (5.7)). Since all the four generated modes exhibit rotational Doppler-effect for the rotating analyzer with respect to the stationary screen, we selected one mode combination (-1, (1 -1)), to demonstrate the RDE in the fibers. The output beam generated by the TMF with suitable topological charge and polarization of the vortex and fundamental mode is passed through

the analyzer rotating in the counter clockwise direction in steps of 5° (shown in Fig.5.1, in steps of 30°), the ZIP rotates the same way as the analyzer.

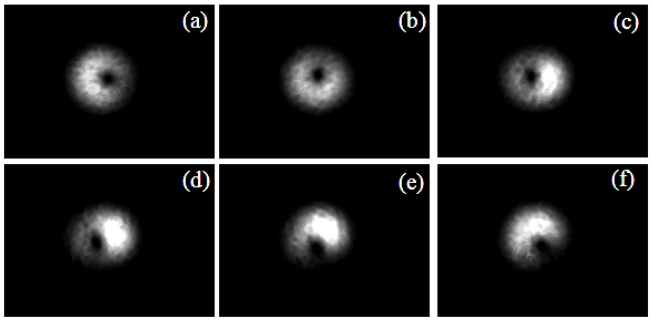

Figure 5.1: Output images after the rotating analyzer insteps of 30°: (a) 0° (b) 30° (c) 60° (d) 90° (e) 120° (f) 150°

From the images we calculate the X and Y coordinates of the geometric centre of the beam and the ZIP (denoted respectively as X_c, Y_c, X_{min} and Y_{min}) using MATLAB program (discussed in Chapter 2). From these measurements we calculate the ZIP rotation with respect to the beam centre as a function of the analyzer rotation. The X-Y coordinates of the ZIP as a function of the analyzer rotation is shown in Fig.5.2. It is seen from the figure that the ZIP trajectory for a rotating analyzer with respect to stationary screen makes two (4π) rotations for one (2π) rotation of the analyzer implying that the angular frequency ($\Delta\Omega$) of the ZIP is twice the angular frequency of the analyzer (Ω) i.e., $\Delta\Omega = 2\Omega$. It is important to note that the trajectory of the ZIP exactly corresponds to the S-line trajectory measured using the Stokes parameters (Fig.4.8). To identify the C-point in the output beam, we introduced a QWP in the output beam as discussed in Sec 3.2.1 at fixed QWP angles of 8° and 33°. The beam passing through the rotating analyzer 'A' gives us the azimuth curves

s_1 and s_2 respectively as shown in Fig.5.2. The intersection of the two curves within the S-contour is the C-point

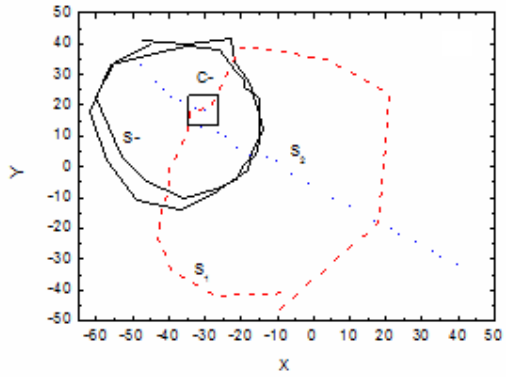

Figure 5.2: Polarization singularities – S-lines and C-point – in the output from the TMF excited by left-circularly polarized Gaussian beam.

Next, the output beam is passed through a rotating DP and HWP-DP combination to study the phase and polarization effects on the RDE. The DP inverts the vortex location by 180° due to one total internal reflection at the prism base and it changes the topological charge of the vortex beam from -1 to +1. For such a beam, one complete rotation of the DP in the CCW direction with respect to the beam axis results in the CCW rotation of the ZIP at twice the angular rotation frequency due to the image rotation property of the DP [16]. The X-Y plot of the ZIP rotation as function of the DP angle (Fig.5.3) shows a symmetric circular trajectory for the rotation around the beam center at twice the rotation frequency of the DP. To study the effect of DP on the RDE of the vortex beam passing through it, we fix the DP at every 22.5° and rotate the analyzer kept after the DP in the CCW direction. In this case the ZIP or the singularity point after the CCW rotating analyzer rotates in the CW direction, this behavior is due to the sign flip in the topological charge of the vortex beam

so that the handedness and topological charge of the vortex beam have the same sign, and from eqn. (5.6) the output beam rotates opposite to the analyzer rotation. For every 45° orientation of the DP the X-Y plots of the ZIP as a function of analyzer rotation shown in Fig.5.3.

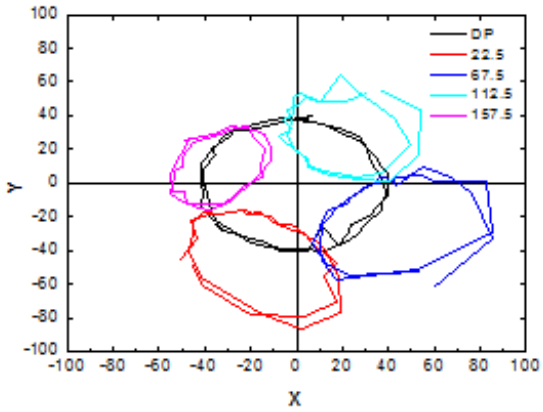

Figure 5.3: Rotation of the ZIP due to rotating DP (black) and analyzer rotation for different fixed orientation of the DP (colors).

In all the cases the ZIP rotates twice the rotation of the analyzer and all the trajectories go around the periphery of the DP rotation trajectory. For the DP oriented at 22.5° we see that the ZIP trajectory is more elliptical and is less elliptical for the DP orientation of 157.5°. This behavior is due to the polarization leakage from the DP which we discuss in more detail in Sec 5.2.

Now the output beam is passed through the combination of half-wave plate and Dove prism introduced in the output beam from the TMF to rotate both the polarization and the image at twice the angular frequency. One complete CCW rotation of these two elements together rotates the ZIP or the singularity point twice in the CCW direction as shown by continuous (black) line central circle in Fig.5.4. As the output beam from the TMF is a combination of both left and right circular polarized light, introduction of a rotating HWP

changes the phase difference between the field components and hence the polarization of the beam passing through it by equal and opposite amount to both the circular components and hence the resulting behavior of $\Delta\Omega = 2\Omega$ of the ZIP. Next, we introduced a rotating analyzer after the HWP-DP combination positioned at different fixed angles to study the behavior of the polarization singularities (*S*-line and *C*-point) in the output beam. The trajectory of the *S*-line or the ZIP for every 45° orientation of the HWP-DP combination also rotates at twice the angular frequency of the analyzer rotation but now rotating in CCW direction. For a complete rotation of analyzer these trajectories go along the periphery of the circle measured for the HWP-DP ZIP trajectory as shown in Fig.5.4.

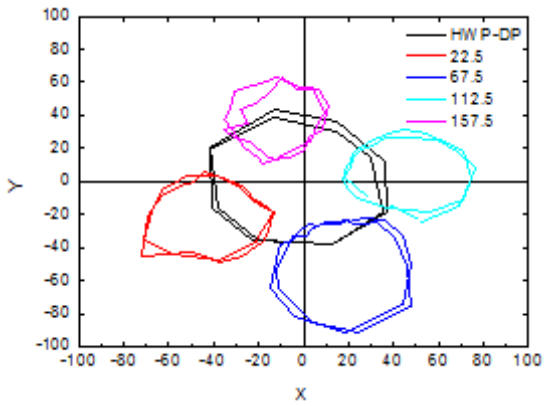

Figure 5.4: Rotation of the ZIP due to rotation of HWP-DP combination (black) and rotation of analyzer for different fixed orientation of the HWP-DP combination (colors)

The change in the direction of rotation of the ZIP trajectory as compared to that in Fig.5.3 is due to the introduction of the HWP which changes the rotation direction of the circular polarization of the output beam. Also, due to the introduction of additional phase to the output beam polarization by the

HWP, the starting point of the ZIP due to polarization singularity in the output beam changes its starting position. From the above sets of measurements, it is clear that with the DP and the HWP-DP combination, the ZIP rotates in the CCW direction whereas for the DP and HWP-DP combination at different angles, the CCW rotation of analyzer the ZIP rotates in CW direction for DP and it rotates in CCW direction for HWP-DP combination.

5.2 Characterization of Dove prism using polarization singularities

5.2.1 Introduction

Dove prism (DP) works on the principle of total internal reflection, due to which it flips the image in one transverse dimension, while leaving the image unchanged in the other transverse dimension [121]. The DPs have an interesting property that they rotate the beam along their longitudinal axis and for one complete rotation of the DP (Ω) the transmitted image rotates twice (2Ω) while keeping the line of sight undeviated [122, 123]. This property means that they can rotate a beam of light by an arbitrary angle. Due to these optical properties DPs are extensively used in image applications and interferometers to rotate one beam with respect to other [124, 125], in pattern-recognition systems [126], in metrology of rotating objects [127], in optical profilers [128] and in optical parametric oscillators [129, 130].

Recently, the DPs are also used to change the OAM of the LG beam by changing the helical phase from right to left or vice-versa. DPs are key elements of the interferometric method for measuring the orbital angular momentum OAM of single photons and the OAM content in a superposition of LG beams [131-132]. Using the beam rotation property of the Dove prism, RDE is demonstrated for homogeneously polarized beams and measured the frequency

shift [7, 131]. But in recent experiments it is found that the DP behaves as a polarizer with poor extinction (polarization leakage) ratio and that this ratio decreases with the increasing prism base angle [133-135]. The polarization leakage of the DP can be measured by rotating the DP kept in-between the parallel and crossed polarizers [133-135].

Since the DPs have extensive use in optical angular momentum related research, we characterize the polarization leakage of the DP by using inhomogeneously polarized singular beam. We demonstrated that the coherent superposition of orthogonal circularly polarized Gaussian mode and vortex mode inside a TMF forms a beam with well-defined polarization singularities (S-line and C-point) as discussed in Chapter 4. These polarization singularities are sensitive to external perturbations like polarization, phase and amplitude changes. The deformation in S-contour from its initial shape and the C-point position within the S-contour gives information about the polarization leakage, and the orientation of ellipse around the C-point (hue plot) will give the phase distortion due to the optical component. We used a beam with well-defined S-line and C-point to characterize the DP of 45° base angle by comparing the S-line and C-point before and after the DP and for every 22.5° rotation of the DP.

5.2.2 Results and discussion

To understand the behavior first, the DP is characterized using a linearly polarized Gaussian beam. The experimental setup used is shown in Fig.5.5. The polarization components are oriented such that the vertically polarized light is passed through the DP. Keeping the analyzer (A) orientation parallel and perpendicular to the input polarization we measure the intensity of the output beam for different orientations of the DP in steps of 10° from 0^o to 360°. For

analyzer axis oriented parallel and perpendicular to the input polarization, the intensity versus DP rotation angle measurements are shown in Fig.5.6 (a). When the analyzer axis is parallel to the input polarization the output intensity is modulated by 2Ω for one complete rotation of DP (Ω) but does not drop below the 75% of its peak value whereas for the perpendicular orientation of the analyzer axis, the output intensity is modulated by 4Ω with small intensity variation. The same measurements are repeated for the different input beam polarization of 45°, 90° and 135° by orienting the output analyzer parallel and perpendicular to the input polarization as a function of DP rotation angle. We observed the same behavior of the output intensity for the DP rotation for all the cases. For 45° linearly polarized input light the output intensity modulation is as shown in Fig.5.6 (b).

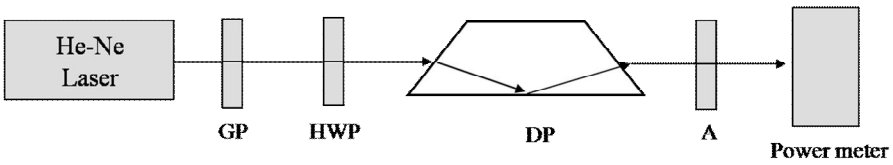

Figure 5.5: Schematic of the experimental setup to characterize the DP using linearly polarized light: GP- Glan-Thomson polarizer, HWP- half-wave plate, DP-Dove prism, A-analyzer

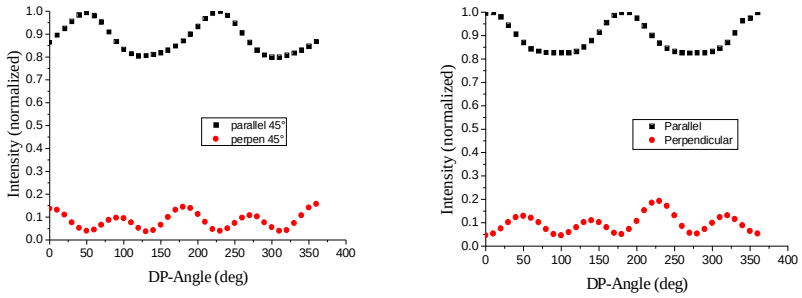

Figure 5.6: Intensity variation of the Gaussian beam as a function of DP rotation angle for vertical 0° and 45° polarized input beam.

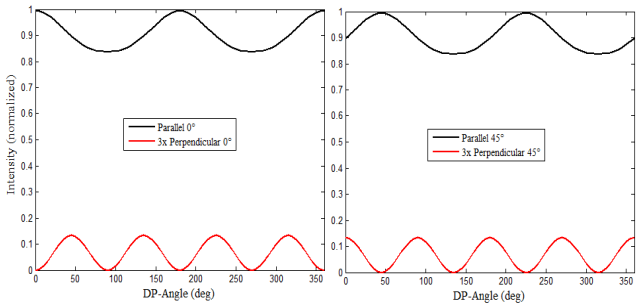

Figure 5.7: Matlab simulated plots for the two input polarizations in Fig.5.6.

To understand the DP behavior we simulated the experiment with DP in between parallel and perpendicular oriented polarizers by using the DP matrix, such as the input transmition, total internal reflection (TIR), and output transmition in between the rotation matrix and the polarization matrix for corresponding input and output polarizers in parallel and perpendicular cases as [133].

Output-parallel= Pol-parall **x** Rot **x** Tran-out **x** TIR **x** Tran-in **x** Rot **x** Pol-in **x** input (5.8)

Output-crossed = Pol-crossed **x** Rot **x** Tran-out **x** TIR **x** Tran-in **x** Rot **x** Pol-in **x** input (5.9)

The Matlab simulated plots for the intensity versus DP rotation for two input polarizations vertical (0°) and 45° are as shown in Fig.5.7 ((a) and (b)). The simulated results are found to match well with the experimental results.

Now the inhomogeneously polarized vortex beam generated using the TMF with well defined polarization singularities (S-line, C-point) with topological charge +1 and negative C-point index ($I_C = -1/2$) is passed through the DP oriented at 0°. The S-line, C-point and the ellipse orientation around the C-point before and after the DP are as shown in Fig.5.8. From the

figure the S-contour changes drastically for the output beam compared with the input beam. In order to get the S-contour information such as 'b/a' ratio and the area enclosed by the S-contour before and after the DP we draw a line around the S-contour shown in Fig.5.8 inset. The 'b/a' ratio of the input and output beams have the same value (0.95) but the area enclosed by the S-contour ($A=\pi\cdot a\cdot b=6.65$ pixel^2) in the output beam is double the area enclosed by the S-contour (3.3 pixel^2) in the input beam. The size of the S-contour can change only when the polarization states and the amplitudes of the combined Gaussian and vortex beams change as discussed in Sec 4.1.Hence the change in the S-contour after the DP is due to the polarization leakage from the DP, which effects the amplitudes of the Gaussian and the vortex beams.

For the input and output beams the position of the C-point inside the S-contour are identified (Fig.5.8 green dot) with respect to the geometric center of the beam (red dot), which will help us to understand the C-point motion with respect to geometric center within the S-contour for DP rotation. For the input beam with the C-point to the right of the geometric center moves to the left side of geometric point for the output beam, which is due to the total internal reflection in the DP. The orientation index of the C-point for the input beam is -1/2, and where the polarization ellipse around the C-point are rotates in the CCW direction changes to +1/2 for the output beam, with the polarization ellipse around the C-point rotating in the CW direction. The change in the C-point index is due to the change in the sign of the vibration phase or equivalently to the change in the sign of the topological charge of the vortex beam or the handedness of the Gaussian beam as discussed in Sec 3.1, following the relation $I_C = hS_C$. In this case the handedness of the Gaussian beam remains the same but the topological charge of the vortex beam changes

from the +1 to -1 due to the DP, which results in the change in the C-point index.

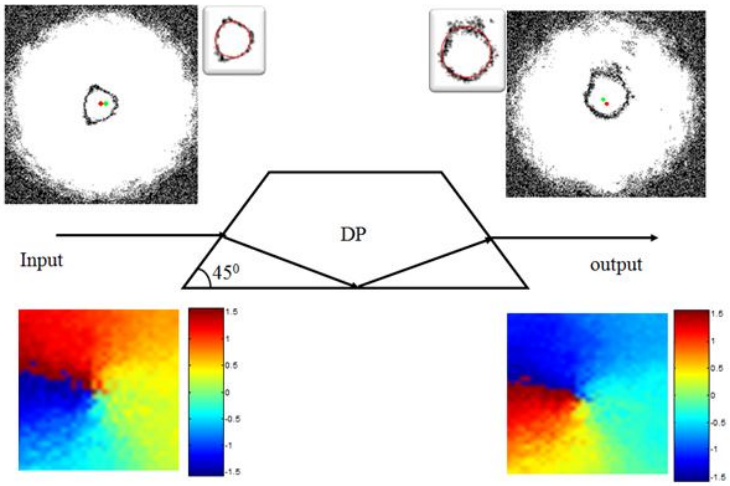

Figure 5.8: Input and output beam S-line, C-point (green dot), geometric center of the beam (red dot) and the orientation map of the polarization ellipse around the C-point. Inset shows the circle drawn around the S-contour to compare the area enclosed by the S-contour for input and output beams.

Further, we confirmed that the S-line shape deformation by looking into the amplitude variation of the beam before and after the DP by taking the amplitude contours of the two beams with same intensity values. The intensity contours of the two beams are as shown in Fig.5.9. The same intensity contours of the two beams are as shown in inset of the beams, from which it is clear that the same intensity contours of the input and output beams of the DP are different in size and shape due to the amplitude leakage which is due to the polarization leakage.

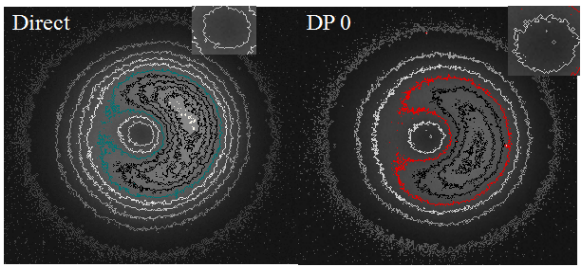

Figure 5.9: Intensity contours of the input and the output beam after the DP oriented at 0°. Inset shows the same intensity contours of the input and output beams.

Next, we measured the shape of the S-contour, C-point and orientation of ellipse around the C-point for every 22.5° rotation of the DP (upto180°) to study the effect of polarization leakage of the DP for different input beam polarization characteristics. The measured S-contour, C-points and orientation map of polarization ellipse around the C-point for different angles of the DP with 45° interval is shown in Figs 5.10 and 5.11. Form the Fig 5.10, it is clear that shape of the S-contour changes for different angles of the DP and the area enclosed by the S-contour is more for the DP at 22.5° (7.3 pixel^2) and less for the DP at 112.5° (3.4 pixel^2) which is similar to the RDE measurements of analyzer rotation behavior for different angles of the DP. The DP oriented at 22.5° shows a bigger circle and the DP at 112.5° shows a smaller circle, on the periphery of the DP rotation trajectory (Fig.5.3).

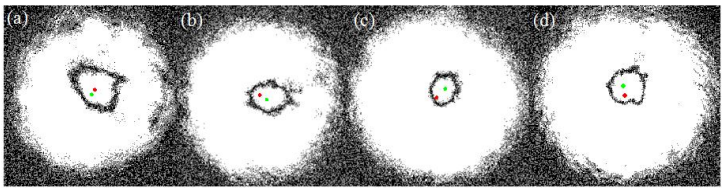

Figure 5.10: S-line and C-point of the output beam for DP at different angles: (a) 22.5° (b) 67.5° (c) 112.5° (d) 157.5°, C-point (green dot) and geometric center (red dot) are indicated in the figure.

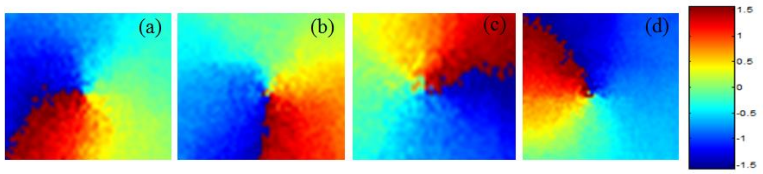

Figure 5.11: Orientation of polarization ellipse around the C-point in the output beam for DP at different angles: (a) 22.5° (b) 67.5° (c) 112.5° (d) 157.5°

Hence the polarization leakage of the DP is different at different angles of the DP. It is also important to note that the C-point rotates around the geometric center of the beam for the DP rotation (as shown in Fig.5.10), due to the phase accumulation from the DP and the image rotation property of the DP which are confirmed further by the orientation of the polarization ellipse around the C-point is shown Fig.5.11. In these hue plots the minimum orientation angle (blue colour '$-\pi/2$') changes its position depending on the orientation angle of the DP. The CCW rotation of DP results in the polarization ellipse rotating in the CCW direction and completes one full circle for the DP rotation from 0° to180°.

5.3 Summary

To summarize the results presented in this Chapter, we have demonstrated the RDE in the vector-vortex beam generated from a stationary step-index two mode fiber due to the selective excitation of polarization singularities for different cases. If the coherently superposed vortex beam has the same sign of handedness and topological charge, one complete rotation of the analyzer (Ω) with respect to a stationary screen results in the ZIP rotating by -2Ω whereas for a vortex beam with different signs of handedness and topological charge the ZIP rotates by +2Ω. For the beam after passing through the DP oriented at different angles, the RDE changes from -2 Ω to the +2Ω due to the change in the topological charge of the vortex mode caused by the DP.

Using isolated polarization singularities as a marker we have qualitatively characterized the polarization leakage and the accumulated phase from the DP by tracking the shape of the S-line, C-point position with respect to geometric center and the rotation of the polarization ellipse around the C-point. The polarization singularities appears to be one of the best tools to measure the phase and amplitude deformations due to optical components by characterizing shape of the S-line and the orientation of polarization ellipses around the C-point before and after the optical component. These will provide substantial quantitative information about the polarization leakage and the unknown phase accumulated from the optical component and optical materials in linear and possibly nonlinear optical measurements.

Chapter 6

Summary and Future Directions

In this thesis, we investigated the generation of different vector-vortex (VV) beams using two-mode step index optical fiber. The variety of VV beams generated by coupling Gaussian input beam with tilt and off-set to the fiber and the polarization singularities in the output beam are characterized by different methods. In chapter 1. The mathematical background necessary to understand excitation of vector and vortex modes in the optical fiber and also the different representation of vector modes interms of LP and vortex modes are introduced for a two-mode fiber. The formation of vector singularities are introduced in the vector modes via the propagation of vector LP mode in the fiber to better understand the results presented in this thesis.

For a short length of the fiber the beams generated and coupled out of the fiber have both the vector and vortex nature as discussed in Chapter 2. The vector nature of the beam is identified by rotating the analyzer at the output and the vortex nature is identified by constructing a two beam interferometer. The launch angle and the input polarization play a crucial role in the generation of VV beams for a given length of the fiber. The length dependence can be measured using the mathematical expressions developed in the first chapter. The angle of cone of light entering into the fiber with respect to its axis plays a crucial role on the topological charge and on the presence of the partial vortices in the output beam. The beams generated using this method are elliptically polarized across the beam cross section and the orientation of the ellipse major axis changes across the beam. These beams also possess polarization singularities when orthogonal polarized modes are excited simultaneously.

It is realized that the analyzer rotation and two-beam interference alone cannot give the complete information about the beam characteristics and the presence of polarization singularities. Different techniques are developed to identify the polarization singularities across the beam cross section and to measure the presence of partial vortices in the output beam elaborated in Chapter 3. The polarization interferometric technique and complex Stokes parameter method are described to identify the polarization singularities and to measure the presence of partial vortices in the output vector-vortex beams. From the measured complex Stokes parameters the point-wise state of polarization (SOP) map is constructed which gives the polarization behavior at each and every point in the beam cross section. Using these techniques the evolution of polarization singularities in the vector beams are studied as a function of wavelength using a continuously tunable Ti:Sapphire laser. The output beam has cyclic behavior in polarization, where the output HG_{10} mode is transformed from the right elliptical to left elliptical beam whereas the LG_{01} mode is transformed from the left elliptical beam to the half right and half left elliptical polarization through the polarization singularities. The presence of the two partial vortices in the LG_{01} output beam is identified by complex Stokes parameter method and their topological charges identified by the interferometric method. The formation of two C-points with same topological charge in the output of LG_{01} beam is understood by the perturbation of two partial vortices ((1 -1) and (-1 1)) with each other and the sign of the topological charges of the C-points are confirmed by the sign rule. The output beam intensity plot and polarization behavior on the Poincare sphere further confirm the cyclic behavior of modes due to input wavelength tunning.

The isolated or single C-point is formed due to the coherent superposition of orthogonal circular polarized Gaussian beam and vortex beam. The condition

for forming isolated C-point is achieved by selectively exciting the coherent superposition of orthogonal circularly polarized fundamental and vortex modes by coupling circularly polarized Gaussian beam and selecting the appropriate fiber length. The presence of C-point and the L-contour surrounding it are measured by two different techniques and it is concluded that the complex Stokes parameter method is more advantageous than the interferometric method. The switching between the C-point with different topological charges are achieved by changing the input launch angle and the input polarization from right to left or vice versa for each input launch angle, presented in Chapter 4.

In Chapter 5, we presented two applications of isolated polarization singularities: (i) rotation Doppler-effect (RDE) and (ii) characterization of Dove prism. The RDE in polarization singular beams is due to the time dependent phase of the two combined beams. The RDE is measured by passing the output beam through a rotating analyzer with respect to a stationary screen. For one complete rotation of the analyzer the output beam rotates twice along with the analyzer or opposite of the analyzer rotation direction depending upon the modes excited in fiber. The polarization leakage and the phase accumulation in the DP on the output beam are measured by tracking the area enclosed by the L-contour and the orientation of polarization ellipses around the C-point before and after the DP at different angles. The measurements shows significant changes in the L-contour and the hue plot of polarization ellipses around the C-point for DP at different angles confirms the polarization leakage and phase accumulation from the DP at different angles.

The beams generated and studied in a this thesis have application in a wide variety of basic and applied research areas due to the vector and vortex nature of

the beams and their sensitivity to the external perturbations which can be measured precisely by looking at the polarization singularities in the output beam.

Future directions of the work:

In order to understand the output beam behavior generated using TMF reported in this thesis, to make it suitable for applications including trapping, micromanipulation and as novel microscopy tool, the output beam should be characterized completely interms of its different parameters such as phase, polarization, coherence and the Poynting vector distribution (or the transverse energy flow). But the phase and polarization are interdependent quantities in the case of vector-vortex beams generated using fibers (spin-orbit interaction) due to which the contribution from the individual quantities are much difficult to separate experimentally. The recent analysis on the transverse energy flow in light beams shows that even in the paraxial approximation the spin angular momentum can induce orbital rotation of trapped particles [14, 15]. The VV beams reported in this thesis, with their ability to switch between the different topological charges of the C-point can be used in a particle trap experiments to have a rich variety of particle motion and manipulation due to orbital motion from the phase and polarization and their corresponding gradients [136, 137].

Recently other methods of generating VV beams with embedded polarization singularities are reported by using subwavelength gratings [138, 139], q-plates [20, 140], polarization sensitive elements [141], and the interference of two orthogonally polarized LG beams in free space [142]. The tight focusing properties of these beams are studied theoretically and experimentally which will increase the variety of applications of the VV beams [143, 144]. Such beams will also enable applications involving generation of phase and polarization entangled photons, suitable for quantum information applications.

Appendices

Appendix 1

List of operators in Cartesian and cylindrical polar coordinates:

The scalar function 'ψ' and the vector function '**A**' depend on the Cartesian and cylindrical polar coordinates (x, y, z), (r, φ, z). If $\hat{\mathbf{x}}, \hat{\mathbf{y}}, \hat{\mathbf{z}}$ and $\hat{\mathbf{r}}, \hat{\varphi}, \hat{\mathbf{z}}$ are the unit vectors in Cartesian and cylindrical polar coordinates then the operators in Cartesian and cylindrical coordinates are defined as

Cartesian coordinates

Gradient: $\nabla\psi(x, y, z) = \nabla_t\psi + \hat{\mathbf{z}}\dfrac{\partial\psi}{\partial z} = \hat{\mathbf{x}}\dfrac{\partial\psi}{\partial x} + \hat{\mathbf{y}}\dfrac{\partial\psi}{\partial y} + \hat{\mathbf{z}}\dfrac{\partial\psi}{\partial z}$

Divergence: $\nabla \cdot \mathbf{A}(x, y, z) = \nabla_t \cdot \mathbf{A}_t + \dfrac{\partial \mathbf{A}_z}{\partial z} = \dfrac{\partial \mathbf{A}_x}{\partial x} + \dfrac{\partial \mathbf{A}_y}{\partial y} + \dfrac{\partial \mathbf{A}_z}{\partial z}$

Curl: $\nabla \times \mathbf{A}(x, y, z) = \begin{pmatrix} \hat{\mathbf{x}} & \hat{\mathbf{y}} & \hat{\mathbf{z}} \\ \partial/\partial x & \partial/\partial y & \partial/\partial z \\ \mathbf{A}_x & \mathbf{A}_y & \mathbf{A}_z \end{pmatrix}$ and $\nabla_t \times \mathbf{A}_t = \hat{\mathbf{z}}\left\{\dfrac{\partial \mathbf{A}_y}{\partial x} - \dfrac{\partial \mathbf{A}_x}{\partial y}\right\}$

Scalar Laplacian operator ∇^2: $\nabla^2\psi(x, y, z) = \nabla_t^2\psi + \dfrac{\partial^2\psi}{\partial z^2} = \dfrac{\partial^2\psi}{\partial x^2} + \dfrac{\partial^2\psi}{\partial y^2} + \dfrac{\partial^2\psi}{\partial z^2}$

Vector Laplacian operator ∇^2: $\nabla^2\mathbf{A}(x, y, z) = \hat{\mathbf{x}}(\nabla^2\mathbf{A}_x) + \hat{\mathbf{y}}(\nabla^2\mathbf{A}_y) + \hat{\mathbf{z}}(\nabla^2\mathbf{A}_z)$

Where

$$\nabla^2 = \frac{\partial^2}{\partial x^2} + \frac{\partial^2}{\partial y^2} + \frac{\partial^2}{\partial z^2}$$

Cylindrical polar coordinates

Gradient: $\nabla\psi(r,\varphi,z) = \nabla_t\psi + \hat{\mathbf{z}}\frac{\partial\psi}{\partial z} = \hat{\mathbf{r}}\frac{\partial\psi}{\partial x} + \hat{\varphi}\frac{\partial\psi}{\partial y} + \hat{\mathbf{z}}\frac{\partial\psi}{\partial z}$

Divergence: $\nabla\cdot\mathbf{A}(r,\varphi,z) = \nabla_t\cdot\mathbf{A}_t + \frac{\partial\mathbf{A}_z}{\partial z} = \frac{1}{r}\frac{\partial(r\mathbf{A}_r)}{\partial r} + \frac{1}{r}\frac{\partial\mathbf{A}_\varphi}{\partial y} + \frac{\partial\mathbf{A}_z}{\partial z}$

Curl: $\nabla\times\mathbf{A}(r,\varphi,z) = \begin{pmatrix} \hat{\mathbf{r}} & \hat{\varphi} & \hat{\mathbf{z}} \\ \partial/\partial r & \partial/\partial\varphi & \partial/\partial z \\ \mathbf{A}_r & r\mathbf{A}_\varphi & \mathbf{A}_z \end{pmatrix}$ and $\nabla_t\times\mathbf{A}_t = \frac{\hat{\mathbf{z}}}{r}\left\{\frac{\partial(r\mathbf{A}_\varphi)}{\partial r} - \frac{\partial\mathbf{A}_r}{\partial\varphi}\right\}$

Scalar Laplacian operator ∇^2 :

$$\nabla^2\psi(r,\varphi,z) = \nabla_t^2\psi + \frac{\partial^2\psi}{\partial z^2} = \frac{\partial^2\psi}{\partial r^2} + \frac{1}{r}\frac{\partial\psi}{\partial r} + \frac{1}{r^2}\frac{\partial^2\psi}{\partial\varphi^2} + \frac{\partial^2\psi}{\partial z^2}$$

Vector Laplacian operator:

$$\nabla^2\mathbf{A}(r,\varphi,z) = \hat{\mathbf{r}}\left\{\nabla^2\mathbf{A}_r - \frac{2}{r^2}\frac{\partial\mathbf{A}_\varphi}{\partial\varphi} - \frac{\mathbf{A}_r}{r^2}\right\} + \hat{\varphi}\left\{\nabla^2\mathbf{A}_\varphi + \frac{2}{r^2}\frac{\partial\mathbf{A}_r}{\partial\varphi} - \frac{\mathbf{A}_\varphi}{r^2}\right\} + \hat{\mathbf{z}}(\nabla^2\mathbf{A}_z)\ \mathrm{W}$$

here $\nabla^2 = \frac{\partial^2}{\partial r^2} + \frac{1}{r}\frac{\partial}{\partial r} + \frac{1}{r^2}\frac{\partial^2}{\partial\varphi^2} + \frac{\partial^2}{\partial z^2}$

Relation between the coordinates and unit vectors:

$x = r\cos\varphi$, $y = r\sin\varphi$; $r = \left(x^2 + y^2\right)^{1/2}$, $\varphi = \tan^{-1}(y/x)$

$\hat{\mathbf{r}} = \hat{\mathbf{x}}\cos\varphi + \hat{\mathbf{y}}\sin\varphi$; $\hat{\varphi} = -\hat{\mathbf{x}}\sin\varphi + \hat{\mathbf{y}}\cos\varphi$,

$\hat{\mathbf{x}} = \hat{\mathbf{r}}\cos\varphi - \hat{\varphi}\sin\varphi$; $\hat{\mathbf{y}} = \hat{\mathbf{r}}\sin\varphi + \hat{\varphi}\cos\varphi$,

$\hat{\mathbf{r}}\times\hat{\varphi} = \hat{\mathbf{z}}$; $\hat{\mathbf{z}}\times\hat{\mathbf{r}} = \hat{\varphi}$

From the above relations

$\frac{\partial\hat{\mathbf{r}}}{\partial r} = 0$, $\frac{\partial\hat{\mathbf{r}}}{\partial\varphi} = \hat{\varphi}$; $\frac{\partial\hat{\varphi}}{\partial r} = 0$; $\frac{\partial\hat{\varphi}}{\partial\varphi} = -\hat{\mathbf{r}}$

Appendix 2

Formation of LP modes:

The LP_{11}^{ex} mode is formed due to beating between the HE_{21}^{e} and TM_{01} vector modes. The electric field of the two vector modes are

$$\mathbf{e}_{\mathbf{HE}_{21}^{ev}} = F_1(R)\{\hat{\mathbf{x}}\cos\varphi - \hat{\mathbf{y}}\sin\varphi\}\exp(i\beta_1 z)$$

$$\mathbf{e}_{\mathbf{TM}_{01}} = F_1(R)\{\hat{\mathbf{x}}\cos\varphi + \hat{\mathbf{y}}\sin\varphi\}\exp(i\beta_2 z)$$

where $\hat{\mathbf{x}}$, $\hat{\mathbf{y}}$ are the unit vectors, $F_1(R)$ is the radial distribution of the field and β_1, β_2 are the vector propagation constants of the HE_{21}^{e} and TM_{01} modes respectively. The vector and scalar propagation constants of the fiber modes are related by

$\beta_1 = \tilde{\beta} + \delta\beta_1$, $\beta_2 = \tilde{\beta} + \delta\beta_2$,

where $\tilde{\beta}$ is the scalar propagation constant and $\delta\beta_i$ is the polarization correction to the i^{th} mode.

The electric field of the vector LP_{11}^{ex} mode is sum of the two vector modes and is written as

$$LP_{11}^{ex} = \left(\{\hat{\mathbf{x}}\cos\varphi - \hat{\mathbf{y}}\sin\varphi\}\exp(i\delta\beta_1 z) + \{\hat{\mathbf{x}}\cos\varphi + \hat{\mathbf{y}}\sin\varphi\}\exp(i\delta\beta_2 z)\right) F_1(R)\exp(i\tilde{\beta}z)$$

$$LP_{11}^{ex} = \left\{\hat{\mathbf{x}}\cos\varphi[e^{i\delta\beta_1 z} + e^{i\delta\beta_2 z}] + \hat{\mathbf{y}}\sin\varphi[e^{i\delta\beta_2 z} - e^{i\delta\beta_1 z}]\right\} F_1(R)\exp(i\tilde{\beta}z)$$

$$LP_{11}^{ex} = \left\{\hat{\mathbf{x}}\cos\varphi[e^{-i(\delta\beta_2-\delta\beta_1)z/2)} + e^{i(\delta\beta_2-\delta\beta_1)z/2}] + \hat{\mathbf{y}}\sin\varphi[e^{i(\delta\beta_2-\delta\beta_1)z/2} - e^{-i(\delta\beta_2-\delta\beta_1)z/2)}]\right\}\times$$

$$e^{i(\delta\beta_1+\delta\beta_2)z/2} F_1(R)\exp(i\tilde{\beta}z)$$

$$LP_{11}^{ex} = \{\hat{\mathbf{x}}\cos(\varphi)\cos(\delta\beta_{21}z) + i\hat{\mathbf{y}}\sin(\varphi)\sin(\delta\beta_{21}z)\}F_1(R)\exp(i\beta' z)$$

where $\delta\beta_{21} = (\delta\beta_2 - \delta\beta_1)/2$ is half the correction between the polarization correction terms of HE_{21}^{e} and TM_{01}vector modes. $\beta' = \tilde{\beta} + (\delta\beta_1 + \delta\beta_2)/2$ is the vector propagation constant of LP_{11}^{ex} mode.

Similarly the other LP modes are written interms of the vector propagation constants:

$$LP_{11}^{oy} = HE_{21}^{e} - TM_{01} = \begin{pmatrix} -i\cos\varphi\sin\delta\beta_{21}z \\ -\sin\phi\cos\delta\beta_{21}z \end{pmatrix} F_1(R)\exp(i\beta' z)$$

$$LP_{11}^{ox} = HE_{21}^{o} + TE_{01} = \begin{pmatrix} \sin\varphi\cos\delta\beta_{43}z \\ -i\cos\varphi\sin\delta\beta_{43}z \end{pmatrix} F_1(R)\exp(i\beta' z)$$

$$LP_{11}^{oy} = HE_{21}^{od} - TE_{01} = \begin{pmatrix} -i\sin\varphi\sin\delta\beta_{43}z \\ \cos\varphi\cos\delta\beta_{43}z \end{pmatrix} F_1(R)\exp(i\beta' z)$$

Appendix 3

The electric field due to coherent superposition of orthogonal circularly polarized Gaussian beam and vortex beam is written as

$$\mathbf{E}_t = (\hat{\mathbf{x}} + i\sigma_l\hat{\mathbf{y}})a\exp(-R^2) + (\hat{\mathbf{x}} + i\sigma_2\hat{\mathbf{y}})R\exp(-R^2 + i\sigma_2\varphi) \qquad \text{(A3.1)}$$

The beam passing through the rotating analyzer gives the different projection of the field. The field projections in the new coordinate for $(\hat{\mathbf{x}} + i\sigma_l\hat{\mathbf{y}})$ is

$$\begin{pmatrix}\hat{\mathbf{X}}\\ \hat{\mathbf{Y}}\end{pmatrix}=\begin{pmatrix}\cos\theta & \sin\theta\\ -\sin\theta & \cos\theta\end{pmatrix}\begin{pmatrix}1\\ i\sigma_1\end{pmatrix} \tag{A3.2}$$

$(\cos\theta+i\sigma_1\sin\theta)\hat{\mathbf{X}}+(-\sin\theta+i\sigma_1\cos\theta)\hat{\mathbf{Y}}$ since σ_1 = ±1, writing σ_1 in the numerator or in the denominator will not effect the equation, then the above equation becomes

$$(\cos\theta+i\sigma_1\sin\theta)\hat{\mathbf{X}}+i\sigma_1(\cos\theta+i\sigma_1\sin\theta)\hat{\mathbf{Y}} \tag{A3.3}$$

$$(\hat{\mathbf{X}}+i\sigma_1\hat{\mathbf{Y}})\exp(i\sigma_1\theta) \tag{A3.4}$$

Similarly for $(\hat{\mathbf{x}}+i\sigma_2\hat{\mathbf{y}})$, it is, $(\hat{\mathbf{X}}+i\sigma_2\hat{\mathbf{Y}})\exp(i\sigma_2\theta)$ (A3.5)

The projected field in the new coordinates is (eqns. (A3.4 and A3.5))

$$\mathbf{E}_\theta=(\hat{\mathbf{X}}+i\sigma_1\hat{\mathbf{Y}})a\exp(-R^2+i\sigma_1\theta)+(\hat{\mathbf{X}}+i\sigma_2\hat{\mathbf{Y}})\,Re\,xp(-R^2+i\sigma_2\varphi+i\sigma_2\theta)$$

At the singular point the real and imaginary components of the field is zero. By equating the real and imaginary components of the field to zero the above equation becomes

$$0=a\exp(-R^2+i\sigma_1\theta)+R\exp(-R^2+i\sigma_2\varphi+i\sigma_2\theta)$$

$$0=a+Re\,xp(i(\sigma_2\varphi+\sigma_2\theta-\sigma_1\theta))$$

List of publications related to thesis

Journals

[1] N.K. Viswanathan and V.V.G. Krishna Inavalli, "Generation of optical vector beams using a two mode optical fiber," Opt. Lett. **34**, 1189-1191 (2009)

[2] V.V.G. Krishna Inavalli and N.K. Viswanathan, "Switchable vector vortex beam generation using an optical fiber," Opt. Commun. **283**,861-864 (2010)

[3] V.V.G. Krishna Inavalli and N.K. Viswanathan, "Rotational Doppler-effect due to selective excitation of vector-vortex field in optical fiber," Opt. Exp. **19**, 448-457 (2011)

[4] V.V.G. Krishna Inavalli, P. Vijay and N.K. Viswanathan, "Wavelength dependence of the polarization singularities in a two mode optical fiber," Int. J. Opt. **2012**, 358093 (2011)

[5] Y.V. Jayasurya, V.V.G. Krishna Inavalli and N.K. Viswanathan, "Polarization singularities in the two-mode optical fiber output," Appl. Opt. **50**, E131-E137 (2011)

Conferences

[1] V.V.G. Krishna Inavalli and N.K. Viswanathan, "Generation of switchble vector beams with two-mode optical fiber and its characteristics," International Conference on Optics and Photonics (ICOP), Chandigarh (2009)

[2] N.K. Viswanathan and V.V.G. Krishna Inavalli, " Rotational frequency shift in cylindrical vector beams due to skew rays in few-mode optical fibers," Proc. SPIE **7613**, 761307-9 (2010)

[3] V.V.G. Krishna Inavalli and N.K. Viswanathan, “Measurement of angular Doppler effect of rotating light beam,” India-Singapore Joint Physics Symposium, Hyderabad (2010)

[4] V.V.G. Krishna Inavalli, Y.V. Jayasurya and N.K. Viswanathan, “Measurement of polarization singularities in the output of two-mode optical fiber,” Photonics-2010, Guwahati (2010)

[5] V.V.G. Krishna Inavalli, P. Vijay and N.K. Viswanathan, “Polarization singularities due to cyclic changes in the vector modes of a two-modes of a two mode fiber,” Work shop on Singular Optics and its Applications, ICTP-Italy (2011)

[6] V.V.G. Krishna Inavalli and N.K. Viswanathan, “Singularities in wave optics,” OSA Student-Interactions meeting (SI-2012), Hyderabad (2012)

References

[1] M.V. Berry, "*Singularities in waves and rays*," in R.Balian, M. Kleman, and J.P. Poirier,editors, Les Houches Session XXV-Physics of Defects (North-Holland, 1981)

[2] J.F. Nye, "*Natural focusing and fine structure of light: Caustics and wave dislocations*," Bristol, IOP publishing (1999)

[3] M.S. Soskin and M.V. Vasnetsov, "Singular optics," in Prog. in Optics, E. Wolf, ed. (Elsevier, Amsterdam, (2001)) **42**, Chap. 4

[4] M.R. Dennis, K.O'Holleran and M.J. Padgett, "Singular optics: Optical vortices and polarization singularities," in Prog. in Optics, E. Wolf, ed. (Elsevier, Amsterdam, (2009)) **53,** 293-363

[5] J.F. Nye and M.V. Berry, "Dislocations in wave trains," Proc. R. Soc. London. A. **336**,165-190 (1974)

[6] J.F. Nye, "Polarization effects in the diffraction of electromagnetic waves: the role of disclinations," Proc. R. Soc. London. A. **387**, 105-132 (1983)

[7] J.F. Nye, "Lines of circular polarization in electromagnetic wave fields," Proc. R. Soc. London. A. **389**, 279-290 (1983).

[8] J.V. Hajnal, "Singularities in the transverse fields of electromagnetic waves. I. Theory," Proc. R. Soc. London Ser. A. **414**, 433-446 (1987)

[9] J.V. Hajnal, "Singularities in the transverse fields of electromagnetic waves. II. Observations on the electric field," Proc. R. Soc. London Ser. A **414**, 447-468 (1987)

[10] J.F. Nye and J.V. Hajnal, "The wave structure of monochromatic electromagnetic radiation," Proc. R. Soc. London. A. **409**, 21-36 (1987)

[11] J.V. Hajnal, "Observations of singularities in the electric and magnetic fields of freely propagating microwaves," Proc. R. Soc. London Ser. A. **430**, 413 – 421 (1990)

[12] L. Allen, M.W. Beijersbergen, R.J.C. Spreeuw and J.P. Woerdman, "Orbital angular momentum of light and transformation of Laguerre Gaussian laser modes," Phys. Rev. A **45,** 8185 (1992)

[13] D.L. Andrews, "*Structured light and its applications: An introduction to phase-structured beams and nanoscale optical forces*," Academic Press-Elsevier, Burlington (2008)

[14] J.P. Torres and L. Torner, "*Twisted photons: Applications of light with orbital angular momentum*," Wiley-Vch Verlag, John Wiley and Sons, Weinheim (2011)

[15] A.Ya. Bekshaev and M.S. Soskin, "Transverse energy flows in vectorial fields of paraxial beams with singularities, Opt. Commun. **271**, 332-348 (2007)

[16] M.A. Yao and M.J. Padgett, "Orbital angular momentum: origins, behavior and applications," Adv. Opt. and Photon. **3**, 161–204 (2011)

[17] M.R. Dennis, K.O. Holleran and M.J. Padgett, "Singular optics: Optical vortices and polarization singularities," Prog. in Opt. **53,** 293-363 (2009) Ed. E. Wolf

[18] L. Allen, M.J. Padgett and M. Babiker, "The orbital angular momentum of light," Prog. in Opt. **39,** 291-372 (1999) Ed**.** E. Wolf.

[19] Q. Zhan, "Cylindrical vector beams: from mathematical concepts to applications," Adv. Opt. and Photon. **1**, 1-57 (2009)

[20] E. Hasman, G. Biener, A. Niv, and V. Kleiner "Space-variant polarization manipulation," Prog. in Opt. **47,** 215-289 (2005) Ed. E. Wolf.

[21] E. Snitzer, "Cylindrical dielectric waveguide modes," J .Opt. Soc .Am. **51**, 491-498 (1996)

[22] E. Snitzer, "Observed dielectric waveguide modes in the visible spectrum," J. Opt. Soc .Am. **51**, 499-505 (1996)

[23] A.W. Snyder and J.D. Love, "*Optical waveguide theory*" Chapman and Hall (1983)

[24] A.V. Volyar and T.A. Fadeeva, "Optics of singularities of the field of a low-mode fiber: II. Optical vortices," Opt. and Spectros. **85**, 272-280 (1998)

[25] A.V. Volyar, "Fiber singular optics," Ukr. J. of Phys. Opt. **3**, 69-96 (2002)

[26] C.N. Alexeyev, A.V. Volyar and M.A. Yavorsky, "Fiber optical vortices," In Lasers, Optics and Electro-Optics Research, L. I.Chen, Ed., Nova Science Publishers, (2007)

[27] N.B. Baranova**,** B.Ya. Zel'dovich, and A.V Mamaeyev, "Dislocations of the wavefront of a speckle-inhomogeneous field (theory and experiment)," JETP. Lett. **33,** 195-199 (1981)

[28] M.Ya. Darsh, B.Ya. Zel'dovich, I.V. Kataeyevskaya and N.D Kundicova, "Formation of single wavefront dislocation," JETP, **105**, 1464-1472 (1995)

[29] A.V. Volyar, T.A. Fadeyeva, "Vortex nature of optical fiber modes. I. Structure of the natural modes," Techn. Phys. Lett. **22,** 320-332 (1996)

[30] A.V. Volyar, T.A. Fadeyeva, "Vortex nature of optical fiber modes. II. Distribution of optical vortices," Techn. Phys. Lett. **22,** 333-335 (1996)

[31] T. Grosjean, D. Courjon and M. Spajer, "An all-fiber device for generating radially and other polarized light beams," Opt. Commun. **203**, 1-5 (2002)

[32] T. Grosjean, A. Sabac and D. Courjon, “A versatile and stable device allowing the efficient generation of beams with radial, azimuthal or hybrid polarizations,” Opt. Commun. **252**, 12-21 (2005)

[33] G. Volpe and D. Petrov, “Generation of cylindrical vector beams with few-mode fiber excited by Laguerre-Gaussian beams,” Opt.Commun. **237**, 89-95 (2004)

[34] J. A. Stratton, “*Electromagnetic theory*,” McGraw-Hill, New York (1941)

[35] M. Born and E.W. Wolf, “*Principles of optics*,” 6th edition, Cambridge University Press, UK (1980)

[36] V.S. Liberman and B.Ya. Zel’dovich, “Spin-orbit interaction of a photon in an inhomogeneous medium,” Phys. Rev. A. **45,** 5199-5207 (1992)

[37] A.Yu. Savchencko and B.Ya. Zel'dovich, “Wave propagation in a guiding structure: one step beyond the paraxial approximation,” JOSA. B. **13**, 273-281 (1996)

[38] C.N. Alexeyev, Yu.A. Fridman and A.N. Alexeyev, “Angular momentum and spin–orbit interaction in weakly guiding fibers,” Ukr. J. Phys. **44,** 74-81 (1999)

[39] V.S. Liberman and B.Ya. Zel’dovich, “Birefringence by a smoothly inhomogeneous locally isotropic medium,” Phys. Rev. E. **49**, 2389-2396 (1994)

[40] A.Yu. Savchenko and B.Ya. Zel’dovich, “Birefringence by a smoothly inhomogeneous locally isotropic medium: Three-dimensional case,” Phys. Rev. E. **50**, 2287-2292 (1994)

[41] A.V. Dooghin, B.Ya. Zel’dovich, N.D. Kudnikova, and V.S. Liberman, “ Optical Magnus effect,” Phys. Rev. A. **45**, 8204-8208 (1992)

[42] J. Bures, "*Guided optics-Optical Fibers and all fiber components,*" Wiley-VCH, Berlin (2009)

[43] K. Thyagarajan, A.K. Ghatak and A. Sharma, "Vector modes of an optical fiber in the weakly guiding approximation," IEEE J. Lightwave Technol., **7,** 51 – 53 (1989)

[44] N.S. Kapany, " *Fiber optics: Principles and applications,*" Academic press, New York, (1967)

[45] D. Gloge, "Weakly guiding fibers," Appl. Opt, **10**, 2252-2258 (1971)

[46] A.W. Snyder, "Asymptotic expressions for eigenfunctions and eigrnvalues of dielectric or optical waveguides," I.E.E.E. Trans. Microwave Theory Tech, **17** 1130-1138 (1969)

[47] E. Hecht, "*Optics,*"4th edition, McGraw-Hill, New York (1980)

[48] C. N. Alexeyev, A.V. Volyar and T. A. Fadeeva, " Spin-orbit interaction and evolution of optical eddies in perturbed weakly directing optical fibers," Opt. and Spectros, **93**, 588-297 (2002)

[49] A. S. Davydov, "*Quantum mechanics,*" Pergamon, Oxford (1976)

[50] A.V. Volyar, V. Z. Zhilatis, and V.G. Shvedov, "Spin–orbit interaction in the field of an optical vortex of a few-mode fiber," Tech. Phys. Lett. **24**, 326-328 (1998)

[51] A.V. Volyar, V.Z. Zhilaitis and V.G. Shvedov, "Optical eddies in small-mode fibers: (ii). The spin-orbit interaction," Opt. and Spectros, **86**, 593-598 (1999)

[52] A.V. Volyar and T. A. Fadeeva, " Dynamics of dislocations and disclinations of the field of a few-order optical fiber: (i). Creation and annihilation of $C^{\pm}$ disclinations," Tech. Phys. Lett., **23**, 57-60 (1997)

[53] A.V. Volyar and T. A. Fadeeva, “Dynamics of dislocations and disclinations of the field of a few-order optical fiber: (ii). Pure type of singularities,” Tech. Phys. Lett., **23**, 91-93 (1997)

[54] A.V. Volyar, T.A. Fadeeva and K.M. Reshitova,“ Dynamics of dislocations and disclinations of the field of a few-order optical fiber:(iii). circularly polarized CP_{11} modes and L disclinations,” Tech. Phys. Lett., **23**, 175-177 (1997)

[55] A.V. Volyar, T.A. Fadeeva and K.M. Reshitova, “Dynamics of dislocations and disclinations of the field of a few-order optical fiber: (iv). Formation of an optical vortex,” Tech. Phys. Lett., **23**, 198-200 (1997)

[56] A.V. Volyar and T.A. Fadeeva, “Optics of singularities of the field of a low-mode fiber: (i). Circular disclinations,” Opt. and Spectros, **85**, 264-271 (1998)

[57] D. Pohl, “Operation of a Ruby laser in the purely transverse electric mode TE_{01},” Appl. Phys. Lett. **20**, 266–267 (1972)

[58] M. E. Marhic and E. Garmire, “Low-order TE_{0q} operation of a CO2 laser for transmission through circular metallic waveguides,” Appl. Phys. Lett. **38**, 743–745 (1981)

[59] T. Erdogan, O. King, G. W. Wicks, D. G. Hall, E. Anderson, and M. J.Rooks, “Circularly symmetric operation of a concentric-circle-grating, surface-emitting, AlGaAs/GaAs quantum-well semiconductor laser,” Appl. Phys. Lett. **60**, 1921–1923 (1992)

[60] K. Yonezawa, Y. Kozawa, and S. Sato, “Generation of a radially polarized laser beam by use of the birefringence of a *c*-cut Nd:YVO4 crystal,” Opt. Lett. **31**, 2151–2153 (2006)

[61] G. Machavariani, Y. Lumer, I. Moshe, A. Meir, S. Jackel, and N. Davidson, "Birefringence-induced bifocusing for selection of radially or azimuthally polarized laser modes," Appl. Opt. **46**, 3304–3310 (2007)

[62] J. F. Bisson, J. Li, K. Ueda, and Y. Senatsky, "Radially polarized ring and arc beams of a neodymium laser with an intra-cavity axicon," Opt. Exp. **14**, 3304–3311 (2006)

[63] C.-C. Shih, "Radial polarization laser resonator," U.S. patent **5**,359,622 (Oct. 25, 1994)

[64] Y. Kozawa and S. Sato, "Generation of a radially polarized laser beam by use of a conical Brewster prism," Opt. Lett. **30**, 3063–3065 (2005)

[65] M. A. Ahmed, A. Voss, M. M. Vogel, and T. Graf, "Multilayer polarizing grating mirror used for the generation of radial polarization in Yb:YAG thin-disk lasers," Opt. Lett. **32**, 3272 -3274 (2007)

[66] V. G. Niziev, R. S. Chang, and A. V. Nesterov, "Generation of inhomogeneously polarized laser beams by use of a Sagnac interferometer," Appl. Opt. **45**, 8393–8399 (2006)

[67] Q. Zhan and J. R. Leger, "Microellipsometer with radial symmetry," Appl.Opt. **41**, 4630–4637 (2002)

[68] Q. Zhan and J. R. Leger, "Interferometric measurement of Berry's phase in space-variant polarization manipulations," Opt. Commun. **213**, 241–245 (2002)

[69] M. R. Beversluis, L. Novotny, and S. J. Stranick, "Programmable vector point-spread function engineering," Opt. Exp. **14**, 2650–2656 (2006).

[70] C. Maurer, A. Jesacher, S. F. urhapter, S. Bernet and M. Ritsch-Marte, "Tailoring of arbitrary optical vector beams," New J. Phys. **9**, 1-20 (2007)

[71] G. Machavariani, Y. Lumer, I. Moshe, A. Meir, and S. Jackel, "Spatially-variable retardation plate for efficient generation of radiallyand azimuthally-polarized beams," Opt. Commun. **281**, 732–738 (2008)

[72] B. C. Lim, P. B. Phua, W. J. Lai, and M. H. Hong, "Fast switchable electro-optic radial polarization retarder," Opt. Lett. **33**, 950–952 (2008)

[73] T. Hirayama, Y. Kozawa, T. Nakamura, and S. Sato, "Generation of a cylindrically symmetric, polarized laser beam with narrow linewidth and fine tunability," Opt. Exp. **14**, 12839–12845 (2006).

[74] K. S. Youngworth and T. G. Brown, "Focusing of high numerical aperture cylindrical vector beams," Opt. Exp. **7**, 77–87 (2000).

[75] D.W. Diehl, R.W. Schoonover and T.D. Visser, "the structure of focused radially polarized fields," Opt. Exp. **14**, 3030–3038 (2006)

[76] R.W. Schoonover and T.D. Visser, "Polarization singularities of focused radially polarized field," Opt. Exp. **14**, 5733–5745 (2006)

[77] I.V. Basistiy, M.S. Soskin and M.V. Vasnetsov, "Optical wavefront dislocations and their properties," Opt. Commun., **119**, 604 – 612 (1995)

[78] G. Molina-Terriza, J. Recolons, J.P. Torres, L. Torner and E.M. Wright, "Observation of the dynamical inversion of the topological charge of an optical vortex," Phys. Rev. Lett., **87** 023902-05 (2001)

[79] Q. Zhan and J. R. Leger, "Microellipsometer with radial symmetry," Appl.Opt. **41**, 4630–4637 (2002)

[80] J.F. Nye, "Line singularities in the wave fields," Phil. Trans. R. Soc. London. A. **355**, 2065-2069 (1997)

[81] O.V. Angelsky, "*Optical correlation: Techniques and applications*," SPIE Press, USA (2007)

[82] O. Angelsky, A. Mokhun, I. Mokhun, and M. Soskin, “The relationship between topological charges of component vortices and polarization singularities,” Opt. Commun. **207**, 57-65 (2002)

[83] A. G. White, C. P. Smith, N. R. Heckenberg, H.Rubinsztein-Dunlop, R. McDuff, C. O. Weiss, and Chr.Tamm, ‘‘Interferometric measurements of phase singularities in the output of a visible laser,’’ J. Mod. Opt. **38**, 2531–2541 (1991)

[84] V. Yu. Bazhenov, M. V. Vasnetsov and M. S. Soskin, "Laser beams with screw dislocations in their wavefronts," JETP Lett. **52**, 429-431 (1990)

[85] N. R. Heckenberg, R. McDuff, C. P. Smith, H. Rubinsztein-Dunlop, and M. J. Wegener, ‘‘Laser beams with phase singularities,’’ Opt. Quantum Electron. **24**, S951–S962 (1992)

[86] O. Angelsky, R. Besaha, A. Mokhun, I. Mokhun, Sopin and M. Soskin, “ Singularities in vectoral fields” Proc. SPIE, **3904,** 40-55 (1999)

[87] O.V. Angelsky, I.I. Mokhun, A.I. Mokhun, and M.S. Soskin “Interferometric methods in diagnostics of polarization singularities,” Phys. Rev, E **65**, 036602-5 (2002)

[88] A.I. Mokhun and M.S. Soskin and “Elliptic critical points: C-points, a-lines, and the sign rule,” Opt. Lett, **27**, 995-997 (2002)

[89] I. Freund, “Poincare vortices,” Opt. Lett, **26**, 1996-1998 (2001)

[90] I. Freund, A.I. Mokhun, M.S. Soskin, O.V. Angelsky and I.I. Mokhun, “Stokes singularity relations,” Opt. Lett, **27**, 545-547 (2002)

[91] M.S. Soskin, V. Denisenko and I. Freund, “Optical polarization singularities and elliptic stationary points,” Opt. Lett., **28**, 1475 – 1477 (2003)

[92] D. Goldstein “*Polarized light*” Second edition (Marcel Dekker, Inc., 2003)

[93] D. Gloge, “Dispersions in weakly guiding fibers,” Appl.Opt, **10**, 2442-2445 (1971)

[94] D. Marcuse, “Interdependence of waveguide and material dispersion,” Appl. Opt, **18**, 2930-2932 (1979)

[95] B.J. Ainslies and C.R. Day, “A review of single-mode fibers with modified dispersion characteristics,” J. Lightwave Technol, **4**, 967-979 (1986)

[96] I. Kaminow, “Polarization in optical fibers,” IEEE- JQE, **17**, 15–22 (1981)

[97] T.I. Su and L. Wang, “A cutback method for measuring low linear fibre birefringence using an electro-optic modulator,” Opt. and Quantum Electron, **28**, 1395–1405 (1996).

[98] K. Kikuchi and T. Okoshi, “Wavelength-sweeping technique for measuring the beat length of linearly birefringent optical fibers,” Opt. Lett, **8**, 122–123, (1983)

[99] W. Eickhoff, Y. Yen, and R. Ulrich, “Wavelength dependence of birefringence in single-mode fiber,” Appl. Opt, **20**, 3428–3435 (1981)

[100] F. T. Martinez, D. Tentori, C. A. Diaz, and F. J. M. Jimenez, “Birefringence assessment of single-mode optical fibers,” Opt. Exp, **13**, 2556–2563 (2005)

[101] C. N. Alexeyev, A. V. Volyar, and M. A. Yavorsky, “Optical vortices in twisted optical fibres with torsional stress,” Journal of Optics A, **10**, 095007 (2008).

[102] T. A. Fadeeva and A. V. Volyar, “Vectorial topological dipole in output radiation of a fiber optical coupler,” Tech. Phys. Lett., **30**, 553–556, (2004).

[103] C.N.Alexeyev, E. V. Borshak, A. V. Volyar, andM. A. Yavorsky, “Angular momentum conservation and coupled vortex modes in twisted

optical fibres with torsional stress," Journal of Optics A, **11**, 094011 (2009).

[104] A. S. Jazi and J. C. McKeeman, "Synthesis of intensity patterns in few-mode optical fibers," J. of Lightwave. Techn., **9**,1047–1052, (1991)

[105] O. Hosten and P. Kwiat, "Observation of the spin Hall effect of light via weak measurements," Science **319**, 787 – 790, 2008

[106] S. Barreiro, J.W.R. Tabosa, H. Failache and A. Lezama, "Spectroscopic observation of the rotational Doppler effect," Phys. Rev. Lett., **97**, 113601 (2006)

[107] M.J. Padgettt, "Like a speeding watch," Nature **443**, 924 – 925 (2006)

[108] B.A. Garetz and S. Arnold, "Variable frequency shifting of circularly polarized laser radiation via a rotating half wave retardation plate," Opt. Commun., **31**, 1 – 3 (1979)

[109] B.A. Garetz, "Angular Doppler effect," J. Opt. Soc. Am. **71**, 609 – 611 (1981)

[110] I Bialynicki-Birula and Z Bialynicka-Birula, "Rotational frequency shift," Phys.Rev.Lett., **78**, 2539 – 2542 (1997)

[111] L. Allen, M. Babiker and W.L. Power, "Azimuthal Doppler shift in light beams with orbital angular momentum," Opt. Commun., **112**, 141 – 144 (1994)

[112] J. Courtial, D.A. Robertson, K. Dholakia, L. Allen and M.J. Padgett, "Rotational frequency shift of a light Beam," Phys. Rev. Lett. **81**, 4828 – 4830 (1998)

[113] J. Arlt, M. MacDonald, L. Paterson, W. Sibbett, K. Dholakia and K. Volke-Sepulveda, "Moving interference patters created using angular Doppler-effect," Opt. Exp. **10**, 844 – 852 (2002)

[114] I.V. Basistiy, A.Ya Bekshaev, M.V.Vasnetsov, V.V.Slyusar and M.S. Soskin, "Observation of the rotational Doppler effect for optical beams with helical wave front using spiral zone plate," JETP Lett., **76**, 486 – 489 (2002)

[115] I.V. Basistiy, V.V. Slyusar, M.S. Soskin, M.V. Vasnetsov and A.Ya. Bekshaev, "Manifestation of the rotational Doppler effect by use of an off-axis optical vortex beam," Opt. Lett., **28**, 1185 – 1187 (2003)

[116] M.V. Vasnetsov, J.P. Torres, D.V. Petrov and Lluis Torner, "Observation of the orbital angular momentum spectrum of a light beam," Opt. Lett., **28**, 2285 – 2287 (2003)

[117] C.N. Alexeyev, A.N. Alexeyev and M.A. Yavorsky, "Optical vortices in rotating weakly guiding ideal optical fibers," J. Opt. A: Pure Appl. Opt., **6**, 762 – 768 (2004)

[118] C.N. Alexeyev, A.N. Alexeyev and M.A. Yavorsky, "Effect of one-axis anisotropy on the propagation of optical vortices in rotating optical fibers," J. Opt. A: Pure Appl. Opt., **7**, 63 – 72 (2005)

[119] T.A. Fadeyeva, A.N. Alexeyev, C.N. Alexeyev, "Rotational Doppler effect in weakly guiding optical fibres,' Proc. SPIE **6254**, 625401 (2006)

[120] A.N. Alexeyev, C.N. Alexeyev, T.A. Fadeyeva and A.V. Volyar, "Analysis of singularity properties of the radiation field in low-mode optical fibers," Ukr. J. Phys., **7**, 11 – 17 (2006)

[121] W. L. Wolfe, "*Nondispersive prisms*," in Handbook of Optics, 2nd ed., M. Bass, E. W. Van Stryland, D. R. Williams, and W. L. Wolfe, eds. (McGraw-Hill, New York, 1995), pp. 4.1–4.29.

[122] D. L. Sullivan, "Alignment of rotational prisms," Appl. Opt. **11**, 2028–2032 (1972).

[123] I. Moreno, G. Paez, and M. Strojnik, “Dove prism with increased throughput for implementation in a rotational shearing interferometer,” Appl. Opt. **42**, 4514–4521 (2003).

[124] M.S. Scholl and G. Paez, “Simulated interferometric patterns generated by a nearby star-planet system and detected by a rotational shearing interferometer,” J. Opt. Soc. Am. A **16**, 2019–2024 (1999).

[125] H. Fujii and Y. Ohtsuka, “Rotational filtering for randomly oriented pattern recognition,” Opt. Commun. **36**, 255–257 (1981)

[126] C. Perez-Lopez, F.M. Santoyo, G. Pedrini, S. Schedin, and H.J. Tiziani, “Pulsed digital holographic interferometry for dynamic measurement of rotating objects with an optical derotator,” Appl. Opt. **40**, 5106–5110 (2001)

[127] P.Z. Takacs, E.L. Church, C.J. Bresloff, and L. Assoufid, “Improvements in the accuracy and the repeatability of long trace profiler measurements,” Appl. Opt. **38**, 5468–5479 (1999).

[128] A.V. Smith and M.S. Bowers, “Image-rotating cavity designs for improved beam quality in nanosecond optical parametric oscillators,” J. Opt. Soc. Am. B **18**, 706–713 (2001).

[129] D.J. Armstrong and A.V. Smith, “Demonstration of improved beam quality in an image-rotating optical parametric oscillator,” Opt. Lett. **27**, 40–42 (2002).

[130] N. Gonz´alez, G.M. Terriza, and J.P. Torres, “How a dove prism transforms the orbital angular momentum of a light beam,” Opt. Exp, **14**, 9093-9102 (2006)

[131] J. Leach, M.J. Padgett, S.M. Barnett, S. Franke-Arnold, and J. Courtial, "Measuring the Orbital Angular Momentum of a Single Photon," Phys. Rev. Lett. **88**, 257901 (2002).

[132] R. Zambrini and S.M. Barnett, "Quasi-Intrinsic Angular Momentum and the Measurement of Its Spectrum," Phys. Rev. Lett. **96**, 113901 (2006).

[133] M.J. Padgett and J.P. Lesso, " Dove prisms and polarized light," Journal of Modern Optics, **46**, 175-179 (1999)

[134] I. Moreno, G. Paez and M. Strojnik, "Polarization transformation properties of Dove prisms," Opt.Commun, **220**, 257-268 (2002).

[135] I. Moreno, "Jones matrix for image rotation prisms" Appl. Opt, **43**, 3373-3381 (2004)

[136] Y. Roichman, B. Sun, Y. Roichman, J. Amato-Grill, and D.G. Grier, **"**Optical forces arising from phase gradients," PRL. **100**, 013602-4 (2008)

[137] D.B. Ruffner and D.G. Grier, **"**Optical forces and torques in nonuniform beams of light," PRL. **108**, 173602-4 (2012)

[138] E. Hasman, A. Niv, G. Biener and V. Kleiner, "Vectorial vortices obtained with quantized Pancharatnam-Berry phase optical element," Proc. of SPIE. 6131, 613107-8 (2006)

[139] L. Marrucci, E. Karimi, S. Slussarenko, B. Piccirillo, E.Santamato, E. Nagali, and F. Sciarrino, "Spin-to-orbital conversion of the angular momentum of light and its classical and quantum applications," J. Opt. **13**, 064001 (2011).

[140] F. Cardano, E. Karimi, S. Slussarenko, L. Marrucci, C. de Lisio, and E. Santamato, 'Polarization pattern of vector vortex beams generated by q-plates with different topological charges," Appl. Opt. **51**, C1-C6 (2012)

[141] M. Beresna, M. Gecevicius, and P.G. Kazansky, “Polarization sensitive elements fabricated by femtosecond laser nanostructuring of glass,” Opt. Exp. **1**, 783-795 (2011)

[142] E.J. Galvez, S. Khadka, W.H. Schubert, and S. Nomoto, “Poincare-beam patterns produced by nonseparable superpositions of Laguerre–Gauss and polarization modes of light,” Appl. Opt. **51**, 2925-2934 (2012)

[143] Z. Zhou, Q. Tan, and G. Jin, “Theoretical and experimental studies on tightly focused vector vortex beams,” Appl. Opt, **50**, G80-G85 (2011)

[144] K. Kitamura, K. Sakai, N. Takayama, M. Nishimoto, and S. Noda, “Focusing properties of vector vortex beams emitted by photonic-crystal lasers,” Opt. Lett, **37**, 2421-2423 (2012)